DEVELOPMENT AND EVALUATION OF MULTIFERROIC NANOPARTICLE-BASED DRUG DELIVERY SYSTEM

Dissertation

Gençay SEVİM

Eskişehir 2023

DEVELOPMENT AND EVALUATION OF MULTIFERROIC NANOPARTICLE-BASED DRUG DELIVERY SYSTEM

Gençay SEVİM

Dissertation
Department of Advanced Technologies
Programme in Nanotechnology
Supervisor: Assoc. Prof. Dr. Gülay BÜYÜKKÖROĞLU

Eskişehir
Eskişehir Technical University
Institute of Graduate Programs
January 2023

This thesis has been supported by the project 2002S008 of Anadolu University, which is approved by the SRP Committee.

FINAL APPROVAL FOR THESIS

This thesis titled DEVELOPMENT AND EVALUATION OF MULTIFERROIC NANOPARTICLE-BASED DRUG DELIVERY SYSTEM has been prepared and submitted by Gençay SEVİM in partial fulfillment of the requirements in "Eskişehir Technical University Directive on Graduate Education and Examination" for the Degree of PhD in Advanced Technologies Department has been examined and approved on 17/01/2023.

Committee Members		**Title, Name and Surname**	**Signature**
Member	:	Prof. Dr. Servet TURAN	
Member	:	Prof. Dr. Rana ARSLAN	
Member	:	Assoc. Prof. Dr. Behiye ŞENEL	
Member	:	Prof. Dr. Murat CANPOLAT	
Member	:	Prof. Dr. Semir ÖZDEMİR	

Prof. Dr. Murat TANIŞLI
Director of the Institute of Graduate Programs

17/01/2023

SUPERVISOR APPROVAL

PhD student Gençay SEVİM, whom I supervise, has completed this thesis titled DEVELOPMENT AND EVALUATION OF MULTIFERROIC NANOPARTICLE-BASED DRUG DELIVERY SYSTEM. According to my inspections, the work is scientifically and ethically appropriate for the student to the thesis defense exam.

Supervisor

Assoc. Prof. Dr. Gülay BÜYÜKKÖROĞLU

ABSTRACT

DEVELOPMENT AND EVALUATION OF MULTIFERROIC NANOPARTICLE-BASED DRUG DELIVERY SYSTEM

Gençay SEVİM

Department of Advanced Technologies
Programme in Nanotechnology
Eskişehir Technical University, Institute of Graduate Programs, January 2023
Supervisor: Assoc. Prof. Dr. Gülay BÜYÜKKÖROĞLU

Due to the deficiencies and side effects of the methods commonly used in cancer treatment, there is a need for targeted drug delivery systems that actively target the cancerous region. In active targeting, multiferroic materials that several groups have been working on in recent years are promising. Magneto-electric nanoparticles (MENs), one of the multiferroic materials, are structures that can both be targetable and perform nano-electroporation due to their multiferroic properties.

This thesis aims to develop a drug delivery system that can target metastatic bone cancer. As the targeting part, magneto-electric $CoFe_2O_4$-$BaTiO_3$ biphasic nanostructures were synthesized. These nanostructures are coated with MEIS1 protein inhibitor-loaded solid lipids that bind to MEIS protein and suppress tumoral activity in cancer cells. Physicochemical characterizations of the prepared systems were carried out, and their effects on different cancer cells that could metastasize to the bone were evaluated in vitro. In addition, a theoretical data pool of MENs was created using MATLAB.

Keywords: Multiferroics, Magnetoelectric effect, Active targeting, MEIS protein inhibitor, Metastatic cancer.

ÖZET

MULTİFERROİK ÖZELLİKLİ NANOPARÇACIK TABANLI İLAÇ TAŞIYICI SİSTEMİN GELİŞTİRİLMESİ VE DEĞERLENDİRİLMESİ

Gençay SEVİM

İleri Teknolojiler Anabilim Dalı
Nanoteknoloji Bilim Dalı
Eskişehir Teknik Üniversitesi, Lisansüstü Eğitim Enstitüsü, Ocak 2023
Danışman: Doç. Dr. Gülay BÜYÜKKÖROĞLU

Kanser tedavisinde yaygın olarak kullanılan yöntemlerin eksiklikleri ve yan etkileri sebebiyle, kanserli bölgeye aktif olarak hedeflendirilmiş ilaç taşıyıcı sistemlere ihtiyaç duyulmaktadır. Aktif hedeflemede son yıllarda üzerinde sayılı grubun çalıştığı multiferroik malzemeler gelecek vaat etmektedir. Multiferroik malzemelerden biri olan manyeto-elektrik nanoparçacıklar (MEN), sahip oldukları ferroik özellikler nedeniyle hem hedefe yönlendirilme hem de nanoelektroporasyon etki gösterme özelliğine sahip yapılardır.

Bu tez çalışmasında, metastatik kemik kanserine hedeflendirilebilecek bir ilaç taşıyıcı sistemin geliştirilmesi amaçlanmıştır. Hedefleme parçası olarak manyeto-elektrik özellikli $CoFe_2O_4$-$BaTiO_3$ çift fazlı nanoyapılar sentezlenmiştir. Bu nanoyapılar MEIS proteinine bağlanarak kanser hücrelerinde tümöral aktiviteyi baskılayan MEIS1 protein inhibitörü yüklenmiş katı lipitlerle kaplanmıştır. Hazırlanan sistemlerin fizikokimyasal karakterizasyonu gerçekleştirilmiş ve kemiğe metastaz yapabilen farklı kanser hücreleri üzerindeki etkinliği in vitro olarak değerlendirilmiştir. Ayrıca MATLAB kullanılarak MEN'lerin teorik bir veri havuzu oluşturulmuştur.

Anahtar Sözcükler: Multiferroikler, Manyetoelektrik etki, Aktif hedefleme, MEIS protein inhibitörü, Metastatik kanser.

ACKNOWLEDGEMENTS

The academic career journey is always a challenging way to the life of an academician. However, the impact of the teachers in the face of obstacles on this path is enormous. Like every academician, there have been many obstacles and difficulties in my academic life. But the teachers I will mention about have made these obstacles and difficulties bearable and surmountable for me.

Firstly, to my fiancée, Betül ORUÇ, for having a significant role in my starting this doctoral program and supporting me not only throughout my doctoral education but always, and helping me get through this process easier when I lost my self-confidence,

To my dear teacher, Assoc. Dr. Gülay BÜYÜKKÖROĞLU, for always opening my horizons with her innovative vision in every sense from the moment I met her, always supporting me and being more than just an academic advisor for me,

To my dear teacher, Assoc. Dr. Behiye SENEL, for answering my questions tirelessly with his naive and polite approach, and guiding me with her ideas not only in the laboratory but also in my personal life,

To my dear teacher, Prof. Dr. Servet TURAN, for never sparing his support since I started my Ph.D., never getting tired of me disturbing him to get his valuable ideas, and setting an example for me as an academic,

To my dear teacher, Prof. Dr. Murat CANPOLAT, for helping me develop not only academically but in every sense with his high-quality counseling in my graduate education, and making me feel at every opportunity that I was not alone in this journey,

To my dear teacher, Prof. Dr. Semir ÖZDEMİR, for always setting an example for me both with his ideas and his attitude toward students from the first moment I met him in my biophysics education, and for having a heart-to-heart talkable with me about my problems,

To my dear teacher, Prof. Dr. Rana ARSLAN, for contributing to both the development of my thesis project and my development with her ideas during my doctoral thesis process, and for supporting me at every opportunity with his polite and friendly attitude,

To my dear teacher, Prof. Dr. Uğur SERİNCAN, for patiently answering my questions during my doctoral education and helping me get through my adaptation process quickly with his sincere behavior,

To my dear teacher, Prof. Dr. Nihan KOSKU PERKGÖZ, for making me love Nanotechnology during my doctoral education, opening my horizons on this subject, and always setting an example for me as an educator with her kind and naive behavior,

To my dear teachers, Prof. Dr. Nazmi YARAŞ and Prof. Dr. Narin DERİN, for enabling me to develop in Biophysics in my graduate education,

To my dear teachers, Prof. Dr. Hülya SİVAS and Prof. Dr. Ayşe Tansu KOPARAL, for allowing me to attend their courses as a guest participant even though I could not formally take the courses in the areas I wanted to improve in my doctoral education,

To my esteemed teachers in the Department of Pharmaceutical Technology, Prof. Dr. Müzeyyen DEMİREL, Prof. Dr. Ebru BAŞARAN, Assoc. Dr. Evrim YENİLMEZ, Assoc. Dr. Ahmet Alper ÖZTÜRK, Assoc. Dr. Mustafa Sinan KAYNAK, Assist. Prof. Dr. Gülsel YURTDAŞ KIRIMLIOĞLU and Assist. Prof. Dr. Murat Sami BERKMAN, for making me feel like not a stranger by accepting me among them and for sharing their opinions with me on many issues,

To my dear teacher, Assoc. Dr. Fatih KOCABAŞ, for providing the MEIS protein inhibitor to be used in my doctoral thesis project,

To my dear teacher, Prof. Dr. Fatih DEMİRCİ, for letting me use his lab for my Ph.D. thesis project,

To all the academic and administrative staff of ESTU Graduate Education Institute, always keeping me informed about academic problems during my Ph.D.,

To my dear friends, Assist. Prof. Dr. Member Tanju MERCAN, Lec. Dr. Yiğit Ali ÜNCÜ, Assoc. Dr. Hasan ÖZDOĞAN, Assist. Prof. Dr. Murat Cenk ÇELEN, Cihan ATAK, Dr. Murat BÜYÜKAKSU, İbrahim AKDİLEK, Dr. Orhan ŞİŞMAN, Yusuf KASAP, Tolga ŞİMŞEK, Assist. Prof. Dr. Enis HİDİŞOĞLU, Serkan TARHAN, Onur KAYNARCALI, Sezer ÖZALTIN, Gizem DEĞER, Res. Assist. Sinan ÖZER, Res. Assist. Kadir AYKAÇ, Lect. Berna KAVAL, Pharm. İrem NAMLI, Dr. Damla KIRCI, Assist. Prof. Dr. Güven AKÇAY, Assist. Prof. Dr. Uğur DALAMAN, Kadri GÜLEÇ, Res. Assist. Ceyda KÖROĞLU, Gökhan KADIOĞLU, Nur KADIOĞLU and İsmail SAMSA, for always supporting me in all matters and for always trying to help me on this challenging path, and also Umut Ece KESKİN and Ercan KESKİN, for not withholding their crucial support at the most critical moment of my life,

To my dear father Tuncay SEVİM, my dear mother Figen SEVİM, my dear mother-in-law Özden ÖÇ, my dear brother Ahmet SEVİM and his wife Cansu SEVİM, and my dear cousin Olcay GÜNAY, for having always stood by me and for supporting me in every decision I made, and my niece Nisan Mila SEVİM, for making us happy and adding color to our lives with her birth.

To my dear teachers, Prof. Dr. Servet TURAN, Prof. Dr. Ender SUVACI, and Prof. Dr. Müfide BANAR, for having made me eligible to receive Council of Higher Education 100/2000 Ph.D. scholarship support with their positive opinions, and to CoHE, for providing this scholarship support enabling me to continue my doctoral education,

To Akdeniz University, Eskişehir Technical University, and Anadolu University for the opportunities and social connections they provided me, and, to Middle East Technical University, for always enabling me to move forward with its quality education and its motto of lifelong learning,

Finally, to my dear teacher, Prof. Dr. Feridun AY, who has a share in this thesis and all my future academic studies and achievements, for supporting me at the breaking point in my life and convincing me not to quit my Ph.D., for making me feel lucky to have crossed paths with him,

THANK YOU WITH ALL MY HEART.

Gençay SEVİM

17/01/2023

STATEMENT OF COMPLIANCE WITH ETHICAL PRINCIPLES AND RULES

I hereby truthfully declare that this thesis is an original work prepared by me; that I have behaved in accordance with the scientific ethical principles and rules throughout the stages of preparation, data collection, analysis and presentation of my work; that I have cited the sources of all the data and information that could be obtained within the scope of this study, and included these sources in the references section; and that this study has been scanned for plagiarism with "scientific plagiarism detection program" used by Eskişehir Technical University, and that "it does not have any plagiarism" whatsoever. I also declare that, if a case contrary to my declaration is detected in my work at any time, I hereby express my consent to all the ethical and legal consequences that are involved.

Gençay SEVİM

CONTENTS

PAGE

HEADER PAGE ..... **I**
FINAL APPROVAL FOR THESIS ..... **II**
SUPERVISOR APPROVAL ..... **III**
ABSTRACT ..... **IV**
ÖZET ..... **V**
ACKNOWLEDGEMENTS ..... **VI**
STATEMENT OF COMPLIANCE WITH ETHICAL PRINCIPLES AND RULES ..... **IX**
CONTENTS ..... **X**
LIST OF TABLES ..... **XIII**
LIST OF FIGURES ..... **XIV**
LIST OF IMAGES ..... **XV**
GLOSSARY OF SYMBOLS AND ABBREVIATIONS ..... **XVI**
1. INTRODUCTION **1**
2. SOURCE INFORMATION **4**
2.1. Cancer **4**
2.1.1. Cancer etiology **5**
2.1.2. Cancer epidemiology **6**
2.1.3. Bone cancer **8**
2.1.3.1. Primary bone cancer **8**
2.1.3.2. Secondary bone cancer **9**
2.2. Bone Anatomy **12**
2.3. Current Cancer Treatment Methods **14**
2.3.1. Surgical intervention **14**
2.3.2. Radiotheraphy **15**
2.3.3. Chemotheraphy **15**
2.4. Targeted Drug Delivery Systems **16**
2.4.1. Their historical background **16**
2.4.2. Their structure **17**
2.4.2.1. Carrier and protective part **17**

2.4.2.2. Targeting part 19
Passive targeting 19
Active targeting 20
2.5. Multiferroics 24
2.5.1. Magneto-electric effect 26
2.5.2. Targeted drug delivery mechanism with magneto-electric effect 28
2.6. MEIS and Associated Factors in Tumorogenesis 30
2.6.1. MEIS and cancer 31
3. MATERIAL AND METHOD 33
3.1. Utilized Units 33
3.2. Utilized Materials 33
3.3. Utilized Devices and Equipment 34
3.4. Synthesis of Magneto-Electric Nanoparticles 35
3.5. Preparation of Solid Lipid Coated MN and MEN Formulation 36
3.5.1. Preparation of solid lipid nanoparticles 36
3.5.2. Preparation of solid lipid nanoparticles containing MEIS1 protein inhibitor 37
3.5.3. Coating of MNs and MENs with a lipid layer 37
3.5.4. Coating of MNs and MENs with a lipid layer containing MEIS1 protein inhibitor 38
3.6. Analytical Method Development and Validation 39
3.6.1. Validation study 39
3.6.1.1. Linearity 39
3.6.1.2. Accuracy 39
3.6.1.3. Precision 40
3.6.1.4. Sensitivity 40
3.6.2. Determining the amount of MEIS conjugated to MNs and MENs 41
3.7. Determination of the Effects of Prepared Drug Systems on Cells 41
3.7.1. Cell culture studies 41
3.7.2. MTT test 42
3.8. Characterization of Nanostructures 42
3.8.1. Analysis of particle sizes and charges of nanostructures 43
3.8.2. Morphological analysis of nanostructures 43

3.8.3. Analysis of magnetic properties of nanostructures 43
3.8.4. Chemical Analysis of Nanostructures..... 44
3.8.5. Analysis of Crystal Structures of Nanostructures..... 44
4. FINDINGS AND DISCUSSION..... 46
4.1. Standardization of MN Synthesis 47
4.1.1. Magnetization test 48
4.1.2. Particle size, polydispersity index and zeta potential..... 48
4.2. Synthesis of MENs..... 50
4.3. Characterization of MENs and MNs..... 52
4.3.1. Magnetic characterization 52
4.3.2. Morphological characterization..... 55
4.3.3. Chemical characterization..... 59
4.3.4. Crystal structure characterization..... 63
4.4. Characterizations of Lipid-Coated Formulations..... 67
4.5. Analytical Method Development and Validation Study 69
4.5.1. Linearity 69
4.5.2. Precision 70
4.5.3. Accuracy..... 71
4.5.4. Sensitivity 72
4.5.5. Determining Loading Activity..... 72
4.6. Cell Culture Studies 73
4.7. The Data Pool Created to Determine the Limitations of MENs..... 84
5. CONCLUSION 88
REFERENCES..... 89
APPENDIX
CURRICULUM VITAE

LIST OF TABLES

Page

Table 2.1. Leading cancer types worldwide in 2020 in terms of new cases (incidence) and deaths (mortality) by sex (Ferlay et al., 2021). 7
Table 3.1. A list of utilized materials in the study. 33
Table 3.2. A list of utilized devices and equipment in the study. 34
Table 3.3. The codes given to the prepared formulations and their contents. 38
Table 3.4. UPLC analysis conditions 39
Table 4.1. Magnetizations of MNs synthesized at each pH. 48
Table 4.2. Particle sizes, PDI and Zeta potentials of MNs synthesized at different pHs. 50
Table 4.3. Particle size, PDI, and zeta potential measurements of formulations prepared within the scope of lipid coating studies. 68
Table 4.4. Results of Precision Study 70
Table 4.5. Results of Accuracy Study 71
Table 4.6. Results of Sensitivity Study 72

LIST OF FIGURES

Page

Figure 2.1. Molecular development of sporadic and hereditary cancers 5

Figure 2.2. Brief illustration of the steps of cancer metastasis 10

Figure 2.3. (A) It is a rough representation of paravertebral connections such as vessels, nerves that may form connections with other organs. (B) A rough representation of the Axial Skeleton. (C) A rough representation of the paravertebral space..... 11

Figure 2.4. Representation of the basic parts of bone structure..... 14

Figure 4.1. Linearity Graph of MEIS (n=6)..... 70

Figure 4.2. Chromatograms of MEIS inhibitor, MS50, MS50MN, and MS50MEN formulations 73

Figure 4.3. Viability test results of MNs on HUVEC cell line 74

Figure 4.4. Viability test results of MENs on HUVEC cell line..... 75

Figure 4.5. Viability test results of MENs on PANC-1 cell line 75

Figure 4.6. Chemical formula of paracetamol 76

Figure 4.7. 24- and 48-hour MTT test results of formulations prepared with Gelucire44/14 on MCF-10A cells..... 78

Figure 4.8. 24- and 48-hour MTT test results of formulations prepared with Gelucire44/14 on MCF-7 cells..... 79

Figure 4.9. 24- and 48-hour MTT test results of formulations prepared with Gelucire44/14 on MDA-MB-231 cells 80

Figure 4.10. 24- and 48-hour MTT test results of formulations prepared with Gelucire50/13 on MCF-10A cells..... 81

Figure 4.11. 24- and 48-hour MTT test results of formulations prepared with Gelucire50/13 on MCF-7 cells..... 83

Figure 4.12. 24- and 48-hour MTT test results of formulations prepared with Gelucire50/13 on MDA-MB-231 cells 84

LIST OF IMAGES

Page

Image 4.1. Magnetic nanoparticles synthesized at different pHs 47

Image 4.2. Synthesis of MNs by hydrothermal method 51

Image 4.3. Synthesis of MENs by hydrothermal method 52

Image 4.4. Hysteresis plot of MNs obtained with VSM 53

Image 4.5. Hysteresis plot of MENs obtained with VSM 53

Image 4.6. TEM image of MNs (200000x) 57

Image 4.7. TEM image of MENs (10000x) 58

Image 4.8. TEM image of a MEN structure (100000x) 58

Image 4.9. TEM image of aggregated MENs (400000x) 59

Image 4.10. XPS analysis of element iron in MNs 60

Image 4.11. XPS analysis of element cobalt in MNs 60

Image 4.12. XPS analysis of element cobalt in MENs 61

Image 4.13. XPS analysis of element iron in MENs 62

Image 4.14. XPS analysis of element barium in MENs 62

Image 4.15. XPS analysis of element titanium in MENs 63

Image 4.16. XRD analysis of MNs 65

Image 4.17. XRD analysis of MENs 66

Image 4.18. The pool containing all the electrical fields that can be produced according to each parameter within the determined limits 86

Image 4.19. Pool of electrical fields in the theoretical window from which nanoparticles producing electrical fields high enough to interact with healthy cells and low enough not to interact with cancer cells are extracted. 87

Image 4.20. Graph showing the zeta potentials, particle radii and critical distance of nanoparticles that can generate the appropriate electric field. 87

GLOSSARY OF SYMBOLS AND ABBREVIATIONS

EPR	:	Enhanced Permeability and Retention
MEIS1	:	Myeloid Ecotropic Viral Insertion Site 1
ME	:	Magneto-electric
MEN	:	Magneto-electric Nanoparticle
MN	:	Magnetic Nanoparticle
P	:	Electrical Polarization
M	:	Magnetization
α	:	ME coefficient
δ_{ij}	:	Kronecker symbol
ε_{ijk}	:	Levi-Civita Symbol
J	:	Spatial Inversion
T	:	Temporal Reversal
k	:	Coulomb constant
p	:	Dipole Moment
Q	:	Electrical Charge
r	:	Cut-off Distance
DMEM	:	Dulbecco's Modified Eagle Medium
DMSO	:	Dimethylsulfoxide
UPW	:	Ultra-Pure Water
HUVEC	:	Human Umbilical Vein Endothelial Cell
A549	:	Adenocarcinomic Human Alveolar Basal Epithelial Cell
PANC-1	:	Human Pancreas Ductal Adenocarcinoma Cell
VSM	:	Vibrating Sample Magnetometer
TEM	:	Transmission Electron Microscopy

PDI	:	Polydispersity Index
XPS	:	X-Ray Photoelectron Spectroscopy
XRD	:	X-Ray Diffractometer
MCF-7	:	Human Breast Cancer Cell Line
MCF-10A	:	Non-Malignant Breast Cell Line
MDA-MB-231	:	Poorly Differentiated Triple-Negative Breast Cancer Cell Line
UPLC	:	Ultra-Performance Liquid Chromatography

1. INTRODUCTION

The skeletal system, which is responsible for many vital mechanisms of the body, consists of bones. Bones have different anatomical structures from other organs of the body. A pathogenic condition in bones can affect the whole body due to both this different structure of bones and the relationship of the skeletal system with other organs and systems in the body (Florencio-Silva et al., 2015). Metastatic bone cancers, also known as secondary bone cancer, are one of the best examples of this. Cancers in organs such as the prostate and breast closely related to the axial skeleton system can easily metastasize to the bones (Mundy, 2002). For this reason, it is essential to know the primary cancer types they originate from to make appropriate interventions during the treatment phase. In this context, different treatment methods can be used to treat metastatic bone cancer using international guidelines. However, current treatment methods have some shortcomings and disadvantages. Many studies on targeted drug delivery systems have been done and are still being done to prevent these (Bañobre-López et al., 2013; Barenholz, 2012; Beik et al., 2016; Cravo & Mrsny, 2013; Guduru et al., 2013; Iyer et al., 2006; Jurgons et al., 2006; Khan et al., 2015; Rajabi et al., 2016; Rodzinski et al., 2016).

Targeted drug delivery systems basically consist of two main parts as carrier/protective part and therapeutic agent. However, the targeting part is also included among these main parts according to the targeting mechanism (Pattni & Torchilin, 2015).

The carrier/protective part is responsible for protecting the system until it reaches the target tissue. For this, one selects parts specific to the region or tissue to be targeted. These parts may have different sensitivities such as heat, pH, etc (de Smet et al., 2010, 2013; Du et al., 2011; Torchilin, 2006; Ward & Georgiou, 2011; Yatvin et al., 1978).

After determining the carrier/protective part, the same principle applies to determining the targeting mechanism. There are different targeting mechanisms; passive, active, or both (Khan et al., 2015). In the passive targeting mechanism, targeting is carried out by utilizing natural biological changes called the enhanced permeability and retention effect (EPR) without the targeting part (Iyer et al., 2006; Pattni & Torchilin, 2015). In other words, tissue-specific targeting is done with specific targeting parts in active targeting mechanisms (Pattni & Torchilin, 2015). For this, active targeting parts such as ligand-based, chemical, physical, etc. are preferred.

However, each targeting mechanism has certain limitations (Bañobre-López et al., 2013; Chen et al., 2016).

Magnetic nanoparticles (MNs), one of the targeting parts used in physical targeting mechanisms, are promising in many ways. They have the potential to be used in many areas, as they can carry drug systems to the target region or tissue in external magnetic field exposure, as well as allow local hyperthermia application in oscillating magnetic field exposure (Bañobre-López et al., 2013; Beik et al., 2016; Jurgons et al., 2006). Recent studies have furthered these potentials of MN and suggested the use of magneto-electric nanoparticles (MENs). Nanoparticles with magneto-electric properties, on which few research teams have been working, have been tried to use as targeting parts. These nanoparticles are magnetized under magnetic field exposure, but they also become electrically polarized (Guduru et al., 2013; Rodzinski et al., 2016; Stewart et al., 2018; Stimphil et al., 2017; Yue et al., 2012). These nanoparticles are also one of the multiferroic structures. Multiferroic structures simultaneously have two or more ferroelectric, ferroelastic, and ferromagnetic properties. This special physical state has opened a new door for targeting mechanisms. Under a magnetic field, MENs can be targeted by being magnetized and enable cellular nano-electroporation by being electrically polarized (Guduru et al., 2013; Rodzinski et al., 2016).

In this study, both MNs and MENs were selected as targeting parts that would enable the transport of MEIS1-protein inhibitor, a chemotherapeutic agent, to the target site by magnetic field exposure. The bone, which we think can be applied more easily locally, was chosen as the target region.

One uses legally approved agents for each cancer type as a chemotherapeutic agent. These agents may also differ according to the type of cancer. The mechanism of action of each agent is different. For example, taxane-class chemotherapeutics prevent cancer cell growth and proliferation by binding to microtubulins. This situation plays an essential role in cell division (Ojima et al., 2016). In contrast, anthracyclines inhibit proliferation by interventing DNA or RNA synthesis (Henriksen, 2018). There are many chemotherapeutics having different mechanisms of action. One of them is a MEIS1-protein inhibitor developed by Fatih KOCABAŞ and his team (Aksoz et al., 2018; Turan et al., 2020; Turgutalp et al., 2021).

Myeloid ecotropic viral insertion site 1 (MEIS1) was first identified as a viral integration site in mouse myeloid leukemia cells in the mid-1990s (Moskow et al.,

1995). It promotes tumorigenesis by being highly expressed in many tumor cells and causes tumor cells to develop resistance to drug therapy by forming a complex with cell DNA (Aksoz et al., 2018; Geerts et al., 2005; Moskow et al., 1995; Tomoeda et al., 2011; Turan et al., 2020). Also, it is known that they are associated with many types of cancer (Aksoz et al., 2018; Crist et al., 2011; Geerts et al., 2005; Svingen & Tonissen, 2003; Tomoeda et al., 2011). Therefore, a MEIS1-protein inhibitor inhibiting these cancer-associated MEIS proteins has been developed. It has been shown that this inhibitor can inhibit over 95% MEIS-luciferase activity and downregulate MEIS target gene expression at one μM dose. In addition, one determined that the MEIS1 inhibitor is effective in preventing drug resistance and reducing the rate of metastasis (Aksoz et al., 2018; Turan et al., 2020).

In this doctoral thesis, the aim was to develop a carrier system having magnetically targetable MNs and MENs coated with a lipid layer containing MEIS1 protein inhibitor for the treatment of metastatic bone cancer and to evaluate its efficacy in MDA-MB-231 and MCF-7 breast cancer cells metastasizing bone.

2. SOURCE INFORMATION

2.1. Cancer

Cancer, formed by the uncontrolled proliferation of cells, is a disease of critical importance worldwide. Early diagnosis and treatment affect the course of the disease vitally (Wardle et al., 2015).

When mentioning cancer, benign and malignant structures usually come to mind. However, some changes occur at the cellular level before carcinogenesis takes place. These include many cellular changes, such as defects in apoptosis mechanisms of cells, disturbances in growth and proliferation mechanisms, terminal differentiation, and changes in intercellular bonds (Hassanpour & Dehghani, 2017). It is known that these changes occur due to a series of genetic mutations occurring at the molecular level.

Cancer types resulting from genetic mutations are based on two different genetic mutations. One of them is the germline mutation that occurs in germ cells. Individuals having this mutation can transfer the mutation to their children. In this way, hereditary cancer types are transmitted from generation to generation through genes (Loveday et al., 2011; Mehenni et al., 2006). Another genetic mutation is somatic mutation. Somatic mutation is a type of mutation that occurs in cells other than germ cells and is not inherited. It plays a role in the occurrence of non-hereditary cancers (Martincorena & Campbell, 2015). However, Alfred Knudson put forward the two-hit hypothesis for both hereditary and sporadic types of cancer in which both mutations occur (Knudson, 1971). He worked on retinoblastoma and suggested that both mutations must be present for retinoblastoma to happen according to this hypothesis (Knudson, 1971).

Each gene has two alleles in humans: one paternal and one maternal. In retinoblastoma, both alleles must be mutated. Considering that a parent with a germline mutation transfers one of these alleles, the other must be somatically mutated for an individual to develop retinoblastoma (Knudson, 1971). In this context, it was observed that normally heterozygous individuals experience loss of heterozygosity in retinoblastoma (Stenfelt et al., 2017). One of the main reasons is interstitial deletion, one of the somatic mutations. With interstitial deletion, the normal allele is also mutated. Therefore, heterozygosity is lost, and cancer development occurs (Mitter et al., 2011). This situation is shown in summary form in Figure 2.1.

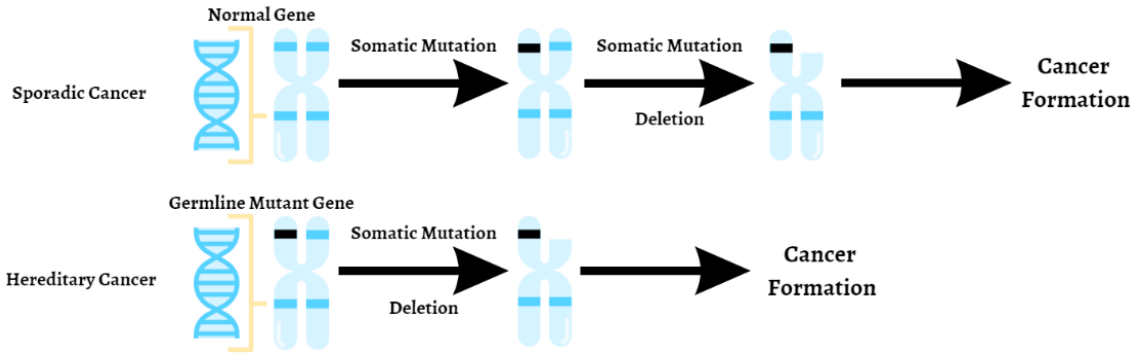

Figure 2.1. *Molecular development of sporadic and hereditary cancers*

In this way, many mutation-based cellular and molecular changes lead to the formation of cancer cells. Even after cancer cells are formed, changes continue to occur in some cellular and biological mechanisms. Especially modifications such as activation of proto-oncogenes, inactivation of tumor-suppressor genes, and inactivation of genomic-stagnation genes begin to form preneoplastic lesions. Afterward, as the cancerous lesions continue to multiply, tumor formation begins (Hassanpour & Dehghani, 2017).

2.1.1. Cancer etiology

Although the exact reason of cancer is unknown, certain risk factors exist to define its etiology. These risk factors are basically grouped into two groups: modifiable factors and non-modifiable factors. Uncontrollable demographic characteristics specific to patients, such as age, gender, genetic inheritance, etc. are considered as cancer factors that cannot be changed. On the other hand, many controllable environmental factors include diet, smoking habits, alcohol habits, radiation exposure, solar exposure, and stress. (Arem & Loftfield, 2018; Bandi et al., 2021; Stein & Colditz, 2004).

These risk factors may not always cause cancer formation. However, they can increase the probability of developing cancer by triggering the cancer formation mechanism at the molecular level. Therefore, it is crucial to know the risk factors for cancer development. For example, when some people will be diagnosed with cancer, their family history of cancer is tried to be analyzed. Because people with a family history of cancer may be more likely to develop cancer. This condition is also called genetic predisposition (Frank, 2004).

Some risk factors can affect different types of cancer in different ways. For example, considering risk factors such as age and gender cervical cancer occurs only in

women, while prostate cancer occurs only in men. The risk of gender-based cancer varies because the cervix is a physiological structure that exists only in women, and the prostate gland is a physiological structure that only exists in men. With such examples, one can easily see that cancer types differ according to "gender risk factor" due to gender-based physiological characteristics (Greenlee et al., 2000; H. I. Kim et al., 2018).

In addition, cancer types can be seen in both sexes but can be specialized according to a gender. One of the best examples is breast cancer, usually seen in women. Lobular cancer, one of the common types of breast cancer, originates from the mammary glands, while ductal cancer, another common type of breast cancer, originates from the milk ducts. Men have different breast anatomy than women. They do not have breast lobes and developed milk ducts. Since they do not have this breast anatomy, the incidence of breast cancer in men is relatively low. However, in the case of breast cancer in men, it is more likely that cancer can metastasize to the lymph nodes. In this way, one can see a differentiation between different sexes in the same cancer types (Greenlee et al., 2000).

In addition to the gender risk factor, the age risk factor can have a similar effect. Some types of cancer are more common in people over 50, while some types of cancer occur at a very young age. For example, Ewing Sarcoma, a rare type of primary bone cancer, is usually seen at young ages, especially in adolescents (Grünewald et al., 2018). In contrast, prostate cancer is more common in men aged 50-70. Also, the probability of developing this cancer also increases exponentially after 50 (Pienta & Esper, 1993).

In brief, modifiable risk factors and non-modifiable risk factors trigger many types of cancer and affect the probability of cancer development (White et al., 2014).

2.1.2. Cancer epidemiology

According to the current data from the World Health Organization, cancer is one of the diseases with the highest mortality, causing the death of approximately 10 million people worldwide in 2020 (Ferlay et al., 2021). Its incidence and prevalence worldwide are also increasing day by day. Among the new cases in 2020, breast cancer led to 2.26 million new cancer cases, followed by lung cancer with 2.21 million new cases. These are followed by 1.93 million new colon and rectal cancer cases, 1.41 million new prostate cancer cases, and 1.2 million new skin cancer cases (Ferlay et al., 2021).

In terms of mortality, lung cancer led to 1.8 million deaths worldwide in 2020. Lung cancer is followed by colon and rectum cancer with 935 thousand deaths, liver cancer with 830 thousand deaths, stomach cancer with 769 thousand deaths, and breast cancer with 685 thousand deaths (Ferlay et al., 2021).

Also, about 70% of cancer-related deaths occur in middle- and low-income countries. This situation shows that there is an essential economic effect in the diagnosis and treatment of cancer (Ferlay et al., 2021).

Table 2.1. *Leading cancer types worldwide in 2020 in terms of new cases (incidence) and deaths (mortality) by sex* (Ferlay et al., 2021).

Men					
Incidance			**Mortality**		
First	**Second**	**Third**	**First**	**Second**	**Third**
Lung cancer	Prostate cancer	Non-melanoma skin cancer	Lung cancer	Liver cancer	Gastric cancer
Women					
Incidance			**Mortality**		
First	**Second**	**Third**	**First**	**Second**	**Third**
Breast cancer	Lung cancer	Cervical cancer	Breast cancer	Lung cancer	Cervical cancer

When evaluating the incidence and mortality by gender in 2020, the highest incidence in men is lung cancer (14.3%), followed by prostate cancer, with a slight difference (14.1%). However, when evaluating cancer-related deaths in men, although lung cancer leads (21.5%), liver cancer comes second (10.4%) (Table 2.1).

When examining the statistics in women, breast, lung, and cervical cancers are in the top three in both incidence and mortality, respectively. However, although breast cancer cases are relatively high (24.5%), they show a decrease in mortality (Table 2.1).

When evaluating the statistics, it is seen that the incidence of bone cancer is relatively low. It generally occurs as prostate cancer and lung cancer metastases in men. It is common for men with prostate cancer to metastasize to the bone (S. Kim et al., 2007). On the other hand, the metastasis of liver cancer to the bone is relatively low. However, some studies have shown that 50-70% of liver cancer metastasizes to the spine when it metastasizes to the bone (Rim et al., 2017). Like prostate cancer in men, breast cancer in women is the most common cancer that metastasizes to the bone. Breast and prostate cancers are the most common cancers causing metastatic bone cancer (Cecchini et al., 2005; Macedo et al., 2017).

When looking at the future predictions in cancer epidemiology, considering the current situation and the past three years, it is revealed that the diagnosis and treatment of cancer have been significantly hampered (Siegel et al., 2022). Because the COVID-19 pandemic started in China and spread worldwide in 2019, many people have been exposed to long quarantine periods. Also, it resulted in many hospital units being directed to COVID-19 patients. This situation has caused cancer and many diseases to be put on the back burner, and therefore, delayed their diagnosis and treatment. Patients with diseases such as cancer, for which early diagnosis and treatment are essential, have been much more affected by this situation. For this reason, it has been widely believed that cancer incidence will decrease for a short time and then increase as an advanced-stage disease. Therefore, cancer-based mortality will increase (Siegel et al., 2022).

2.1.3. Bone cancer

Bone cancers are divided into primary and secondary bone cancers. Primary bone cancer originates from bone cells. Its incidence and prevalence worldwide are pretty low. One can express it as one of the rare types of cancer because its prevalence is less than 1% compared to other types of cancer (http-1). Secondary bone cancers also appear as metastases of different cancer types (Macedo et al., 2017).

2.1.3.1. Primary bone cancer

Osteosarcoma, chondrosarcoma, and Ewing's sarcoma are the most common types of primary bone cancer (Ottaviani & Jaffe, 2009). Osteosarcoma tends to be seen in cells that play an active role in bone development. Therefore, one usually sees it in children and young adults having an active bone development stage. It is the third most common type of cancer after leukemia and brain tumors in children (Ottaviani & Jaffe, 2009).

Chondrosarcoma, another type of primary bone cancer, is a type of bone cancer that originates from cartilage tissue cells (chondrocytes) and progresses to the bone. Due to its metastatic characteristic from cartilage to bone, it may transform into dedifferentiated chondrosarcoma. Differentiated chondrosarcoma is a condition in which chondrosarcoma transforms into a sarcoma like an osteosarcoma (Sağlık, 2014). One sees chondrosarcoma in adults aged 40-70 due to age-related changes in cartilage tissue cells (http-1).

Ewing's sarcoma is one of the primary types of bone cancer and develops from mesenchymal stem cells. It can occur in any bone, but one usually sees it in the hip, upper leg and lower leg bones, and ribs. It can spread to intra-osseous and extra-bony soft tissues and rapidly proliferate and metastasize (Riggi & Stamenkovic, 2007).

2.1.3.2. Secondary bone cancer

Contrary to primary bone cancers, secondary bone cancers usually originate from different tissues and form through metastasis. For this reason, the probability of their occurrence is relatively high (http-1). Also, bones are the third most metastasized sites after the lung and liver (Macedo et al., 2017).

The metastasis mechanism is a multi-step mechanism. Proliferation starts with angiogenesis and then loss of cell-cell adhesion and continues with epithelial-mesenchymal transformation. Epithelial-mesenchymal transformation is a critical step for the metastasis of cancer cells. With this transformation, epithelial cancer cells are transformed into mesenchymal cells with increased motility and enter the systemic circulation. Afterward, it is possible to differentiate into different tissue types in the regions where they settle. In other words, this transformation allows the occurrence of intravasation and local invasion. In the last step of metastasis, adhesion and extravasation steps occur, in which the cancer cell in the circulation is kept in the vascular system of the corresponding region (Cecchini et al., 2005). Figure 2.2 shows a rough representation of these steps of metastasis.

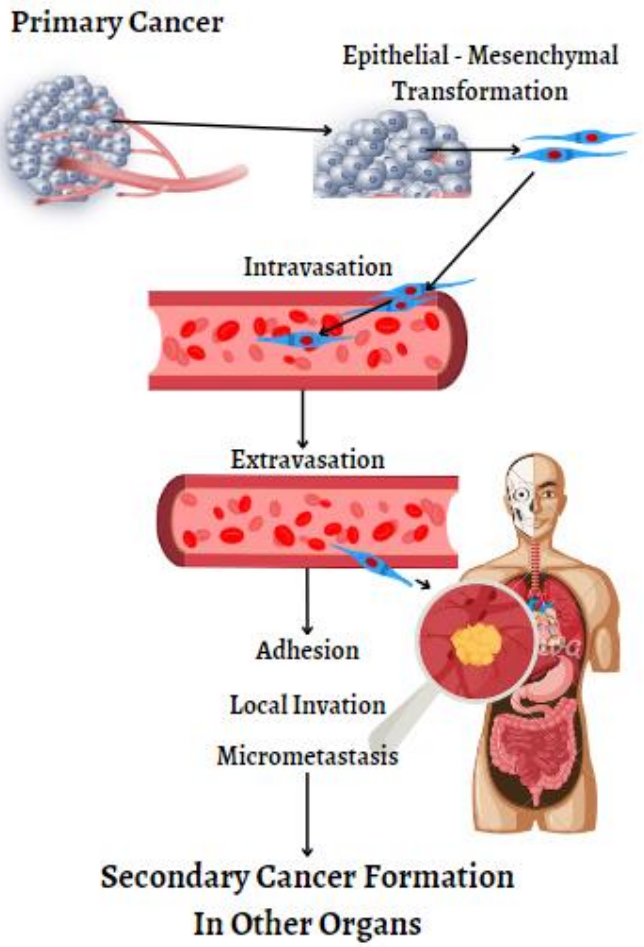

Figure 2.2. *Brief illustration of the steps of cancer metastasis*

Although one cannot clearly explain the reason for the possibility of more metastasis of cancer cells to specific regions, some studies have made some molecular and biological explanations for it (Cecchini et al., 2005; Mundy, 2002; Quayle et al., 2015; Roodman, 2004). Cancer stem cells entering the systemic circulation after epithelial-mesenchymal transformation perform multicellular aggregation using platelets and leukocytes. This aggregation allows their protection from the body's immune system while in circulation. In this way, they can hide from the immune system. This hiding mechanism also ensures the involvement of cancer cells in bone capillaries (Cecchini et al., 2005).

In addition, as stated in Paget's "Seed and Soil" hypothesis for metastasis, the microenvironment of the metastasis site is crucial (Paget, 1889). Accordingly, there should be a microenvironment to allow the cancer cell to grow and multiply in the region where the cancer stem cell is located. Otherwise, it cannot proliferate and multiply; in this case, metastasis will not occur (Paget, 1889).

In addition to all the general steps of metastasis mentioned above, bone cancer metastases target the axial skeleton, visualized in Figure 2.3(b), which usually consists of the bones of the head and torso. One of the main reasons why cancer stem cells specifically target the axial skeleton is that the axial skeleton has paravertebral structures. Paravertebral structures consist of paravertebral space (Figure 2.3(c)) and paravertebral junctions (Figure 2.3(a)). Paravertebral connections are connections with other organs such as blood vessels and nerves (Macedo et al., 2017). These connections increase the probability of primary cancers in other organs to the bones. For these reasons, if cancer in the organs is not diagnosed and treated early, the probability of metastasis to the bones is relatively high (Mundy, 2002).

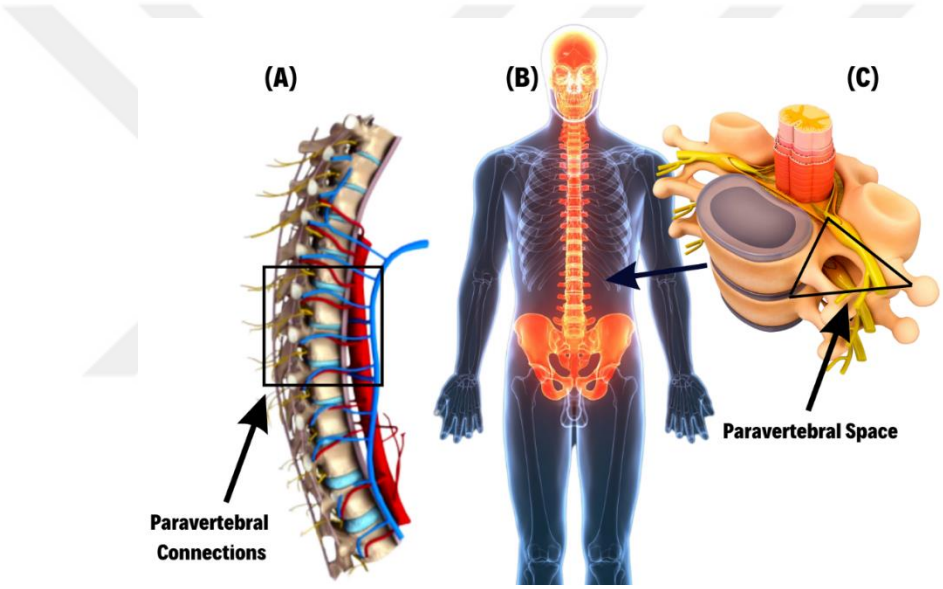

Figure 2.3. *(A) It is a rough representation of paravertebral connections such as vessels, nerves that may form connections with other organs. (B) A rough representation of the Axial Skeleton. (C) A rough representation of the paravertebral space.*

Primary cancer cells that metastasize to bones are not referred to as bone cancer in terms of histopathology but as cancer cells of the organ from which they originate. This situation is very critical for treatment. If one knows from which tissue or organ the metastasis has originated, one can perform the proper treatment type or method. However, at this stage, the effects of active agents used in chemotherapeutic treatment on bone cells should be well known (Mundy, 2002). Because secondary bone cancers differ due to metastases of different primary cancer types, a general treatment method may be ineffective. For example, a group of researchers showed that zoledronic acid-containing bisphosphonate, used in treating metastatic bone cancer originating from

prostate cancer, can cause bone osteonecrosis in the bones (Angel García Sáenz et al., 2007). In this case, when applying a treatment method specific to primary cancer cells that have metastasized to the bone, one should also consider the effects of the treatment method.

In addition, since the bone has different vascularization than other organs due to its structure, the body's immune mechanisms are also restricted from interfering with metastatic cancer in the bone. Thus, metastatic bone cancers proliferate and spread faster but may vary depending on cancer's origin. As with all types of cancer, angiogenesis is necessary for the growth and spread of metastatic bone cancers. However, in each of the primary and metastatic bone cancer types, it has been observed that microcapillaries structures having different densities (Kubo et al., 2013). This situation reveals the reason for the variability of growth and diffusion. However, this difference causes limited chemotherapy treatment in metastatic bone cancer types with low-density vascularization (Raymaekers et al., 2015).

2.2. Bone Anatomy

Before moving on to current treatment methods for bone cancer, it is essential to know the bone structure to understand these methods' limitations better. When examining the bone structure roughly, most cartilage structures are in the embryonic development stage. Over time, calcium salts accumulate in cartilage structures. With these accumulated calcium salts, the cartilage structures harden and become bones (Florencio-Silva et al., 2015).

Bone formation is called osteogenesis, and soft bone structure is called osteogen. Osteogenesis is a mechanism in which four primary bone cells play a role. These bone cells are osteoprogenitors, osteocytes, osteoblast, and osteoclast (Florencio-Silva et al., 2015).

Osteoprogenitors are osteogenic mesenchyme cells making up the bone cell. They are inactive in mature bone structures. When coming to bone formation or repair, they differentiate into osteoblasts (Florencio-Silva et al., 2015). Osteoblasts are responsible for bone formation. First, they provide the formation non-calcified bone structure called "osteoid". Then, they precipitate calcium and phosphorus ions by releasing the alkaline phosphatase enzyme. In this way, they provide calcification. Osteoblasts trapped in the calcified area are transformed into osteocytes, mature and viable bone cells (Florencio-

Silva et al., 2015). Osteocytes are located inside structures called lacunae and have cytoplasmic extensions. These cytoplasmic extensions connect them and provide nutrition and substance transfer to the bone tissue-restricted by the bone matrix's hardening (Florencio-Silva et al., 2015).

When the osteocytes lose their functions, the exchange of substances in the considering region is interrupted, and the bone tissue cannot be nourished. At this stage, osteocytes are resorbed by osteoclasts to ensure the continuity of bone tissue. This situation is called resorption. In this way, one provides that new bone cells are formed instead of osteocytes that have lost their function. Osteoclasts are responsible for bone destruction. For this reason, their cytoplasm contains abundant lysosomes. They soften the bone cells and the hard structure of the bone with the enzymes they have, such as acid phosphatase and collagenase (Florencio-Silva et al., 2015).

When examining the macrostructure of the bone, the bone has layers called the endosteum in the inner part and the periosteum in the outer part, preventing the bone's transverse growth and containing the vessels providing nutrition to the bone. These layers are responsible for bone growth, nutrition, and repair (Florencio-Silva et al., 2015). Osteocytes form the compact and spongy tissues of the bone. Tight bone tissues include the Haversian system, which contains the Haversian canal. Haversian canals are the canals of bone vessels that supply nutrients and oxygen to osteocytes. Volkmann canals connect them. Spongy bone tissues are composed of irregular spaces and contain bone lamellae containing red bone marrow (Florencio-Silva et al., 2015). These red bone marrows are the regions where blood cells are produced. In addition, the yellow bone marrow, found only in long bones in the skeletal system, is the region where white blood cells and platelets that provide the coagulation mechanism are produced. With this unique structure of bone, it is of vital importance to the body. The rough representation of the bone anatomy is as in Figure 2.4.

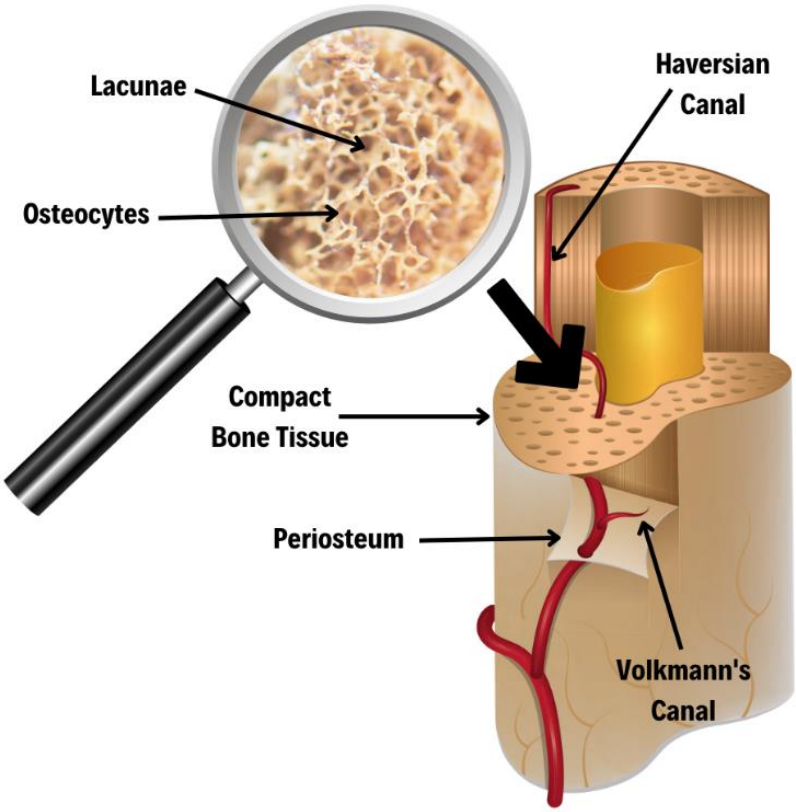

Figure 2.4. *Representation of the basic parts of bone structure*

2.3. Current Cancer Treatment Methods

Treating cancer occurring in the bone, one of the most metastasized body structures, should also be evaluated in many ways. Hence, the location, size, and origin of the cancerous region are significant. The fact that many parameters play such a role indicates the necessity of a multidisciplinary approach in the treatment of metastatic bone cancer. In this context, according to the bone cancer guidelines published and subsequently updated by the National Comprehensive Cancer Network, it has been reported that the treatment process of bone cancer is quite sensitive methods (Biermann, 2013; Biermann et al., 2017; Sybil Biermann et al., 2013). Therefore, it has been offered that a multidisciplinary team should work on treating bone cancer. Generally, one uses surgical intervention, radiotherapy, and chemotherapy methods. Although rare, one also uses ablation and embolization treatment methods (Biermann, 2013; Biermann et al., 2017; Sybil Biermann et al., 2013).

2.3.1. Surgical intervention

In surgical intervention, one cuts and removes the cancerous area. The location and size of the cancerous area determine the limits of surgical intervention.

Metastasectomy, rotationplasty, and limb-sparing resection are examples of such surgical interventions. With surgical interventions, depending on the condition of the cut area, sometimes one can make bone reinforcement from another part of the body or add artificial bone-like structures. Especially thanks to the developing tissue engineering, studies on systems that can imitate the strength and compatibility of the bone structure have started to increase (Collins et al., 2021; Guo et al., 2021; Marew & Birhanu, 2021; Simunovic & Finkenzeller, 2021; Y. Wang et al., 2021). Although surgical intervention techniques can currently treat the cancerous area, amputation of the limbs may be necessary in some cases (http-2). After amputation, integrating prostheses into the amputated places can be an extra burden for patients and their relatives, both financially and morally.

2.3.2. Radiotheraphy

Radiotherapy is widely used in the treatment of many types of cancer. It uses high-energy radiation to kill cancer cells. It is basically divided into external and internal radiotherapy. In external radiotherapy, one applies external radiation to the corresponding tissue of the patient using radiotherapy devices. On the other hand, in internal radiotherapy, one injects radiopharmaceuticals into the cancerous area of the patient and applies radiotherapy inside the body (Cravo & Mrsny, 2013).

In radiotherapy applications, radiation damages the DNAs of the tumor cells and prevents the proliferation of the cancerous area. Therefore, besides being used as a neoadjuvant treatment, it is also used as an adjuvant treatment method. However, during this treatment, it can also damage the DNA of healthy cells (Cravo & Mrsny, 2013). In this case, secondary cancer cases are experienced. There is even radiotherapy treatment among the risk factors for bone cancer (http-3; http-4).

2.3.3. Chemotheraphy

In chemotherapy, administration of chemotherapeutic with agents at high doses for specific periods can be done by local injection or injection into the entire systemic circulation. In this way, various therapeutic agents stop the vital activities of cancer cells and activate apoptosis or necrosis (Chou, 2010; Dai & Tan, 2015; Persidis, 1999).

The therapeutic indices of these agents are narrow, and their dose adjustment is quite sensitive; therefore, they can affect healthy cells and tissues. It has been even shown that long-term treatment using chemotherapeutic agents contributes to cancer metastasis and the development of multi-drug resistance mechanisms. Notably, it has

been found that the application of chemotherapy agents as monotherapy triggers these mechanisms (Chou, 2010; Dai & Tan, 2015; Persidis, 1999). One has begun combining chemotherapeutic agents used in monotherapy to prevent them. This therapy applied by combining chemotherapeutics is called combinational therapy. It provides a synergistic mechanism of action. In combination therapies, more than one chemotherapeutic agent is administered together. This therapy offers the opportunity to impact multiple pathways and mechanisms instead of affecting a single cancer pathway or mechanism (Minko et al., 2013; Shen et al., 2012). Although cancer patients are now trying to be treated using this therapy, chemotherapeutic agents are released into the whole body in this therapy. This situation may cause other diseases by affecting different mechanisms besides the formation of secondary cancer. In addition, chemotherapy treatment for bone cancer remains very limited. Due to the structure of the bone, its angiogenesis mechanism works differently, and its vascularization occurs through microcapillaries of different densities. These differences make it very difficult to transport chemotherapeutic agents to the corresponding bone area. In addition, like radiotherapy, one also sees chemotherapy as a risk factor for bone cancer. Especially, chemotherapy using drugs known as alkylating agents is a risk factor for bone cancer (http-4).

2.4. Targeted Drug Delivery Systems

2.4.1. Their historical background

Today, the inadequacy of the methods used for the treatment of cancer has led to an increase in studies on targeted drug delivery systems. German scientist Paul Ehrlich, who has worked in the fields of hematology, immunology, and antimicrobial chemotherapy, prepared the way for targeted drug delivery systems (Strebhardt & Ullrich, 2008; Winau et al., 2004). During his immunology studies, Ehrlich observed that antibodies target only pathogens and make them ineffective. With this observation, Ehrlich first introduced the "Magic Bullet" concept. In this concept, like a bullet, drugs reach the desired target without harming the healthy parts of the body and target only the microbes or bacteria that it thinks cause diseases. (Strebhardt & Ullrich, 2008; Winau et al., 2004). The development of the Magic Bullet was not only a pioneer of targeted drug delivery systems but also chemotherapy, one of the curing diseases methods using chemicals (DeVita & Chu, 2008; Strebhardt & Ullrich, 2008).

From Ehrlich to the present, targeted drug delivery systems have made significant progress. Especially considering the disadvantages and destructive effects of other treatment methods, the interest in targeted drug systems has increased, and one has focused on studies in this field (Bañobre-López et al., 2013; Barenholz, 2012; Beik et al., 2016; Guduru et al., 2013; Iyer et al., 2006; Jurgons et al., 2006; Khan et al., 2015; Rajabi et al., 2016; Rodzinski et al., 2016; Stimphil et al., 2017; Yue et al., 2012). Drug targeting and delivery systems has been developed and being still developed in this context.

Targeted drug delivery systems must have specific characteristics to offer the desired treatment opportunity. In this context, ideal targeted drug delivery systems must (Vasir & Labhasetwar, 2005);

- be able to direct/transfer the therapeutic agent to the desired tissue or area,
- maintain the therapeutic effect in the target area for as long as desired time,
- protect the therapeutic agent from metabolism and early release,
- be biocompatible, biodegradable, and non-toxic.

Tumoral cancer cells have heterogeneous, dynamic biology and can vary according to cancer type. Therefore, it is necessary to have sufficient knowledge of tumor cells' microenvironment, biology, and biophysical properties, as well as the mechanisms of action of drug systems and targeting systems to design a cancer-specific targeted drug delivery system (Vasir & Labhasetwar, 2005).

2.4.2. Their structure

Unlike the Magic Bullet, targeted drug delivery systems today have three essential components. While these were only the therapeutic agent and targeting part in the Magic Bullet, today, the carrier and the protective part is added to them (Pattni & Torchilin, 2015; Winau et al., 2004).

2.4.2.1. Carrier and protective part

The carrier and protective part is an essential part of targeted drug delivery systems. It enables not to opsonize and remove the therapeutic agent from the circulation by the body's reticuloendothelial system (RES). Also, it provides to transport of the agent to the targeted region without metabolism. For this, one designs and uses structures being familiar to RES, not a foreign substance (Lim et al., 2012). One can prepare these as different structures, such as polymeric systems, nanosuspensions,

nanoparticles, nanoliposomes, nanogels, and nano-sized carbon structures. There are carrier and protective structures used for many different purposes in the literature. But generally, natural, and synthetic polymers, micelles, dendrimers, nano capsules, nanoparticles, and liposomes are used (Torchilin, 2006). One determines the carrier and protective part according to the designed drug system. For example, pH-sensitive polymer coatings can be used for pH-sensitive systems (Du et al., 2011). Since these polymers only start to dissolve in the pH environment to which they are sensitive, they are an ideal carrier and protective part for pH-sensitive drug delivery systems. There are structures with different physical and biological sensitivities like these. However, the important thing is to choose the appropriate structure for the drug system to be designed (Torchilin, 2006).

In this study, solid lipids were used as the structure containing the active agent for the targeted delivery system. These solid lipids are lipids that are solid at room and body temperature and have been used frequently since the 1990s in the preparation of nanometer-sized colloidal drug delivery systems by stabilizing with surfactants. Solid lipid nanoparticles (SLNs) have been offered as an alternative to traditional carrier systems such as emulsion, liposome, and polymeric system (Souto et al., 2004).

SLNs do not include the problems seen in other drug delivery systems, such as encapsulation of water-soluble anticancer substances, providing controlled and prolonged release of the drug, and inability to protect the drug in the RES. SLNs are also suitable carrier systems for fat-soluble anticancer drugs and can slowly release the drugs they contain according to their lipid properties (Büyükköroğlu et al., 2016). Lipids used to prepare nanoparticles are biocompatible compounds with GRAS (Generally Recognized as Safe) feature. Triglyceride (tristearin, etc.), fatty acids (stearic acid, etc.), steroid (cholesterol, etc.) and waxes (cetyl palmitate, etc.) can be used as solid lipids.

Various types of surfactants can be added depending on their charge and molecular weight to stabilize the lipid dispersion. 1-5% surfactant or surfactant/cosurfactant mixture is used to ensure stability. Surfactant selection and concentration depend on the lipid and the route of application. For example, surfactants used in parenteral applications are more limited than dermal or oral applications (Mehnert & Mäder, 2012; Saupe & Rades, 2006).

Like this, one designs carrier and protective parts that differ according to their physical and chemical properties. These structures and other drug-targeting system structures define the system's overall size. The European Technology Platform has accepted the size scale of nanostructures to be applied in medicine as 1-1000nm (http-5). However, these sizes vary according to the region to be applied in practice (Wagner et al., 2006). Therefore, nanocarriers' size is a crucial factor in targeting systems.

2.4.2.2. Targeting part

Another critical component of targeted drug delivery systems is the targeting part. It is the most crucial part of the system as it is responsible for the targeting mechanism. Today, studies are still ongoing on different targeting structures. For this reason, various targeting mechanisms have emerged. Drug targeting mechanisms are basically divided into active and passive targeting (Bazak et al., 2015; Bertrand et al., 2014).

Passive targeting

In passive targeting, no targeting part exists. Therefore, one transports drug delivery systems physiologically by biodistribution and delivers them to the target. In passive targeting, targeting is based on the concept called Enhanced Permeability and Retention (EPR) effect. The EPR effect was observed by means of the accumulation of macromolecules at the tumor site for the first time (Matsumura & Maeda, 1986). The basis of the EPR concept is the differentiation of tumor vascularization. The vascularization of tumorous structures is generally heterogeneous compared to normal tissues. Also, their endothelial intercellular pores' widths are larger. Although the sizes of these pores vary depending on the tumor, they are generally around 100-780nm. The reason for such a wide size range is that the size of pores changes according to the disease's prognosis, type, and level. For example, some studies have reported that although the pore size of subcutaneous tumors increases up to the micron levels, they were generally between 380-780 nm (Hashizume et al., 2000; Hobbs et al., 1998). In a study on mice, the same cell lines were grown in two different media, and pore sizes were observed. According to the results, it was determined that the pore sizes of the tumoral structures grown in the subcutaneous microenvironment of the dorsal chamber were considerably larger than the pore sizes of the same tumoral structure grown in the pial microenvironment of the cranial window (Hobbs et al., 1998). Considering all these, it is concluded that tumoral structures significantly affect vascular pore size and

increase permeability compared to normal tissues (Vasir & Labhasetwar, 2005). In addition to this increase in permeability, the expression of growth factors such as vascular endothelial growth factor and basic fibroblast growth factor increases in tumor cells and their microenvironment. This increase leads to increased vasodilation and extravasation (Dellian et al., 1996; Vasir & Labhasetwar, 2005). When combining all these with the high permeability effect, one can perform passive targeting. The first FDA-approved passive targeting system-based nano-drug is Doxil, one of the best examples for passive targeting. Doxil has been formulated to reduce and balance the toxic effect of doxorubicin on healthy cells to treat metastatic ovarian cancer and many types of cancer. Polyethylene glycol coated liposome was used as a carrier and protective part in the formulation (Barenholz, 2012).

However, in some cases, the fact that each cancer type has different vascular permeability and microenvironment may prevent targeting based on the EPR concept. In addition, the lymphatic drainage system in tumor tissues or areas may become dysfunctional by suppressing it. In this case, a reverse pressure occurs in the interstitial environment in the corresponding region. This effect, called "Negative Interstitial Pressure," creates a mechanism of action opposite to the EPR effect. This pressure can restrict passive targeting. Since passive targeting systems have such barriers that block targeting drugs to corresponding regions, the scientific world has focused on active drug targeting systems (Vasir et al., 2006).

Active targeting

In active targeting systems, targeting parts that are appropriate to specific tissues and cells are used. According to their structures, active targeting systems are divided into sub-targeting groups, such as ligand-mediated targeting and chemical and physical targeting (Pattni & Torchilin, 2015; Schmaljohann, 2006).

In ligand-mediated targeting systems, various targeting molecules such as monoclonal antibody-enzyme conjugates, cytokines, glycoproteins, and viral proteins, which can bind to specialized molecular structures on the surfaces of the cells to be targeted, can be used. For providing successful and effective treatment using ligand-mediated drug delivery systems, one should develop systems that target receptors over-expressed in tumor cells (Morachis et al., 2012). For example, transferrin and folic acid receptors are over-expressed in many types of cancer (Kolhatkar et al., 2011). In ligand-mediated targeting systems, targeting the desired region can be succeeded by targeting

specifically these receptors. In the targeting method, biomarkers are significant to target the desired tissue or region. For example, the expression of CA-125, a biomarker for ovarian cancer, differs even in different cancer origins (Høgdall et al., 2007).

In the chemical and physical targeting methods, other active targeting methods, targeting is made by using the physical or chemical properties specific to the tissues. This targeting mechanism uses tissues' physical properties such as pH, temperature, and electrical. For example, the interstitial environment of cancer cells in their microenvironment may be at levels more acidic than that of normal cells. This acidic difference is a valuable parameter for many drug systems. Apart from the cancer microenvironment, the differentiating properties in cancer cells are also important parameters for drug systems. For example, compared with normal cells in terms of membrane potentials, it was found that cancer cells have higher depolarization than normal cells (O'Grady & So, 2005). In this way, one designs drug-targeting systems by considering the biophysical properties specific to cells (Pattni & Torchilin, 2015).

In targeted drug delivery systems, internal and external applications are made to release the drug after targeting the drug to the corresponding region. In internal applications, one generally aims at those cellular differentiations to trigger drug release. For example, by designing specific pH-sensitive systems, it is ensured that the drug is released according to the pH of the region (Huh et al., 2012). In external applications, after the drug delivery system is targeted to the desired area by applying a different application from the outside, external triggering can be made for the drug release. Today, one uses various systems for external applications. The drug is released by targeting the corresponding area with physical factors such as light, temperature, and magnetic field (Guduru et al., 2013; Huh et al., 2012; Schmaljohann, 2006; Yue et al., 2012). For example, gold nanoparticles are heat-sensitive structures and tend to aggregate in the heated region. In this way, one can target drug systems loaded with gold nanoparticles to the region by heating the corresponding area (Pattni & Torchilin, 2015).

Heating has also become a therapy for cancer, recently. In heat therapy, treatment with the hyperthermia method attracts a lot of attention because it both affects the vital enzymatic activities of cancer cells and increases the effects of chemotherapeutic agents (Agostinis et al., 2011; Falk & Issels, 2001; Hildebrandt et al., 2002; Wust et al., 2002). Nanotechnological developments paved the way for the nanomaterial-based

hyperthermia method. The nanomaterial-based hyperthermia method both provides targeted therapy and ensures that the hyperthermal impact does not affect healthy cells. Thus, it offered a more effective hyperthermia treatment. The working mechanism of the nanomaterial-based hyperthermia method is based on different physical infrastructures (Bañobre-López et al., 2013; Beik et al., 2016); "Photodynamic and Photothermal Therapy," "Magnetic Hyperthermia." In photothermal therapy, nanomaterials targeted to the cancerous area are exposed to near infrared laser light. These materials increase their energy by absorbing light. Thus, they enable the target area and cells to heat up. In this way, it offers a nano-hyperthermia treatment at the cellular level (Beik et al., 2016). On the other hand, in photodynamic therapy, photosensitive nanomaterials exposed to near infrared laser light are stimulated and pass to the triple state level. Photosensitive nanomaterials at the excited triple-state level provide to form singlet oxygen by transferring their energy to molecular oxygen. These oxygen radicals also cause the death of the cell (Agostinis et al., 2011). In both therapies, parameters such as the laser's wavelength, the nanomaterial's light sensitivity, and the energy required for excitation are critical (Benov, 2015; Chen et al., 2016).

One can also do a nanoparticle-based hyperthermia method using magnetic nanoparticles or nanomolecules. These magnetic nanoparticles resonate in the oscillating magnetic field, and because of the resonance, the temperature of the region increases. On the other hand, some magnetic nanoparticles can provide controlled hyperthermia by converting electromagnetic energy into heat energy in the magnetic field. In this way, they allow the temperature of the target region or cell to rise to 42 degrees (Bañobre-López et al., 2013; Beik et al., 2016).

As magnetic nanoparticles get smaller, they may gain ferromagnetic properties and not show hyperthermic properties. Therefore, this application is directly related to the sizes of magnetic nanoparticles (Bañobre-López et al., 2013). Since it offers a limited hyperthermia method, it does not provide a complete cure. However, the ferromagnetic property has brought a different targeted drug delivery system to the literature. In this method, one can direct and accumulate ferromagnetic or superparamagnetic nanoparticle-based drug delivery systems into the desired area under the magnetic field. Depending on the retention of therapeutic agent-loaded nanoparticles in this magnetic field, treatment of the cancerous area can be achieved (Jurgons et al., 2006).

In addition to using magnetic nanoparticles as a targeting component, one has also used materials with multiferroic properties as a drug-targeting component in recent years. These materials have two or more ferroic properties. In other words, these materials have at least two ferromagnetic, ferroelectric, and ferroelastic properties. Materials with ferroelectric and ferromagnetic properties are also called magneto-electric materials because these materials are in a structure that can be polarized electrically in the magnetic field or that can show magnetism in the electrical field. Drug targeting systems have been designed by utilizing these properties of multiferroic materials (Guduru et al., 2013; Rodzinski et al., 2016; Stewart et al., 2018; Stimphil et al., 2017; Yue et al., 2012). Since materials showing a magneto-electric (ME) effect can be electrically excited under a magnetic field and magnetized under an electrical field, they can direct to the desired region and create a nano-electroporation effect. The nano-electroporation effect can form nanopores in the cell membrane and carry the drug system into the cell by passing through these nanopores (Guduru et al., 2013; Rodzinski et al., 2016; Stimphil et al., 2017). In a study conducted by a research team at Florida International University and published in 2013, drug targeting was performed on human ovarian carcinoma cells using an average of 30-nm $CoFe_2O_4$-$BaTiO_3$ nanoparticles with ME effect (Guduru et al., 2013).

The basic targeting principle in this study is to ensure the uptake of therapeutic agents into the cell by accumulating MEN-based drug delivery systems under a DC magnetic field, utilizing the electrical polarization of the MENs triggered using the different electrical properties of cancerous and healthy cells membranes by this magnetic field, and creating nanopores large enough for the drug system to pass through the membranes by this electrical field. In this study, the team only tested the MEN-based drug systems they designed in cell culture. For this, by observing under a DC magnetic field of different intensities, they decided on the ideal DC magnetic field strength required for drug targeting systems to be taken into the cell. The same group then, together with a team from the University of Miami, conducted other studies in this area and published them in 2016 (Rodzinski et al., 2016). They conducted animal experiments with the same magneto-electric targeted drug system. In this experiment, they injected human carcinoma cells into the right-thigh of mice and produced an approximately 200 mm^3 tumor. Later, they were able to treat mice with the targeted drug system they designed. However, in this study and previous studies, while the DC

magnetic field can facilitate the uptake of the drug system into the cell, an extra AC magnetic field is needed to realize the drug release. In this study, they designed an AC magnetic field system for mice and continued treatment in that system. A different magnetic field is needed in these studies because the AC magnetic field can break the bonds between MENs and therapeutic agents, and the therapeutic agents are released (Guduru et al., 2013; Rodzinski et al., 2016).

2.5. Multiferroics

Multiferroics, one of the sub-topics of solid-state physics, has been the focus of many scientific studies today because multiferroic structures exhibit more than one ferroic or anti-ferroic properties in the same phase (J. Wang, 2016). The term "multiferroic" was first used by Schmid in his article, where he mentioned the different symmetries that allow two or more of the ferromagnetism, ferroelectricity and ferroelasticity properties to be in phase at the same time (Schmid, 1994). Of these properties, the intrinsic relationship of electricity and magnetism is one of the couplings that form the basis of modern physics. Due to this coupling, one can utilize both the charges and the spin of the electrons; thus, this coupling plays a crucial role in today's power plants, computers, mobile phones, and many other electronic devices. In particular, the magneto-electric effect, expressing the relationship between magnetic spin and electrical dipole, has the potential to make outstanding contributions to the spintronic industry, whose potential is to be used in computer systems (J. Wang, 2016).

Multiferroic structures are basically divided into two; type-I and type-II. Type-I multiferroic structures differ within themselves in terms of ferroelectricity (D. Khomskii, 2009; D. I. Khomskii, 2006; J. Wang, 2016). Type-I multiferroics are generally systems with structural units with temporary dipoles with polar groups such as BO_3, ferroelectric structures bonding hydrogen such as Rochelle salt, transition metal perovskites with transition metals such as $BaTiO_3$, perovskites having hexagonal $RMnO_3$ structure, materials usually containing Bi^{3+} or Pb^{2+} lone pair mechanism, and ferroelectric materials due to the charge arrangement. Type II multiferroics are spiral magnetic structures, structures with magnetostriction mechanisms, and structures showing ferroelectric properties with the electronic mechanism in blocked magnets (Zvezdin et al., 2006).

As mentioned in the previous paragraph, there are many materials having different ferroic properties in the literature. Today, however, structures with magneto-electric properties come to the fore. Magneto-electric properties are based on magnetism and electrical polarization. When comparing magnetism and electrical polarization in terms of physical interpretation, one can easily express the concept of magnetism with well-defined quantities. For example, one can easily define the magnetization of a ferromagnetic material or the sub-lattice magnetization of an antiferromagnetic material by the ‹M› and ‹L› quantities, respectively. However, this is not the case with electrical polarization. The value of the unit cell selected in the material for polarization can be impactful. Therefore, one cannot clearly define the value of polarization. However, one can determine its change under external exposures as a net quantity. For this reason, one should use methods such as the Berry phase and Berry curvature to calculate the polarization theoretically (D. Khomskii, 2009; D. I. Khomskii, 2006; Sui et al., 2015; J. Wang, 2016).

The basis of the berry phase is based on the adiabatic theorem in quantum mechanics. According to the adiabatic theorem, when changing the Hamiltonian of a system slowly, the system remains in the time-dependent ground state. However, there is no time dependency in the Berry phase. If Hamiltonian is in a closed loop in the parameters space, an irreducible phase towards the initial state may occur. In solid-state physics, one also expresses the parameter space as electron momentum. The change in electron wave function is also associated with the Berry phase and curvature (Bérard & Mohrbach, 2006; Bruno et al., 2004; Samuel & Bhandari, 1988; Xiao et al., 2010).

For the berry phase equation, first, some quantum mechanical reformulations are required.

$$\vec{R}(t) = (R_1, R_2, R_3, \dots., R_n) \tag{2.1}$$

Equation 2.1 expresses the time-dependent Hamiltonian parameters. One can write Hamilton as equation 2.2 for each eigenvalue and eigenvector with the wave function. In this equation, $E_n(\vec{R}(t))$ denotes eigenvalues while $|\psi_n(\vec{R}(t))\rangle$ denotes instantaneous eigenstates/vectors.

$$\hat{H}(\vec{R}(t))|\psi_n(\vec{R}(t))\rangle = E_n(\vec{R}(t))|\psi_n(\vec{R}(t))\rangle \tag{2.2}$$

One uses the geometric phase for the time-independent Berry phase. One can express the geometric phase as in equation 2.3.

$$\gamma_n(t) = i\int_0^t \left\langle \psi_n(\vec{R}(t')) \middle| \frac{d}{dt'}\psi_n(\vec{R}(t')) \right\rangle dt' \tag{2.3}$$

The expression $\frac{d}{dt'}\psi_n(\vec{R}(t'))$ can be written as in equations 2.4 by applying the Chain Rule.

$$\frac{d}{dt'}\psi_n(\vec{R}(t')) = \frac{\partial\psi_n}{\partial R_1}\frac{dR_1}{dt} + \frac{\partial\psi_n}{\partial R_2}\frac{dR_2}{dt} + \cdots = (\nabla_{\vec{R}}\psi_n)\cdot\frac{d\vec{R}}{dt} \tag{2.4}$$

When substituting Equation 2.4 in the geometric phase, the Berry phase equation expressed as in Equation 2.5 is obtained.

$$\gamma_n(t) = i\int_{\vec{R}(0)}^{\vec{R}(t)} \langle \psi_n(\vec{R}) | \nabla_{\vec{R}}\psi_n(\vec{R}) \rangle \, dR \tag{2.5}$$

This can be calculated if Hamiltonian is in a closed loop, $\vec{R}(0) = \vec{R}(t)$ (Bruno et al., 2004; Samuel & Bhandari, 1988; Xiao et al., 2010).

2.5.1. Magneto-electric effect

The history of magneto-electric structures begins in Curie's article in 1894, in which he expressed the possibility of a combination of magnetic and electrical properties in a structure or material (Curie, 1894). Although multiferroic properties were expressed in the book written by Landau and Lifshitz in 1959, there was no observed pattern (Landau et al., 2013). However, in the same year, in an article written by Dzyaloshinskii, he suggested that the antiferromagnet Cr_2O_3 material should exhibit linear magneto-electric properties (Dzyaloshinskiĭ, 1960). The following year, Astrov, working on this effect, observed the magneto-electric effect in Cr_2O_3 (Astrov, 1960). Then in 1966, Ascher and his team discovered the first multiferroic material (Ascher et al., 2004).

The magneto-electric effect is the condition in which a magneto-electric material can be electrically polarized and magnetized by magnetic field exposure or, vice versa, magnetized and electrically polarized by electrical field exposure. We can physically explain this relationship with the following system of equations (J. Wang, 2016):

$$P_i = \alpha_{ij}H_j + \beta_{ijk}H_jH_k + \ldots \tag{2.6}$$

$$M_j = \alpha_{ji}E_i + \beta_{jik}E_iE_k + \ldots \tag{2.7}$$

Here, P denotes electrical polarization, M denotes magnetization, and α denotes the ME coefficient. The linear ME effect can be expressed simply by ignoring the

quadratic terms in Equations 2.6 and 2.7, considering only the first-order terms and including the free energy term (Eq. 2.8-2.10).

$$F_{ME} = -\alpha_{ij} E_i H_j \tag{2.8}$$

When substituting the free energy term of equation 2.8 in equation 2.6 or 2.7, one obtains the polarization equation 2.9 and the magnetization equation 2.10 (J. Wang, 2016).

$$P = -dF / dE \tag{2.9}$$

$$M = -dF / dH \tag{2.10}$$

The ME coefficient is a tensor that can have symmetrical and anti-symmetrical components. The symmetrical component of this tensor can be mathematically expressed with the Kronecker symbol (δ_{ij}) in a diagonal form as in equation 2.11 (J. Wang, 2016).

$$\alpha_{ij} = \alpha_i \delta_{ij} \tag{2.11}$$

If expressing the symmetrical component as in equation 2.11, the polarization component connected to the magnetic field is positioned in parallel with the magnetic field.

One uses the anti-symmetric Levi-Civita symbol (ε_{ijk}) to express the anti-symmetric component of the ME tensor mathematically. For this, one equalizes the product of the ME tensor with the symbol Levi-Civita to a pseudovector, also known as the toroidal moment (Equation 2.12). This pseudovector determines whether the polarization and magnetization are perpendicular to the exposed external fields (J. Wang, 2016).

$$T_i = \varepsilon_{ijk} \alpha_{jk} \tag{2.12}$$

These parameters help explain symmetry based on spatial inversion (J) and temporal reversal (T) concepts. These symmetries form the basis of the ME effect. A ME effect occurs when only these symmetries are broken in a system or material. While the electrical vectors of the ME effect change sign under spatial inversion, magnetic vectors change signs under temporal reversal (Equations 2.13, 2.14).

$$
\begin{aligned}
J\ P &= -P \\
J\ E &= -E \\
J\ M &= M \\
J\ H &= H
\end{aligned}
\tag{2.13}
$$

$$
\begin{aligned}
T\ P &= P \\
T\ E &= E \\
T\ M &= -M \\
T\ H &= -H
\end{aligned}
\tag{2.14}
$$

In this context, the product of spatial inversion and a temporal reversal is conserved for the ME effect. However, this product is not conserved in multiferroic structures (J. Wang, 2016).

2.5.2. Targeted drug delivery mechanism with magneto-electric effect

MENs should not be confused with magnetic nanoparticles (MNs), superparamagnetic iron oxides, or other superparamagnetic, ferromagnetic, ferrimagnetic nanoparticles used in drug targeting and medical imaging. Although MENs, like MNs, have a non-zero magnetic field, unlike MNs, they have an intrinsic electrical field that can be controlled externally. This controllable electrical field underlies the interaction between the drug system and specific cells (Stimphil et al., 2017).

One can apply MENs with two primary methods systemic and local. In local application, they are either injected directly into the tumor area or injected into the vessels, targeting them to the corresponding region by magnetic field exposure. In systemic application, one applies them intravenously and ensures they are targeted to the corresponding region with magnetic field application. In both cases, the selectivity and targeting of the drug system by cells is succeeded by a certain physical infrastructure (Guduru et al., 2013; Rodzinski et al., 2016; Stewart et al., 2018; Stimphil et al., 2017; Yue et al., 2012).

One can target MENs to whole cells and cell populations. MENs create a unique electrical field that can be stimulated externally by applying a magnetic field, thus creating a nano electroporation effect unique to cancer cells without damaging the healthy cells around them. At that point, the localization distance of the electrical field produced by the nanoparticles is defined by the dimensions of the nanoparticles (Stimphil et al., 2017).

As a result, controlling MENs with a magnetic field increases selectivity towards cancer cells, strengthens penetration into cancer cells, and enables the control of drug release.

The electrical field produced by MENs at a point on the cell membrane is formulated as the following equation;

$$E = k\frac{3(p.\check{r})\check{r}-p}{r^3} + \frac{kQ}{r^2}\check{r} \tag{2.15}$$

Here k is the Coulomb constant, p is the dipole moment of the MENs, Q is the electrical charge of the MENs, and r is the distance between the MENs and a point on the cell membrane.

The following equation expresses the dipole moment MEN.

$$p = \alpha H \tag{2.16}$$

In the electric field formula in equation 2.15, one determines the first term by the electrical dipole moment triggered by the magnetic field. One defines the second term by the surface electric charge that occurs according to colloidal chemistry when MENs are in a solution or plasma. In this case, a double-charged layer forms around the surfaces of the MENs due to the interaction of chemical and electrical forces. The zeta potential measurement determines this surface charge. However, the surface charge depends on the magnetic field to be applied. As the applied magnetic field increases, the surface charge also increases (Stimphil et al., 2017).

MENs and cell membranes have the same charge polarity, so they can easily pass-through capillaries without being engulfed by surrounding cells. However, while circulating, MENs pass very close to the cells (about one micron). At the same time, the electrical field (about 0.1V/μm) created by the applied magnetic field easily triggers the local dielectric breakdown in cancer cells. In contrast, the electrical field (about 1.5V/μm) must be higher for healthy cells to be affected. Thus, dielectric breakdown of healthy cells cannot be easily triggered. One knows that the conductivity of the membranes of cancer cells is approximately three times higher than that of normal cells. This high conductivity creates an attraction force between MENs and cancer cells due to the electrostatic mirror effect (Stimphil et al., 2017).

In the first-order approach, the membrane has two different states. One of them is the normal state of the membrane, in which case the membrane is non-conductive. In this case, one repels negatively charged MENs by the negatively charged membrane. In

contrast, during the nano electroporation process, the conductivity of cancer cells increases, and they begin to attract MENs. According to the “mirror image” model, this gravitational force can be formulated as the following equation (Stimphil et al., 2017);

$$F_m = \frac{kQ^2}{4r^2} \tag{2.17}$$

Since the effective surface charge depends on the magnetic field, the gravitational force also depends on the magnetic field. Here, to calculate the cut-off distance “r” and find the attraction force, the surface charge “Q”, which is dependent on the magnetic field, is found by measuring the zeta potential “V(H)” in phosphate buffered solution (PBS), like the plasma pH level using the formula below (Stimphil et al., 2017).

$$Q = V(H)d/k \tag{2.18}$$

One also uses the following formula for the cut-off distance.

$$r_c = 0.5\sqrt{\frac{kQ}{E}} \tag{2.19}$$

Based on this, the following conclusion is reached: If the applied magnetic field power is increased, the critical distance increases. This increase increases the number of nanoparticles that can trigger nano electroporation in that region, which increases the selectivity of the targeting method. Also, this electrical field provides high selectivity and forms nanopores on the membrane by taking advantage of the electrical properties of the cell membrane. In this way, one ensures that pathways are opened to facilitate the uptake of the drug system into the cell. As it is known, the cell membrane has an electrically polarizable environment due to its ion channels and lipid structure. The electrical charge of the cell membrane also depends on many internal and external factors. For example, it depends on many cellular variables such as the cellular microenvironment, pH, ion channels, etc (Stimphil et al., 2017).

2.6. MEIS and Associated Factors in Tumorogenesis

MEIS proteins play significant roles in cancer processes such as tumorigenesis, metastasis, and invasion. They can have different regulations in different cellular environments. Also, they are misregulated in various cancers. For example, while they have upregulation in pancreatic cancer, downregulation in colon cancer. In addition, they and their factors can used as biomarkers for many diseases (Girgin et al., 2020).

Therefore, recent therapeutic approaches involving the function of MEIS and factors in MEIS-associated cancers are being investigated (Girgin et al., 2020).

MEIS1, a member of the Three Amino Acid Loop Extension (TALE) type class of the homeobox gene family, is one of the main regulators of self-renewal of hematopoietic stem cells (HSC). Therefore, research is being done on its use as a potential therapeutic agent. MEIS1 have been investigated and MEIS1 inhibitors that can modulate HSC activity have been developed. For this purpose, a library of homeobox family inhibitors was constructed and the homeodomain of MEIS proteins were screened using AutoDock Vina and the PaDEL-ADV platform (Aksoz et al., 2018; Turan et al., 2020).

It is known that MEIS proteins expressed in many tissues are associated with many types of cancer and form complexes with cell DNA, leading to the development of drug resistance in cancerous cells. MEIS1 protein inhibitor has been shown to inhibit over 95% of MEIS-luciferase activity at 1 μM doses. In addition, inhibitor of MEIS protein was determined to downregulate MEIS target gene expression. In addition, it has been determined that this inhibitor is effective in preventing drug resistance and reducing the rate of metastasis (Aksoz et al., 2018; Turan et al., 2020).

2.6.1. MEIS and cancer

MEIS1 was first identified in the mouse model of leukemia. MEIS1, belonging to the TALE transcription factors 1 class, cooperates with PBX1 and HOXA9 transcription factors. They are characterized by PBX interaction domains (Turan et al., 2020).

Types of cancer such as breast cancer depend on hormones such as estrogen. It was determined estrogen receptor induces upregulation of MEIS1 and Forkhead box P3 (FOXP3) in breast cancer. MEIS1-FOXP3 interaction can increase the expression of cancer-associated genes. Also, it was suggested that co-expression of MEIS1 with TMEM25 and REPS2 can be a marker for breast cancer. High expression of MEIS1, TMEM25 and REPS2 is a determining factor for assessing the likelihood of breast cancer recurrence and survival. Also, mutation of the HOX/PBX/MEIS interactions may also contribute to development of breast cancer. Considering all of these, it can conclude that MEIS1 and associated factors function as oncogenic in cancer development and progression (Turan et al., 2020).

Homeobox proteins called HOX are transcription factors that play a role in growth control and cell differentiation during embryogenesis. In addition to homeostasis, they also play important roles in oncogenesis when they are expressed sporadically in cells. Their expression and functions in cancers are tissue-specific. MEIS and PBX, being TALE homeobox proteins, act as a cofactor for HOX proteins (Girgin et al., 2020).

In the thesis study, MEIS protein inhibitor, which was developed by Fatih Kocabaş and his team and was patented from the European patent institute with the number EP3541410A2, was used as an active agent.As mentioned in “Introduction” part, different chemotherapeutic agents with different effect mechanism are used for each cancer type. In this study, a MEIS1-protein inhibitor, a new one of them, was used (Aksoz et al., 2018; Turan et al., 2020; Turgutalp et al., 2021).

3. MATERIAL AND METHOD

3.1. Utilized Units

In this thesis study, one used the Anadolu University Faculty of Pharmacy Pharmacy Technology Department Laboratory, Anadolu University Plant, Medicine and Scientific Research Application and Research Center, and Anadolu University Faculty of Pharmacy Doping and Narcotic Substances Analysis Laboratory facilities for the preparation and evaluation of nanostructures and formulations. One made service procurement from different universities for the characterization of nanostructures and formulations. The unit from which one purchased the service for each characterization is detailed in the corresponding headings.

3.2. Utilized Materials

In this study, one used the materials in Table 3.1. However, in addition to these materials, MEIS protein inhibitor was used as an anti-cancer agent. The conjugation of the MEIS1 protein inhibitor and the magnetoelectric carrier system was performed.

Table 3.1. *A list of utilized materials in the study.*

NAME	PURPOSE of USAGE
Cobalt Nitrate Hexahydrate	For magnetoelastic core structure
Iron (III) Nitrate Nonahydrate	For magnetoelastic core structure
Polyvinylpyrrolidone	For magnetoelastic core structure
Sodium borohydride	For magnetoelastic core structure
Barium Carbonate	For piezoelectric shell structure
Citric Acid	For piezoelectric shell structure
Titanium (IV) isopropoxide	For piezoelectric shell structure
Ethanol Solution	For piezoelectric shell structure
Falcon tube (conical bottom, 50 mL)	For use at all stages of study
Flask (filtered, sterile, T.C. treated, 75 cm^2)	For cell culture experiments
96-well plate (transparent, T.C. Treated, with lid)	For cell culture experiments
Micro test tubes (1.5 & 2.0 mL)	For use at all stages of study
Dulbecco's Modified Eagle Medium (DMEM)	For cell culture experiments
24-well plate (transparent, T.C. Treated, sterile, capped)	For cell culture experiments
Fetal bovine serum (sterile, suitable for cell culture)	For cell culture experiments
Dimethylsulfoxide (DMSO)	For cell culture experiments
MTT dye 98% (570 nm wavelength)	For cell culture experiments
Trypsin/EDTA 0.25% (100 mL)	For cell culture experiments

Table 3.1. (Continued) *A list of utilized materials in the study.*

Penicillin/Streptomycin	For cell culture experiments
1XPBS buffer liquid	For cell culture experiments
Tween®80	For solid lipid coating
Gelucire® 44/14	For solid lipid coating
Gelucire® 50/13	For solid lipid coating
Dichloromethane	For solid lipid coating

3.3. Utilized Devices and Equipment

Table 3.2 shows the devices and equipment used in this study. In addition to these devices, one also used devices from different institutions and different units. These devices are not listed in Table 3.2 but are discussed in detail in the next sections.

Table 3.2. *A list of utilized devices and equipment in the study.*

NAME	BRAND/MODEL	PURPOSE of USAGE
pH Meter	Ohaus ST 3100 F	For pH measurement
Adjustable Volume Automatic Pipette (100-1000 μL)	Eppendorf Research Plus	For use at all stages of study
Adjustable Volume Automatic Pipette (20-200 μL)	Eppendorf Research Plus	For use at all stages of study
Rechargeable Pipette	Eppendorf Easy Pet 3	For use at all stages of study
Adjustable Volume Automatic Pipette (500-5000 μL)	Eppendorf Research Plus	For use at all stages of study
Large Capacity Centrifuge	Eppendorf 5810	For synthesis and cell culture
Incubator with CO_2	Hera Cell 240i	For cell culture
Multi Reader	Perkin Elmer Victor X5	For cell culture viability tests
Distilled Water Device	Millipore	For use at all stages of study
Deep-freezer (-20°C)	Arçelik	For temperatures higher than -20°C
Deep-freezer (-80°C)	New Brunswick Sci.	For temperatures higher than -80°C
Fluorescent Microscope	Leica 400DMI	For sterilization in cell culture
Laminar Flow Cabinet	Heal Force	For cell culture
Mechanical Mixer	Silent Crusher S Heidolph	For use in all stages
Microcentrifuge	Eppendorf	For synthesis and cell culture
Zeta Potential and Particle Size Meter	Nano Zetasizer ZS Malvern	For determining the particle sizes & zeta potentials
Vortex	Jeio Tech Co.	For use at all stages of study
Water Bath	GFL T-251425	For degassing and thawing

Table 3.2. (Continued) *A list of utilized devices and equipment in the study.*

Sonicator	Sonics	For use in the synthesis
Rotavapor	Buchi R-205	For use in the synthesis
Autoclave	Hirayama	For sterilization of all materials
Inverted microscope	Leica DMIL	For cell culture
Ultra Pressure/Performance Liquid Chromatography	Agilent	For analytical method development and validation

3.4. Synthesis of Magneto-Electric Nanoparticles

One uses many different chemical synthesis methods in the literature during the synthesis of MENs. However, in this thesis, MENs were synthesized by the hydrothermal synthesis method, which is one of the most widely used synthesis methods. According to this method, in the synthesis phase of biphasic MENs, one makes two separate syntheses for the core and the shell. Afterward, one combines the two phases.

Hydrothermal synthesis method steps (Etier et al., 2012; Guduru et al., 2013; Stewart et al., 2018):

- First, $CoFe_2O_4$, a core magnetoelastic nanostructure, is synthesized. For this, 0.058g $Co(NO_3)_2*6H_2O$ and 0.16g $Fe(NO_3)_3*9H_2O$ are dissolved in 15ml ultra pue water (UPW).
- One mixes it with a 5 ml UPW solution containing 0.2g of polyvinylpyrrolidone and 0.9g of sodium borohydride. Then, this mixture is stirred at 120°C for 12 hours to allow the reaction to continue.
- Afterward, the gel-like ferroic liquid is dried at 80°C to obtain $CoFe_2O_4$, core magnetoelastic nanostructures. These structures are defined as MN in the following sections.
- These nanostructures washed with UPW are subjected to a decantation process. Then, it is dried again and exposed to 750°C in the muffle furnace to prevent possible chemical contamination.
- After synthesizing the core structures, one prepares the $BaTiO_3$ precursor solution. For this, 30 ml of UPW solution containing 0.029g $BaCO_3$ and 0.1g citric acid is mixed with an ethanolic solution containing 1g citric acid and 0.048 ml titanium (IV) isopropoxide.

- For synthesizing the $CoFe_2O_4$-$BaTiO_3$ nanostructure, 0.1g of $CoFe_2O_4$ core structure is mixed with the obtained $BaTiO_3$ precursor solution. After a titanium alloy (Ti_6Al_4) head with a radius of 3mm and a length of 137mm is attached, one sonicates the mixture at 40% of the maximum frequency (20 kHz) for approximately 1-2 hours until completely dispersed.
- As soon as the $CoFe_2O_4$ particles are completely dispersed, the mixture is dried at 80°C with continuous stirring.
- The dried powder is placed in a muffle oven and exposed to 750°C for 5 hours, and MENs are obtained by cooling in a controlled manner.
- Finally, the decantation process is applied to UPW-dissolved MENs to ensure decontamination. The remaining product is dried in the oven again to obtain ideal MENs.

3.5. Preparation of Solid Lipid Coated MN and MEN Formulation

Solid lipids Gelucire® 44/14 with a melting temperature of about 44°C and Gelucire® 50/13 (Gattefosse, Cedex, France) with a melting temperature of 50°C were selected as the lipids to be used for loading the MEIS1 inhibitor into MNs and MENs. Separate formulations were prepared to determine the effects of these lipids used in the system to be prepared, the effects of the MEIS1 inhibitor together with lipids, and the comparative effects of ME and MEN with the lipid-coated formulations.

3.5.1. Preparation of solid lipid nanoparticles

Solid lipids Gelucire® 44/14 and Gelucire® 50/13 (Gattefosse, Cedex, France) were used to prepare the formulations. The solvent emulsification/evaporation method was used in the formulations prepared with Gelucire® 44/14 (Büyükköroğlu et al., 2016), and the simple emulsion preparation method was used in the formulations prepared with Gelucire® 50/13 (Büyükköroğlu et al., 2015).

Formulations prepared with Gelucire® 44/14: 500 mg of Gelucire® 44/14 was used for each of the formulations. After weighing 500 mg of lipid, it was taken into a pressure balloon and completely dissolved in 5 ml of Tween 80 (5% g/v) and dichloromethane mixture. 10 ml ultrapure water containing 4% Tween 80 was added to this mixture and sonication was performed at 70% power for 1 minute for emulsification. The milk-colored emulsion formed in the balloon was immersed in a water bath at 350 mbar and 60 ºC in a rotavapor and rotated at 50 rpm for approximately

1 hour to remove the organic phase from the environment. The resulting solid lipid dispersion was stored at room temperature until use.

Formulations prepared with Gelucire® 50/13: 500 mg of Gelucire® 50/13 was weighed into a 15 mL test tube, and solid lipid was dissolved by immersing it in a 60 ºC water bath. 10 ml of ultrapure water containing 4% Tween 80 heated to 60 ºC in a separate container was added and sonicated at 70% power for 1 minute for emulsification. Consideration was given to controlled cooling of the formulation to room temperature and stored at room temperature until use.

3.5.2. Preparation of solid lipid nanoparticles containing MEIS1 protein inhibitor

For Gelucire® 44/14: As the MEIS1 protein inhibitor is completely dissolved in ethanol, a 1:1 ml mixture of ethanol and dichloromethane with pre-prepared surfactant was prepared. 5 mg of MEIS1 protein inhibitor was added to this mixture and dissolved with the help of a sonicator. By adding 500 mg of Gelucire® 44/14 on it, the lipid was also dissolved. 10 ml of ultrapure water containing 4% Tween 80 was added to this mixture and emulsification and evaporation were carried out as mentioned above. The obtained solid lipid formulation loaded with MEIS1 inhibitor was stored at room temperature until use.

For Gelucire® 50/13: 5 mg of MEIS1 protein inhibitor was weighed into a balloon, and a clear solution was obtained by adding 6 mL of ethanol: dichloromethane (1:1 v/v) mixture. Then, the balloon was immersed in a water bath at 60 ºC to remove the organic phase, and it was rotated in a rotavapor at 350 mbar and 50 rpm for approximately 1 hour. 10 ml of ultrapure water containing 4% Tween 80 heated to 60 ºC was added onto the lipid layer containing MEIS formed on the balloon surface and sonicated at 70% power for 1 minute for emulsification. Attention was paid to controlled cooling of the obtained dispersion to room temperature and stored at room temperature until use.

3.5.3. Coating of MNs and MENs with a lipid layer

For Gelucire® 44/14: Since MNs can be dispersed in dichloromethane mixture with pre-prepared surfactant, no alcohol content is used in any way. After 500 mg of Gelucire® 44/1 was dissolved in 5 ml of dichloromethane with surfactant, 5 mg of MN was added and dispersed with the help of a sonicator. Afterwards, 5 ml of ultrapure water was added and sonicated again, and the emulsion was stored by evaporation as described in 3.5.1.

For Gelucire® 50/13: 5 mg of MN and 500 mg of Gelucire® 50/13 were taken into a balloon, 6 mL of ethanol: dichloromethane (1:1 v/v) mixture was added on it to dissolve the lipid and to ensure homogeneous dispersion of MNs. minute sonicated. Then, it was evaporated to remove the organic solvent from the environment and emulsified with 10 mL of heated water containing surfactant.

The same lipid coating procedure for MNs was applied for MENs.

3.5.4. Coating of MNs and MENs with a lipid layer containing MEIS1 protein inhibitor

For Gelucire® 44/14: For this formulation, first of all, 5 mg of MEIS protein inhibitor was dissolved in a 1:1 ml mixture of ethanol and dichloromethane with pre-prepared surfactant with the help of a sonicator. After it was completely dissolved, 500 mg Gelucire® 44/14,5 mg MN and 5 ml ultrapure water were added to the mixture and sonicated again. After emulsification, the organic phase was removed with the help of a rotavapor. This procedure has also been applied to MENs.

For Gelucire® 50/13: For MN and MEN formulations containing MEIS, 5 mg of MEIS was added to the organic solvent in which the lipid was dissolved, and the MN was dispersed, and dissolved by sonication. As a result of evaporation of the organic solvent, dispersions were prepared by adding aqueous phase on the mixture of MEIS, MN and lipid on the balloon wall. This procedure has also been applied to MENs.

The codes and contents of the formulations are presented in Table 3.3.

Table 3.3. *The codes given to the prepared formulations and their contents.*

	Codes	Lipid(mg)	Tween 80 (%)	D.water (mL)	MN (mg)	MEN (mg)	MEIS (mg)
Gelucire 44/14	G44	5	9	10	-	-	-
	MS44	5	9	10	-	-	5
	MN44	5	9	10	5	-	-
	MEN44	5	9	10	-	5	-
	MS44MN	5	9	10	5	-	5
	MS44MEN	5	9	10	-	5	5
Gelucire 50/13	G50	5	4	10	-	-	-
	MS50	5	4	10	-	-	5
	MN50	5	4	10	5	-	-
	MEN50	5	4	10	-	5	-
	MS50MN	5	4	10	5	-	5
	MS50MEN	5	4	10	-	5	5

3.6. Analytical Method Development and Validation

Agilent brand Ultra Pressure/Performance Liquid Chromatography (UPLC) device in Biotechnology Laboratory at Anadolu University was used in the quantification of MEIS protein inhibitor. The analysis conditions and materials are shown in Table 3.3.

Table 3.4. *UPLC analysis conditions*

Device	Agilent 1290 Infinity LC System
Column	GraceSmart RP18 150 mm x 4.6 mm
Column Temperature	40 °C
Mobile Phase	Acetonitrile (1% O-phosphoric acid)/Ultra Purified Water (1% O-phosphoric acid) (60/40)
Dedector	Max-Light Cartride Cell
Wavelenght	258 nm
Flow Rate	0.670 mL. s^{-1}
Volume of Injection	5 µL
Device	Agilent 1290 Infinity LC System

3.6.1. Validation study

The purpose of performing analytical method validation is to prove the accuracy and reliability of the method used.

3.6.1.1. Linearity

The linearity study is carried out to express that the analysis results increase in direct proportion with the increase in the amount of active agent in the samples at different concentrations obtained by the serial dilution method from the stock solution prepared at a certain concentration. Analyzes should be done with at least 5 different concentrations (ICH, 2005).

In this study, 6 serial samples were prepared from 9 different concentrations in the concentration range of 5-100 µg. mL^{-1} to obtain the standard regression curve of MEIS1 to be analyzed by UPLC method. As a result of the analysis of these samples, the area value corresponding to each concentration was found.

3.6.1.2. Accuracy

Accuracy refers to the closeness of the analytical method to the true value or the accepted reference value. Accuracy must be ensured throughout the specified range. Generally, three different concentrations within the specified range are measured in at

least three samples each. The results obtained are evaluated by calculating the % yield and the relative standard deviation of each batch (ICH, 2005).

In this thesis study, a solution containing MEIS1 at 3 different concentrations (5 µg. mL^{-1}, 40 µg. mL^{-1}, 100 µg. mL^{-1}) was prepared to determine the accuracy. Each solution was analyzed 3 times.

3.6.1.3. Precision

Precision refers to the distribution among a set of measurements obtained from multiple analysis of the same sample under certain conditions. The parameters of repeatability, intermediate precision, and reproducibility play a role in the interpretation of precision (ICH, 2005).

The repeatability parameter specifies the precision under the same conditions within a short time interval. For the determination of reproducibility, the area measurement of the samples prepared from the same stock solution should be repeated (ICH, 2005).

In this study, the precision of the method was determined by making repeated measurements of the MEIS1 solution prepared with 3 different concentrations (5 µg. mL^{-1}, 40 µg. mL^{-1}, 100 µg. mL^{-1}) in the calibration range, 3 times on 3 different days.

3.6.1.4. Sensitivity

Sensitivity is the ability of the method used to detect the substance in the sample and determine its concentration. The sensitivity of the method is interpreted by calculating the limit of detection (LOD) and limit of quantitation (LOQ) (ICH, 2005).

LOD is expressed as the lowest concentration at which the signal of the standard substance is separated from the noise. Depending on the device used for the analysis, different methods are used to determine the LOD value. The LOD value is found by visual evaluation, signal-to-noise ratio and the obtained response and standard deviation of the slope (ICH, 2005).

Equation 3.1 in the ICH manual is used to calculate the LOD (ICH, 2005).

$$LOD = \frac{3.3\,\sigma}{S} \tag{3.1}$$

LOQ, on the other hand, is the lowest amount of standard substance in a sample that can be quantitatively detected with appropriate accuracy and precision.

Equation 3.2 in the ICH manual is used to calculate LOQ (ICH, 2005).

$$LOQ = \frac{10\,\sigma}{S} \tag{3.2}$$

Here, σ denotes the standard deviation of the y-axis intercept and m denotes the slope of the correlation equation.

3.6.2. Determining the amount of MEIS conjugated to MNs and MENs

The UPLC method was used to determine the amount of drug loaded on solid lipid nanoparticles, MNs, and MENs. For this purpose, 3K MWCO Amicon Ultra-0.5 Centrifugal Filter Unit was used to remove free MEIS that was not trapped in the lipid during the formulation study. 500 µL samples taken from the formulations were placed in centrifugal filters, centrifuged at 6000 rpm for 10 minutes to separate free MEIS. The amount of free MEIS in the separated supernatant was determined using UPLC. To find the amount of loaded MEIS, 500 µL of the formulations were taken, sonicated in acetonitrile: methanol (1:1 w:w) mixture and analyzed by UPLC method after centrifugation.

$$\%EE = \frac{AAF-AAS}{AAF} x\ 100 \quad (3.3)$$

Here, AAF is amount of active agent in the formulation and AAS is mount of active agent in the supernatant.

3.7. Determination of the Effects of Prepared Drug Systems on Cells

3.7.1. Cell culture studies

One investigated the effectiveness of the formulations prepared by cell culture studies on healthy and cancer cells. For this purpose, one used human umbilical vein endothelial cell (HUVEC) lines and female preneoplastic breast epithelial cell line (MCF-10A) as healthy cells, adenocarcinomic human alveolar basal epithelial cell (A549), human pancreas ductal adenocarcinoma (PANC-1), metastatic mammary adenocarcinoma (MDA-MB-231), and human breast adenocarcinoma (MCF-7) as cancer cells. One used the standard cell culture technique both in the production of the cells and in applying the formulations to the cells. For this, cells were cultured in DMEM containing 10% fetal bovine serum (FBS), 1% penicillin-streptomycin, and 1% L-glutamine. One carried out cell culture at 37°C in an atmosphere containing 5% CO_2 and 95% air. After the cells reached the rapid growth phase, they were treated with 2xTrypsin/EDTA solution and subcultured (Büyükköroğlu et al., 2016).

3.7.2. MTT test

The colorimetric 3-(4,5-dimethylthiazol-2-yl)-2,5-diphenyltetrazolium bromide (MTT) method was used for the quantitative determination of cell cytotoxicity. In cell culture studies, one used 96-well cell culture plates. After one suspended the cells in 10% FBS at a concentration of $2x10^4$ cells/mL, one transferred the cell suspension to each well of 96-well cell culture plates (100 µL). After a one-day growth period, to examine the cytotoxic effects on the second day, the cells in which formulations dispersed in distilled water were added to the cell suspensions at specific concentrations, and the control cells were incubated at 37°C in an atmosphere containing 5% CO_2 and 95% air for 24-48 hours. At the end of the determined incubation period, 20 µL (5 mg/mL) MTT dye was added to each well and incubated for another 4 hours at 37°C so that the MTT dye could be converted into formazan salt by living cells. At the end of this period, one removed MTT, added 200 µL DMSO to each well, and determined the color change spectrophotometrically at 570nm wavelength in a plate reader. The percentage of viable cells (%) in each well was calculated by comparing it with the control group (Büyükköroğlu et al., 2016).

3.8. Characterization of Nanostructures

The magnetoelastic core structure of the most popular room temperature MEN configuration is $CoFe_2O_4$, and the piezoelectric shell structure is $BaTiO_3$. Due to their structure, MENs have specific magnetic properties. For example, the coercivity of MENs at room temperature is around 100 Oe (Stewart et al., 2018). This value is higher in ferromagnetic structures. Even magnetic saturation values are approximately ≤10 emu/g. This value is much higher in structures with high magnetic moments, such as iron oxide. Magnetic characterization is crucial, especially in understanding how MEN behave in the applied magnetic field (Stewart et al., 2018). For this reason, one made the characterizations of the basic properties of the synthesized structures in this study.

These characterizations;

- Analysis of particle sizes and charges of nanostructures,
- Morphological analysis of nanostructures such as particle size and coating,
- Analysis of magnetic properties of nanostructures,
- Chemical analysis of nanostructures,
- Analysis of crystal structures of nanostructures.

3.8.1. Analysis of particle sizes and charges of nanostructures

One used the Zetasizer device in the Anadolu University Faculty of Pharmacy Pharmaceutical Technology Laboratory to analyze the prepared nanostructures' size and zeta potential. Distilled water with pH 7.4 and 50 µS conductivity passed through a 0.22 µm filter was used for the measurements. 5 mg of each synthesized nanoparticle was weighed and dispersed in 2 mL distilled water (pH 7.4, 50 µSm). ZetaSizer measurements were made by taking 50 µL of this dispersion and mixing it with 950 mL of distilled water. One took all measurements using back-scattering geometry (173^{o}). One used "Auto Run" for measurements, and the software measured an average of 10 to 15 Zeta Runs. All measurements were made at 25°C using a "Clear Disposable Zeta Cell." For lipid-coated formulations, 50 µL samples were taken and measurements were carried out in the same way.

Afterward, one analyzed the zeta potentials of the structures synthesized using ZetaSizer. One calculated this potential with the Helmholtz-Smoluchowski equation utilizing the device's software.

3.8.2. Morphological analysis of nanostructures

One received JEOL 1220 JEM brand Transmission Electron Microscope (TEM) service support for the morphological analysis of the synthesized nanostructures from Eskişehir Osmangazi University Central Research Laboratory Application and Research Center (ESOGÜ-ARUM).

TEM works with the principle of passing high-energy electrons over a sample and detects and images the particles and rays arising due to the interaction of these electrons with the atoms in the sample. Thanks to TEM, morphological analyses can be made up to very high magnifications.

Due to their structure, one examined the nanostructures synthesized in this study under 100kV. Since one has observed that they burn out when higher kV is reached, one determined the voltage of 100kV as ideal, and one made images accordingly.

3.8.3. Analysis of magnetic properties of nanostructures

One received Dexing Magnet VSM 550 brand Vibrating Sample Magnetometer (VSM) service from Dokuz Eylül University Electronic Materials Production and Application Center (DEU-EMUM) for the magnetic characterization of the synthesized nanostructures. One analyzed magnetic properties such as hysteresis plots,

magnetization curves, magnetic moments, coercivities, and residual magnetization of nanostructures using VSM.

The basic working principle of VSM is based on Faraday's law. Accordingly, when a magnetic material vibrates, there is a flux change. With this change, an electromagnetic force (EMF) is formed. The magnetic field range of the VSM used in this thesis is 0 – 3.5 T, the magnetic moment range is 10-2 – 300 emu, and the application temperature range is -196 – 900°C.

Since the nanostructures synthesized in this study were pulverized, a minimum sample of 300 mg was sufficient for VSM analysis.

3.8.4. Chemical Analysis of Nanostructures

One received Thermo Scientific K-Alpha model X-Ray Photoelectron Spectroscopy (XPS) service support from Dokuz Eylül University Electronic Materials Production and Application Center (DEU-EMUM) for the chemical characterization of the synthesized nanostructures. Using XPS, one analyzed whether the nanostructures produced have the desired chemical content.

XPS is a measurement of the energies of electrons ejected from the surface of a material by X-rays. With XPS, one can make only chemical analyzes of the surface layers. Because the distances that electrons emitted by X-rays can travel without losing energy too much are very short. This limitation provides an analysis opportunity from the surface to a depth of approximately 5-10 nanometers.

The XPS utilized in this thesis has a 180° dual focus hemisphere analyzer, 128 channel detector, Al Kα microfocus monochromator, 30-400 μm spot size with 5 μm pitch, dual beam source, ultra-low energy electron beam and 100-4000 eV. It has an ion gun with an energy range.

The synthesized nanostructures were prepared with a maximum sample area of 60 × 60 mm2 and a maximum sample thickness of 20 mm.

3.8.5. Analysis of Crystal Structures of Nanostructures

One received Thermo Scientific ARL X'TRA branded X-Ray Diffractometer (XRD) service support from Dokuz Eylül University Electronic Materials Production and Application Center (DEU-EMUM) for the chemical characterization of the synthesized nanostructures. Using XRD, the nanostructures were analyzed to determine whether they were in the desired crystal structure.

In XRD analysis, the X-rays sent to the material to be examined diffracted depending on the atomic arrangement specific to the crystal phase. These diffraction profiles quantitatively describe a particular crystal structure. One can perform XRD analysis even with samples at a minimal amount.

In thesis study, the XRD has Cu-Kα, Ni-filtered X-ray source, a source voltage of 15 – 60 kV, a source current of 5 – 60 mA, a scanning range of 0 – 89°, an average scanning speed of 0.1°, and an angular resolution of <0.04° FWHM.

Since the nanostructures synthesized in this study were pulverized, a minimum sample of 150 mg was sufficient for XRD analysis.

4. FINDINGS AND DISCUSSION

Targeted drug delivery systems are at the forefront of new-generation treatment methods. Because the spread of active substances prepared in a synthetic, semi-synthetic way to be used in treating many diseases into the body circulation may cause undesirable side effects. Studies on targetable drug systems, one of the systems studied, have increased to prevent this (Vasir & Labhasetwar, 2005). One has developed and still developing drug targeting and delivery systems in this context (Bañobre-López et al., 2013; Beik et al., 2016; Iyer et al., 2006; Jurgons et al., 2006; Khan et al., 2015; Krpetić et al., 2012; Rajabi et al., 2016; Rodzinski et al., 2016; Stimphil et al., 2017).

This study focused on metastatic bone cancer. Considering the anatomical structure of the bone and the diversity of cancer types developing in the bone, the lack of effective bone-specific drug therapy is striking (Angel García Sáenz et al., 2007; Mundy, 2002; Raymaekers et al., 2015). One predicted that ligand-mediated active targeting systems would not be impactful for bone cancer, and physical targeting methods were preferred to overcome this deficiency. MEN with magnetic properties were preferred as suitable physical targeting parts (Guduru et al., 2013; Rodzinski et al., 2016; Stewart et al., 2018; Stimphil et al., 2017; Yue et al., 2012).

Although the history of ME materials is old, their use in the health field is relatively new (Guduru et al., 2013; Rodzinski et al., 2016; Stewart et al., 2018; Stimphil et al., 2017; Yue et al., 2012). ME materials are used and are trying to be used in many areas thanks to their ability to have two ferroic properties simultaneously. In recent years, these materials have shown great promise for drug targeting and nano electroporation in cancer therapy. Because when ME structures are injected into the body, external magnetic field application provides orientation and retention to the desired region and creates an electrical field in magnetic field exposure, which opens the way for nano electroporation at the cellular level (Guduru et al., 2013; Rodzinski et al., 2016; Stewart et al., 2018; Stimphil et al., 2017; Yue et al., 2012).

ME materials are basically divided into single and double phases. Single-phase MENs do not exhibit high intensity ME effects but have low ME coefficients. This may be insufficient to form pores in cancer cells' membranes and disrupt their membrane structures. Therefore, dual-phase ME systems with high ME coefficients are preferred for targeting and treatment. The core parts of dual-phase MENs are piezomagnetic or magnetoelastic. In other words, they can show the piezo effect under the influence of a

magnetic field. The shell parts are also piezoelectric. That is, they can be electrically polarized under a piezo effect. In this way, under the magnetic field, the core parts of the dual-phase MENs can be oriented while creating an electrical field by triggering the shell parts with a piezo effect (Stimphil et al., 2017).

4.1. Standardization of MN Synthesis

Although there is more than one method in the literature for the synthesis phase of MNs, one has used the standard hydrothermal synthesis method due to its easy applicability and low cost (Stimphil et al., 2017). In the hydrothermal synthesis method for synthesizing dual phase magnetoelectric structures, one uses UPW in synthesizing MNs. During synthesizing such nanostructures by chemical processes, many parameters such as pH, temperature, and time can affect nanostructures' size, zeta potential, and chemical and physical properties (Schäf et al., 2004). In the hydrothermal synthesis methods in the literature, the temperature parameter has already been determined (Etier et al., 2012; Stimphil et al., 2017). However, the pH parameter, which is very effective in chemical synthesis processes, has not been determined and not specified. Considering this situation, one saw that the pH parameter should also be set to a certain standard for the hydrothermal synthesis of MENs, and it was carried out in this study.

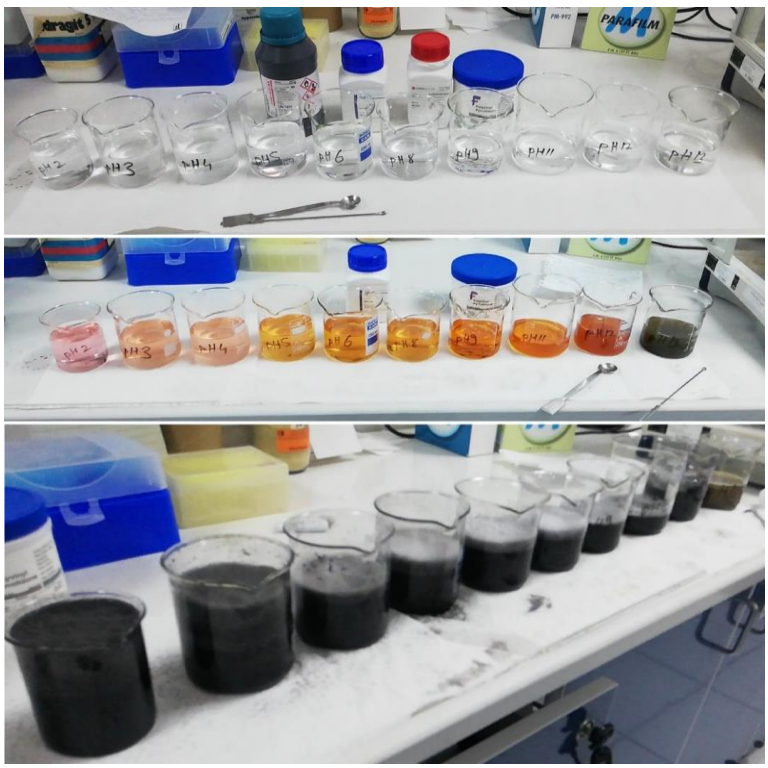

Image 4.1. *Magnetic nanoparticles synthesized at different pHs.*

All variable conditions were kept constant at this stage, and only the pH parameter was changed. One used UPWs with different pH (2-13 pH) and synthesized MNs at different pH. Image 4.1 shows all of them except for two ones. Since one previously synthesized MNs using UPWs of pH 7 and 10, they are not included in image 4.1.

4.1.1. Magnetization test

One carried out the magnetization tests of the MNs obtained at each pH with four Neodymium magnets with a working temperature of 80°C (Curie Temperature) and an intrinsic coercivity of approximately kOe > ~10.5. As a result of this test, one observed that the nanostructures synthesized in the pH 2-5 and pH 12-13 ranges could not be effectively magnetized. As a result of the magnetization tests, one observed that the nanoparticles synthesized in the pH 6–11 range were efficiently magnetized (Table 4.1).

Table 4.1. *Magnetizations of MNs synthesized at each pH.*

Values of pH	2	3	4	5	6	7	8	9	10	11	12	13
Magnetization	-	-	-	-	+	+	+	+	+	+	-	-

4.1.2. Particle size, polydispersity index and zeta potential

Particle size is of critical importance in drug systems. It affects many factors that can affect the efficacy of drug systems, such as cellular uptake, metabolism or biodegradation, and physical stability (Ekambaram et al., 2012). Although the particle size varies for different medical purposes, one has decided that the particle size that can be applied generally is between 1-1000nm (Wagner et al., 2006; http-5).

In addition, it is known that the spaces (100-780nm) between endothelial cells differ according to different cancer types, and this situation has been reported in many studies (Hashizume et al., 2000; Hobbs et al., 1998). In this context, when we consider the particle size, it is seen that drug systems with different sizes should be designed even for the treatments of different cancer types.

During the synthesis of nanostructures, many parameters such as pH, temperature, mixing speed and time, and amount of catalyst affect these structures' particle size and distribution (Ekambaram et al., 2012). For this reason, one should examine particle sizes and distributions of nanostructures synthesized according to each variable.

Like particle size, the polydispersity index (PDI) is an essential parameter for formulations. It affects the aggregation of nanostructures at the targeted site; therefore, it is crucial to characterize synthesized drug formulations (Danaei et al., 2018).

PDI is a parameter ranging from 0 to 1 that allows the size distribution and range of the synthesized materials to be expressed as a numerical value after dispersing these materials in the liquid. The closer the PDI value is to 0, the more homogeneous the particle size distribution is assumed (Danaei et al., 2018). As a result of studies conducted with different materials in the literature, it has been noticed that there are material-specific PDI values (Badran, n.d.; Clarke, 2013). One has observed that lipid-based structures designed especially as drug delivery systems can have perfect homogeneity when PDI values are 0.3 and below (Badran, n.d.; Danaei et al., 2018).

In addition to particle size and polydispersity index, Zeta potential is a critical parameter for all drug formulations. It allows the interpretation of many basic mechanisms, such as the aggregation of the synthesized structures, their dispersity stability, and their ability to form weak bonds (Clogston & Patri, 2011; Lowry et al., 2016).

Fundamentally, one expresses the zeta potential as a numerical value for the motion of nanostructures under an electrical field exposure, having a net charge and being suspended in the liquid. Two primary regions enable the formation of zeta potential in nanostructures. One of these regions is the inner layer called the “Stern” layer. In this layer, the ions are firmly bound. The other layer is the outer layer, called the “Diffuse” layer. This layer also consists of more loosely related ions. These two layers together form the electrical double layer. One can also consider the zeta potential as the numerical value of this electrical double layer (Clogston & Patri, 2011; Lowry et al., 2016). However, fundamentally, it is clearly expressed as the electrostatic potential at the boundary called the “slipping plane.”

The zeta potential is affected by many chemical parameters. However, pH directly affects it since it depends on H+ ions. For example, the zeta potential is generally positive for acidic pH values and negative for basic pH values. This situation shows that the zeta potential is directly affected by pH (Berg et al., 2009; Chang et al., 2015).

One has also established zeta potential to certain standards with the studies. According to the standards, one defines nanostructures with a zeta potential between -10 mV and +10 mV as neutral structures (Clogston & Patri, 2011). One stated that

nanostructures with zeta potentials of -30 mV ≥ and +30 mV ≤ zeta are also strong anions and cations (Clogston & Patri, 2011). Due to their anionic and cationic properties, they show strong stability against aggregation (Lowry et al., 2016).

Table 4.2 shows the particle sizes, PDIs, and zeta potentials of MNs that can be magnetized in the magnetization test. As it can be understood from the obtained data, synthesis steps have been tried to be examined in many ways. In this context, one has concluded that the ideal synthesis for MN structures should be done using UPW having pH 10. As a zeta potential, it seems to be a perfect structure in terms of being resistant to aggregation formation, having a homogeneous particle size, and having a particle size of approximately ~100 nm.

Table 4.2. *Particle sizes, PDI and Zeta potentials of MNs synthesized at different pHs.*

Sample	Particle size (Nm)	PDI	Zeta potential (mV)
Synthesized with pH 6	134.7 ± 24.25	0.235 ± 0.072	-3.69
Synthesized with pH 7	97.31 ± 27.83	0.316 ± 0.088	-0.23
Synthesized with pH 8	104.6 ± 28.7	0.353 ± 0.095	-2.87
Synthesized with pH 9	106.6 ± 26.5	0.283 ± 0.081	-8.40
Synthesized with pH 10	101.42 ± 36.9	0.238 ± 0.075	-42.26
Synthesized with pH 11	99.6 ± 26.75	0.269 ± 0.078	-5.71

In general, formulations prepared with solid lipids have negative zeta potential because lipids have a negative surface charge (Büyükköroğlu et al., 2015). Since MN synthesized at pH 10 with a high negative zeta potential (-42.26 mV) is thought to be difficult to coat with a lipid with negative zeta potential, due to the electrical repulsion between them, it has a neutral and well magnetizable pH in lipid-coated MN formulations. Particles synthesized with 7 were used.

4.2. Synthesis of MENs

After the standardization study of MNs, MENs were synthesized from MNs synthesized with pH 10. One used the "Standard Hydrothermal Synthesis" method mentioned in the Materials and Methods section for this. Different chemical synthesis methods are available for the synthesis of MENs (Etier et al., 2012; Guduru et al., 2013; Stewart et al., 2018). However, as mentioned in the standardization section, one chose this chemical synthesis method because of its low-cost and easy application in the laboratory environment. The standard hydrothermal synthesis method of MENs is

illustrated step-by-step in Image 4.2 and 4.3. In Image 4.2, one added only UPW to the beakers in step 1. In step 2, one added cobalt nitrate hexahydrate to all three beakers and iron (III) nitrate nonahydrate to only the rightmost beaker. The difference can be easily seen from the color change. In step 3, one added polyvinylpyrrolidone and sodium borohydride to each beaker to reduce the unwanted aggregation of nanostructures and initiate the reaction. Afterward, one continued the reaction at 120°C for about 12 hours. In step 4, one observed the formation of ferroic liquid after 12 hours. In step 5, one dried the samples at 80°C. One exposed the dried samples to high temperature in the muffle furnace for purification and calcination in step 6 and obtained the powdered $CoFe_2O_4$ nanostructures in the 7th step.

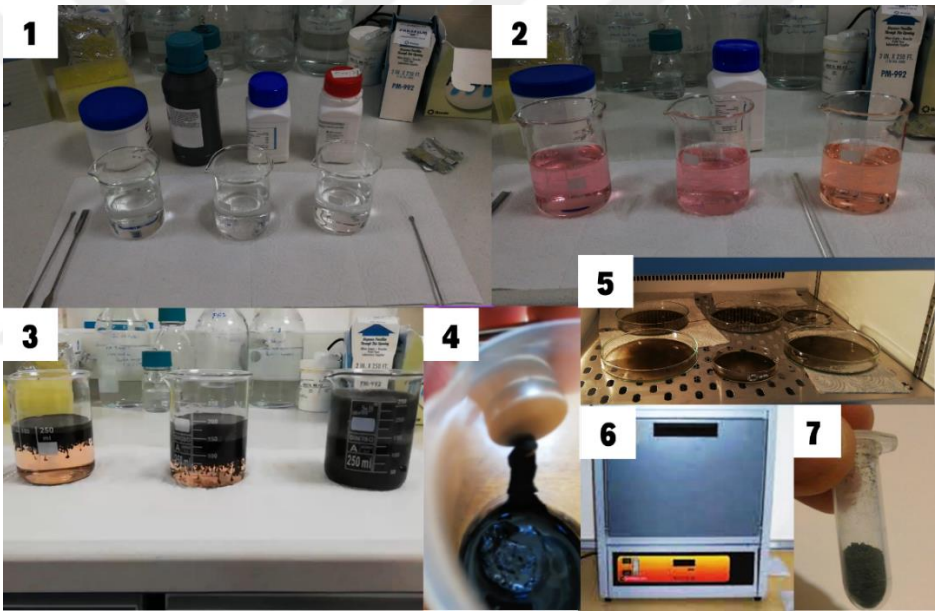

Image 4.2. *Synthesis of MNs by hydrothermal method*

In this way, after synthesizing the $CoFe_2O_4$ nanostructures, the magnetoelastic core part, steps in Image 4.3 were started. In Image 4.3, one added UPW to one beaker in step 2 and ethanol to the other in step 3. In the 4th step, one added barium carbonate and citric acid to the beaker containing UPW and mixed citric acid and titanium (IV) isopropoxide to the beaker containing ethanol, allowing them to dissolve completely. In the 5th step, one added ethanol to the UPW solution and mixed it with a magnetic stirrer. In the 6th step, one added $CoFe_2O_4$ nanostructures to this mixture and combined them with a sonicator in the 7th step. After approximately 2 hours of sonication, one obtained a solution of $CoFe_2O_4$-$BaTiO_3$ nanostructures with a milky opaque structure.

Afterward, one acquired powder magneto-electric $CoFe_2O_4$-$BaTiO_3$ nanostructures by applying the same drying and purification process of $CoFe_2O_4$ powder nanostructures.

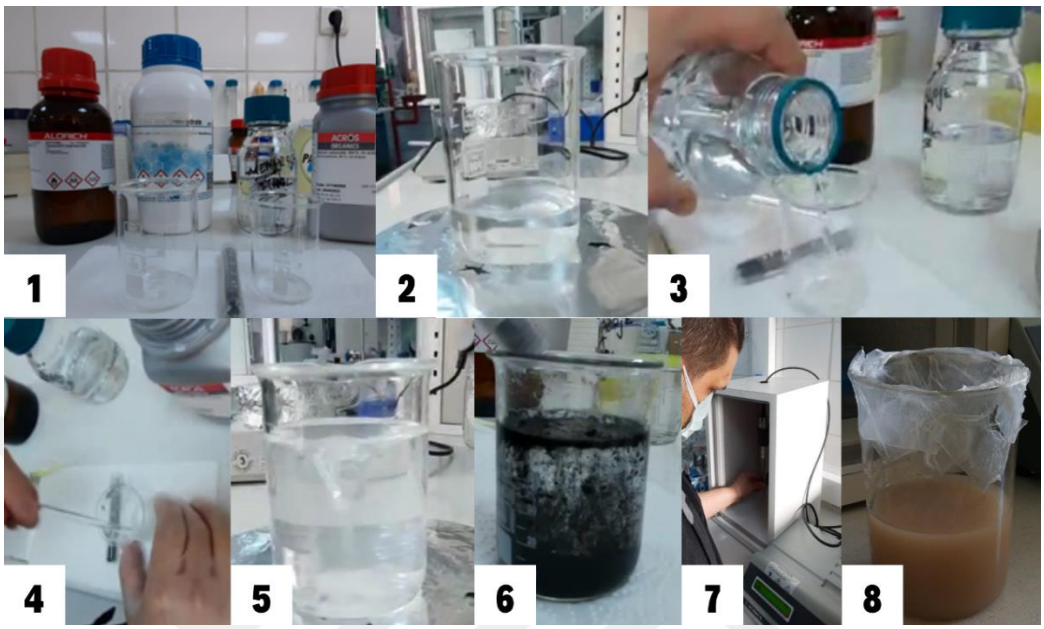

Image 4.3. *Synthesis of MENs by hydrothermal method*

4.3. Characterization of MENs and MNs

Some properties of synthesized MENs and MNs need to be characterized. Since MENs and MNs are magnetizable particles, one should describe their magnetization or magnetic properties in detail by performing their magnetic characterization (Tumanski, 2016). In addition, it is necessary to analyze the particle sizes of both structures and whether the MNs are covered with piezoelectric shell parts to form MEN structures. In addition to all these, it is crucial to perform chemical analyzes.

4.3.1. Magnetic characterization

One characterized the synthesized nanostructures by purchasing VSM from DEU-EMUM magnetically. The hysteresis graphs of MENs and MNs were determined by performing VSM analyses at 300 Kelvin temperature under 32000 Oe magnetic field intensity. Image 4.4 represents the hysteresis plot of MNs, and Image 4.5 illustrates the hysteresis plot of MENs.

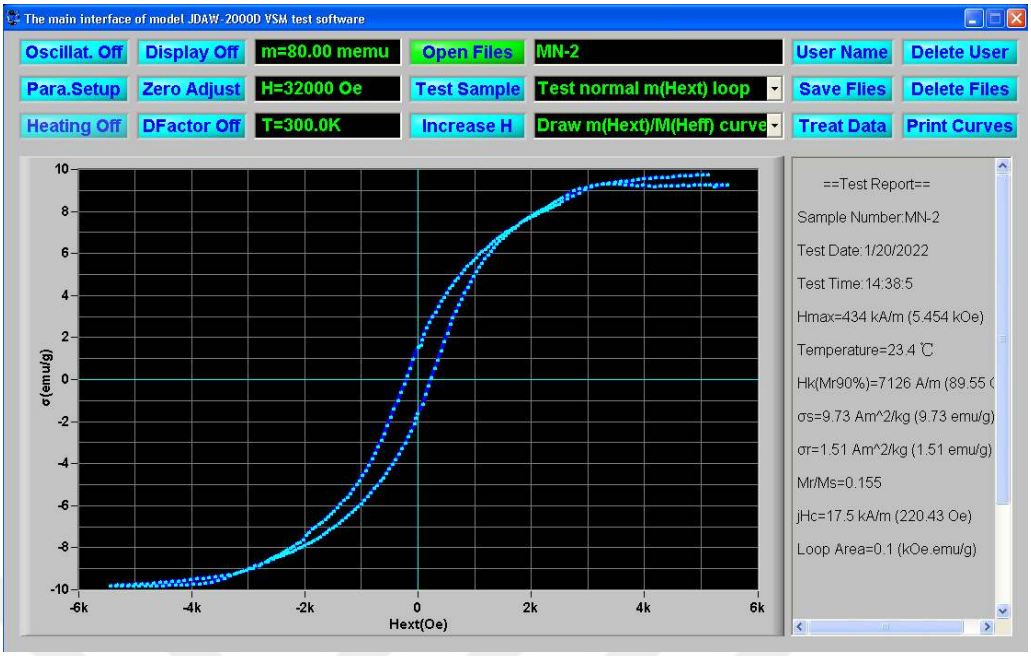

Image 4.4. *Hysteresis plot of MNs obtained with VSM.*

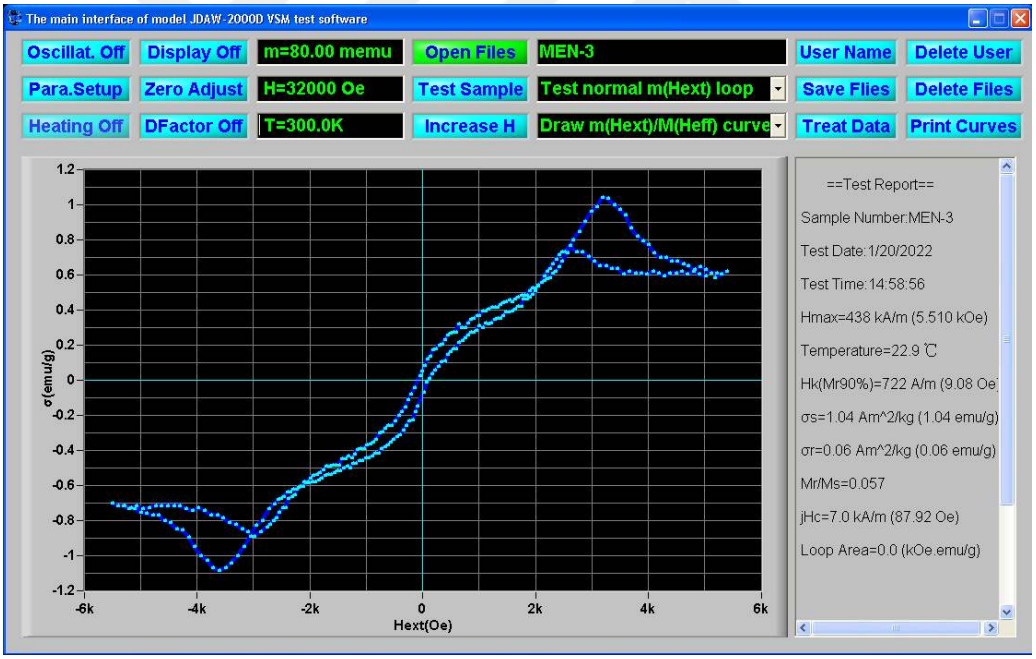

Image 4.5. *Hysteresis plot of MENs obtained with VSM.*

VSM analyzes show that both materials can be magnetized. However, when examining Image 4.4 and 4.5, one observed that there were some differences in the magnetic characterizations of the two nanostructures. This situation is expected because the core parts of MEN structures are magnetoelastic. In other words, they can show ferromagnetic properties. For this reason, they are easier to become magnetized under a magnetic field. Shell parts are in a piezoelectric or electroelastic structure. They do not

have magnetic properties. They create an electrical field by being elastically triggered by the core part under a magnetic field. For this reason, one expected that the magnetic properties of MENs, which are formed by the conjugation of the core and shell parts, differ from the magnetic properties of the core part.

When examining the differences in magnetic properties between the two nanostructures in detail, the differences in coercive excitation or field draw attention. Coercive excitation, an essential feature for magnetic structures, refers to the magnitude of the magnetic field that must be applied in the opposite direction to bring the magnetized material back to zero magnetization value by being exposed to the magnetic field (Tumanski, 2016). According to the VSM results, the coercive excitation (jHc) data differed between MENs and MNs (Image 4.4, 4.5). The coercive excitation of MNs is 220.43 Oe (Image 4.4), while that of MENs is 87.92 Oe (Image 4.5). As can be seen from these results, the magnetic field that needs to be applied in the opposite direction to reset the magnetization of MENs is relatively low. This shows that MENs can exhibit magnetic behavior like paramagnetic substances.

Another feature expressed in the hysteresis graph is the σs parameter, which shows the value at which the magnetic flux density reaches saturation. Each magnetic material has its unique saturation magnetic flux density value, or in other words, saturation magnetization value (Tumanski, 2016). In this study, one can clearly see that both nanostructures have different saturation magnetic flux densities. According to the VSM analysis results, while σs for MNs is 9.53 emu/g (Image 4.4), this value is 1.04 emu/g for MENs (Image 4.5). Despite the difference in saturation magnetic flux densities of these materials, one detected no significant difference in the maximum magnetic field intensities, which is another magnetic property. The maximum magnetic field strength expresses the magnetic field strength that must be applied to reach the saturation magnetization value (Tumanski, 2016). There was no significant difference between the maximum magnetic field strength required for MNs and MENs to reach magnetic saturation. The H_{max} of MNs is 5,454 kOe (Image 4.4), while the H_{max} of MENs is 5,510 kOe (Image 4.5). This result means that they both need equal magnetic strength to reach saturation values.

In addition to the saturation magnetic flux density, the σ_r parameter, called residual magnetization or retentivity, is one of the critical magnetic properties of materials. The material can already have a residual magnetic moment when the applied

magnetic field value is zero in ferromagnetic materials. This magnetization value, existing even in a zero magnetic field, is called residual magnetization (Tumanski, 2016). When examining the hysteresis graphs in the magnetic analyses, one sees that both nanostructures have different residual magnetization values. While σ_r is 1.51 emu/g for MNs (Image 4.4), for MENs, it is a very low value (0.06 emu/g) (Image 4.5).

An important magnetic property that can be obtained by the ratio of the residual magnetization value to the saturation magnetization value ($\sigma_r/\ \sigma_s$) in magnetic materials is the residual ratio. The residual ratio is a numerical indication of permanent magnetism and is between 0 and 1 (Tumanski, 2016). There was also a significant difference in the residual ratio (M_r/M_s) results according to VSM analysis. While the residual ratio value of MNs was 0.155 (Image 4.4), one determined the residual ratio of MENs as 0.057 (Image 4.5). According to these results, one sees that the MENs are slightly closer to 0. This result means that the permanent magnetism of MENs is low. This situation shows that when one removes magnetic field exposure, they can have the potential to move away more quickly than materials with high permanent magnetism.

4.3.2. Morphological characterization

As mentioned in the previous sections, particle size is the most critical parameter of drug systems. Particle size can affect the physical and chemical properties of drug delivery systems and many cellular mechanisms (Ekambaram et al., 2012). For this reason, one has determined certain ideal size limits for drug systems. Limits have even been found to differ according to different types of cancer (Hashizume et al., 2000; Hobbs et al., 1998; Wagner et al., 2006). Therefore, it is crucial to carry out size analyzes of drug systems to be developed for cancer treatments. In this context, after magnetic analysis of the synthesized MNs and MENs, TEM service was obtained from ESOGÜ-ARUM to analyze their size in detailed and confirm that biphasic MEN structures were correctly synthesized by covering core MNs with a piezoelectric shell.

In TEM analysis, one performed imaging with a voltage of 100 kV. One observed that the samples burned as one reached higher voltage values. For this reason, imaging was performed at different magnification values by applying a voltage of 100 kV (Image 4.6-4.9).

The TEM image of MNs is shown in Image 4.6. According to this image, one can see that the MNs are of the desired size when compared to the 50 nm scale. However, compared to the ZetaSizer analyses mentioned in the previous section for size analysis,

one sees that the MNs in the TEM images are quite small. The main reason behind this is the use of the "Dynamic Light Scattering (DLS)" mechanism in ZetaSizer size analysis.

In this mechanism, the samples suspended in the prepared measuring liquid are exposed to a monochromatic light source. The light source is scattered from the suspended particles and collected by the detectors after moving through the liquid. At this stage, the particles in the liquid are in Brownian motion because they are not in a static state. Due to this movement, the distances and scattering intensities of the particles reaching the detector by scattering from the suspended particles vary depending on time. In this case, it becomes difficult to physically include the diffusion coefficients of the suspended particles in the analysis because the interaction between particles and the particle anisotropy changes the diffusion coefficient (Hassan et al., 2015). Therefore, specific physical models are used to reduce or removed the effect of the diffusion coefficient. Due to these disadvantages, DLS is a low-resolution technique for particle size analysis. However, it is a beneficial technique in analyzing the presence or absence of agglomeration, as it can perform particle size analysis depending on the light intensity (Hassan et al., 2015).

On the other hand, electron microscopes, as the name suggests, allow imaging by using electrons as a source. TEM systems physically use the wave-particle duality of electrons. As a working principle, the electron beam, which is detached from the source by thermal energy or electrostatic field strength in a vacuum environment, is accelerated and directed to the sample to be imaged with the help of electromagnetic lenses. Then, these electron beams targeted at the thin sample are passed over it. Afterward, electrons whose energies have changed are magnified again with the help of lenses, and images are formed using electron detectors such as fluorescent (Williams & Carter, 2009).

In short, electron microscopes make use of the de Broglie wavelengths of electrons, which are much smaller than the wavelengths of the sources used in light microscopes. Due to the wavelength differences of the sources used in these imaging mechanisms, TEMs can offer imaging with atomic resolution. Therefore, there may be differences in particle sizes between ZetaSizer measurements and TEM analyzes.

In this study, TEM images of MNs in Image 4.6 were taken at 200000x magnification. They are seen as aggregated with each other in the middle part of the

image. One has determined that even in the case of aggregation of MNs, they have a size of around 100 nm. The size is ideal for the drug system designed in this study.

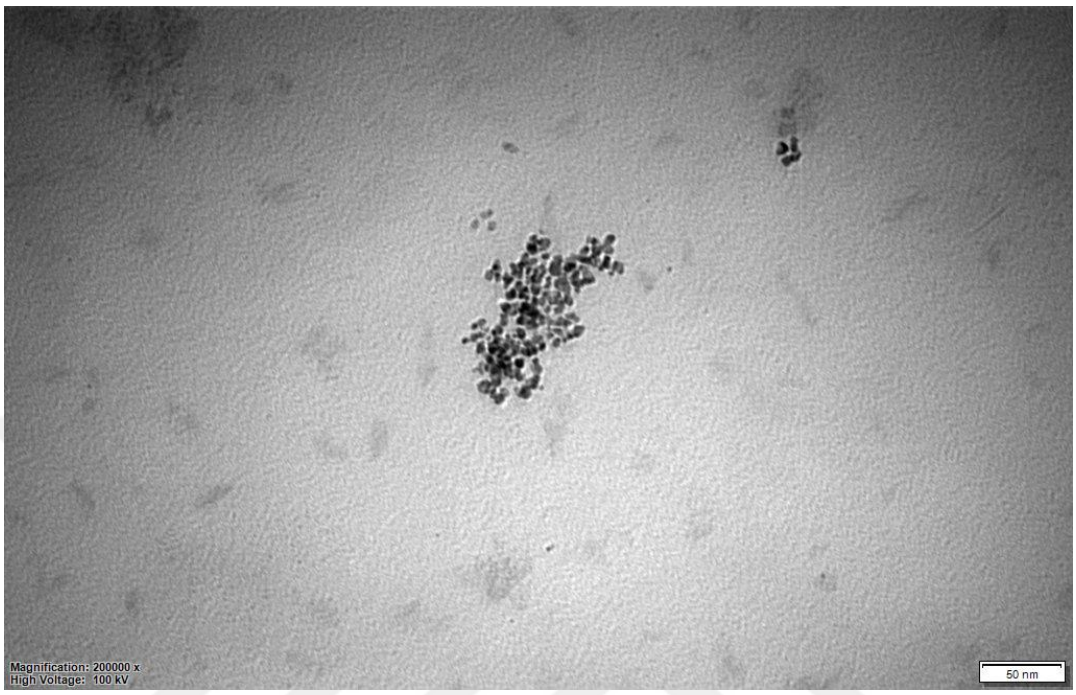

Image 4.6. *TEM image of MNs (200000x)*

TEM images of MENs from synthesized nanostructures under different magnifications are also shown in Image 4.7-4.9. In Image 4.7, displayed using 100 kV and 10000x magnification, the structures circled in yellow represent MENs. One can see that the dark black core parts in the middle of these structures are covered with crustal parts that appear as grayish clouds around them. The largest MEN structure is less than one μm in size. At this stage, it is seen that a piezoelectric shell covers the probably aggregated MNs.

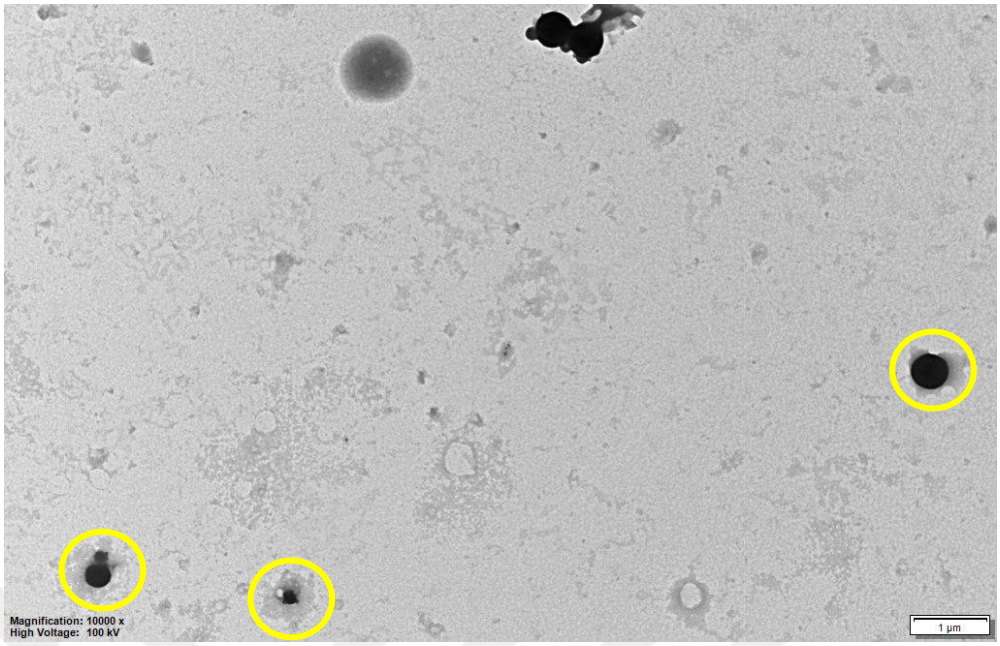

Image 4.7. *TEM image of MENs (10000x)*

In Image 4.8, with 100000 x magnification, one focused on the image of the largest MEN on the far right in Image 4.7. The MEN structure can be seen more clearly in this image. The core structure seen in dark black indicates the magneto-elastic structure, and the gray shell structure surrounding it also expresses the piezoelectric structure. These images show that piezoelectric shells cover MNs.

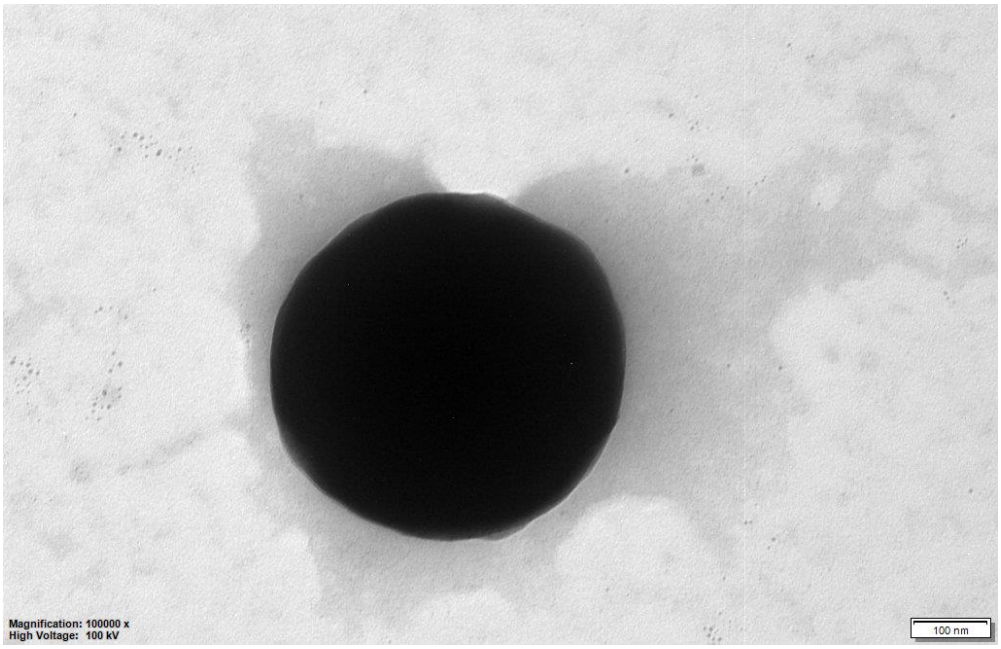

Image 4.8. *TEM image of a MEN structure (100000x)*

Image 4.9 shows TEM images of multiple aggregated MEN structures. From this point of view, one can deduce that the core parts are covered with shell structures even in the aggregated state. Especially when examining the circled structures on the lower right in the TEM image, one can clearly see that gray shells cover the dark black core structures. One has even determined that the particle sizes of these structures are 39 nm and 28.33 nm. In fact, with this TEM image, one can see that even MNs in aggregated small structures are coated independently of aggregation.

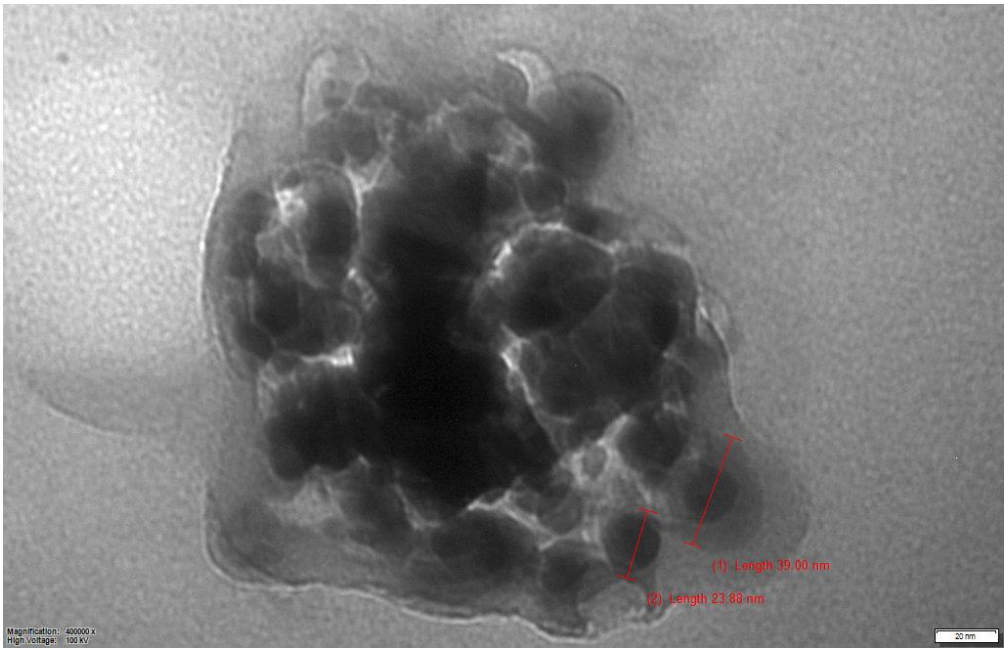

Image 4.9. *TEM image of aggregated MENs (400000x)*

4.3.3. Chemical characterization

As mentioned in the previous sections, the MENs synthesized in this study have a dual-phase ME structure. For this reason, one carried out the synthesis step as the synthesis of two different structures. The core part, MNs, is in the structure of cobalt iron oxide. Therefore, it consists of the elements: cobalt, iron, and oxygen. MENs, on the other hand, are biphasic multiferroic structures obtained by coating barium titanium oxide on cobalt iron oxide. Therefore, the elemental composition of the shell is composed of barium, titanium, and oxygen elements. Fundamentally, one expects these elements to be seen in chemical analysis. When examining the XPS analyses of this study's synthesized structures, one determined that the analysis results were as expected.

XPS service was obtained from DEU-EMUM to characterize samples chemically. One made this analysis using an Al K Alpha source with 400 µm spot size, 30 eV analysis mode, and approximately 3 minutes of scanning with energy steps of 0.1 eV.

Images 4.10 and 4.11 represent the chemical analysis of MNs. As a result of this analysis, one expects that iron, cobalt, and oxygen, which form the elemental composition of MNs, will be seen. In this context, when examining XPS results, one can see that iron, cobalt, and oxygen elements are present in the chemical structures of MNs. This result shows that the core structures were synthesized as desired.

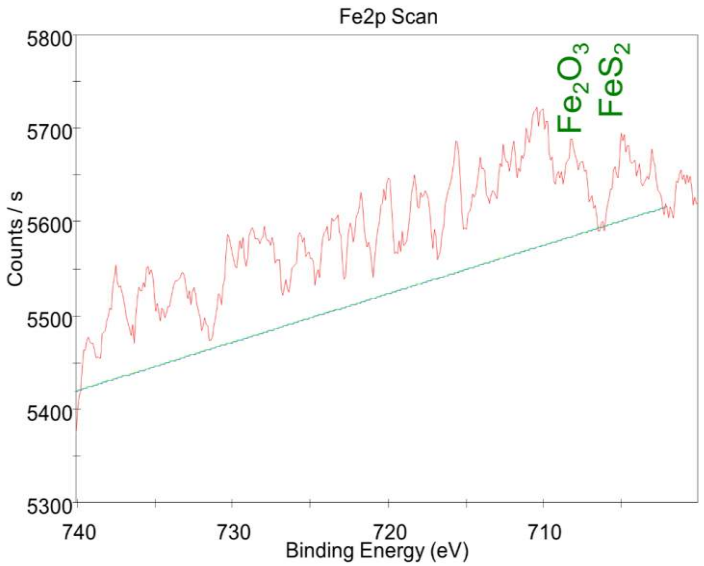

Image 4.10. *XPS analysis of element iron in MNs*

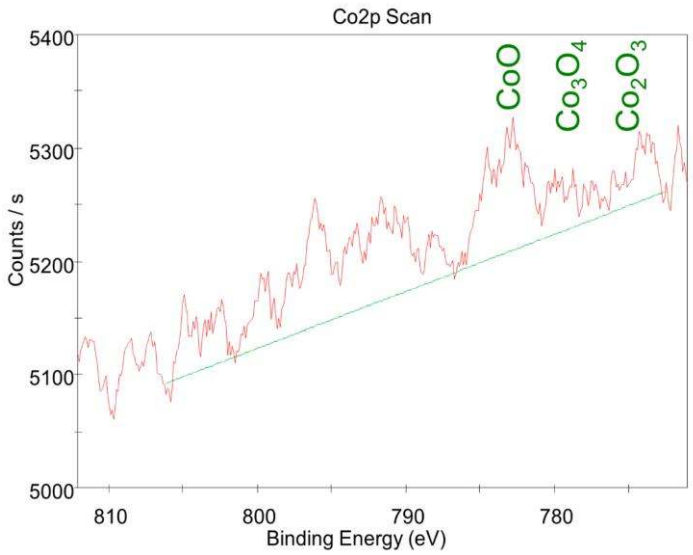

Image 4.11. *XPS analysis of element cobalt in MNs*

In the chemical analysis of MENs, one expects barium and titanium elements in the shell to be seen in addition to the other elements. Images 4.12-4.15 show the XPS analysis results of these elements that make up the MENs. According to these results, one can see that there are iron, cobalt, barium, and titanium elements in the chemical structures of the particles.

Results in Images 4.12 and 4.13 confirmed the chemical analysis of the core structure consisting of iron and cobalt coated in the MENs. Results in Images 4.14 and 4.15 confirmed the presence of these elements in the shell structure consisting of barium and titanium. These results show that the core+shell structures were synthesized with the desired chemical content.

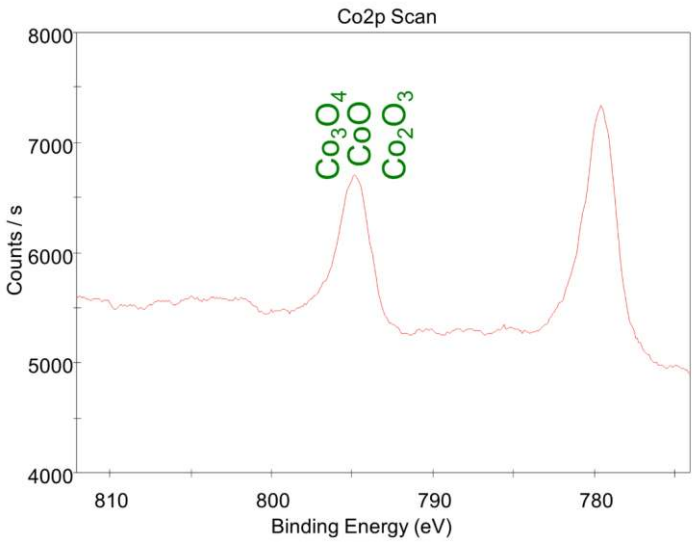

Image 4.12. *XPS analysis of element cobalt in MENs*

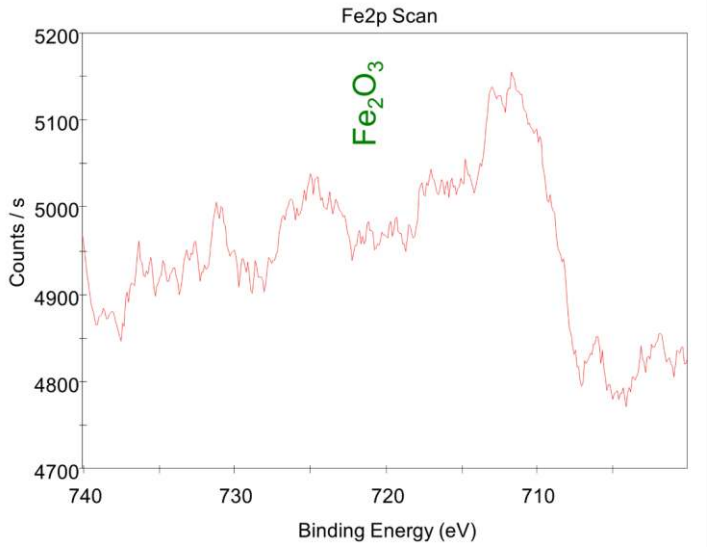

Image 4.13. *XPS analysis of element iron in MENs*

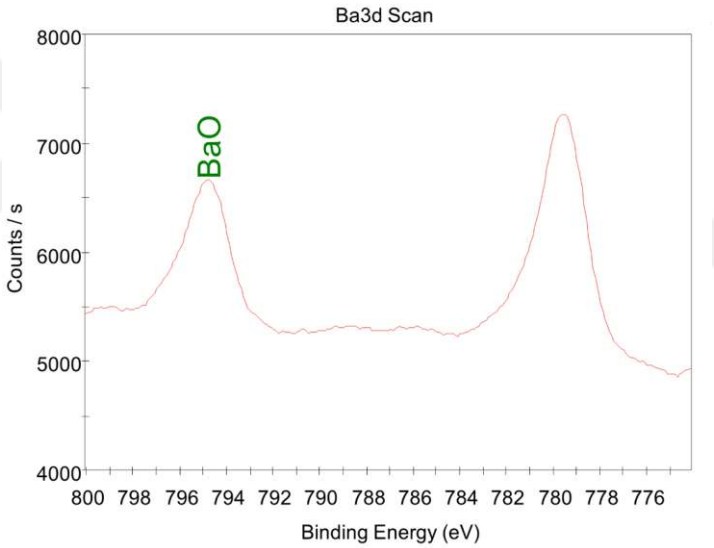

Image 4.14. *XPS analysis of element barium in MENs*

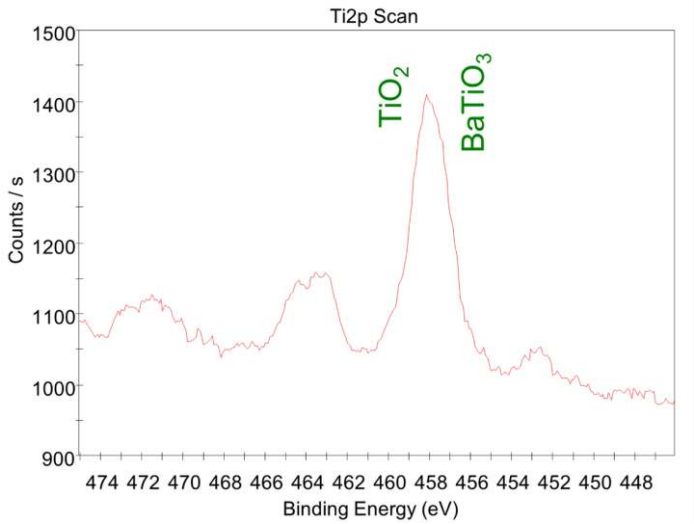

Image 4.15. *XPS analysis of element titanium in MENs*

4.3.4. Crystal structure characterization

One has already determined approximately the crystal structures of $CoFe_2O_4$ core and $CoFe_2O_4$-$BaTiO_3$ nanostructures in the literature (Shahzad et al., 2021; P. Wang et al., 2020). In the literature, one has observed that $CoFe_2O_4$ core structures can have (111), (220), (311), (222), (400), (422), (511), (440), and (533) crystal plane structures. In XRD analysis, the (311) peak is the primary characteristic peak of $CoFe_2O_4$ (Shahzad et al., 2021; P. Wang et al., 2020).

Considering the studies in the literature on $BaTiO_3$ shell structures, one determined that they have (100), (110), (311), (111), (200), and (211) peaks in XRD analysis (Shahzad et al., 2021; P. Wang et al., 2020).

In $CoFe_2O_4$-$BaTiO_3$ MEN structures, on the other hand, peaks have been obtained in the literature, which may vary depending on the ratios of these two core and shell structures, but fundamentally have crystal peaks of these structures (Shahzad et al., 2021; P. Wang et al., 2020).

For the analysis in this study, one obtained an XRD service from DEU-EMUM. XRD analyzes were performed at 25°C by scanning the range of 3,000-90,000° in steps of 2,000° per minute. One determined from the XRD analysis results of MNs that they exhibited (220), (311), (222), (400), and (200) crystal planes structure (Image 4.16). According to these results, one can see that MNs were compatible with the studies in the literature and had the expected crystal peaks.

XRD analysis results of MENs are shown in Image 4.17. According to these results, (100), (110), (311), (111), (200), and (211) XRD peaks were observed in MEN

structures. Compared with the literature, the XRD results of MENs were almost similar as expected. Although there are some shifts, one thought that they might be caused by the analysis temperatures of the materials and some impurities, and even the dimensions of the core and shell parts may cause changes in the intensities of the peaks. For this reason, it is normal for the intensities of some peaks to weaken or strengthen.

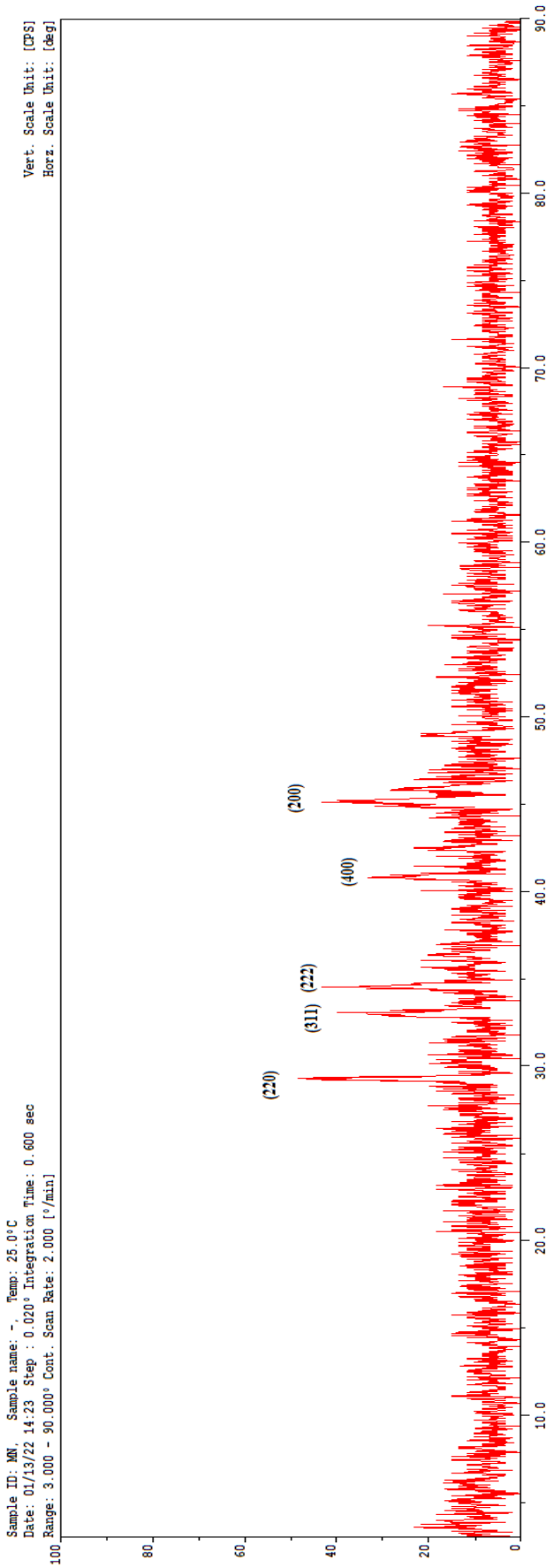

Image 4.16. *XRD analysis of MNs*

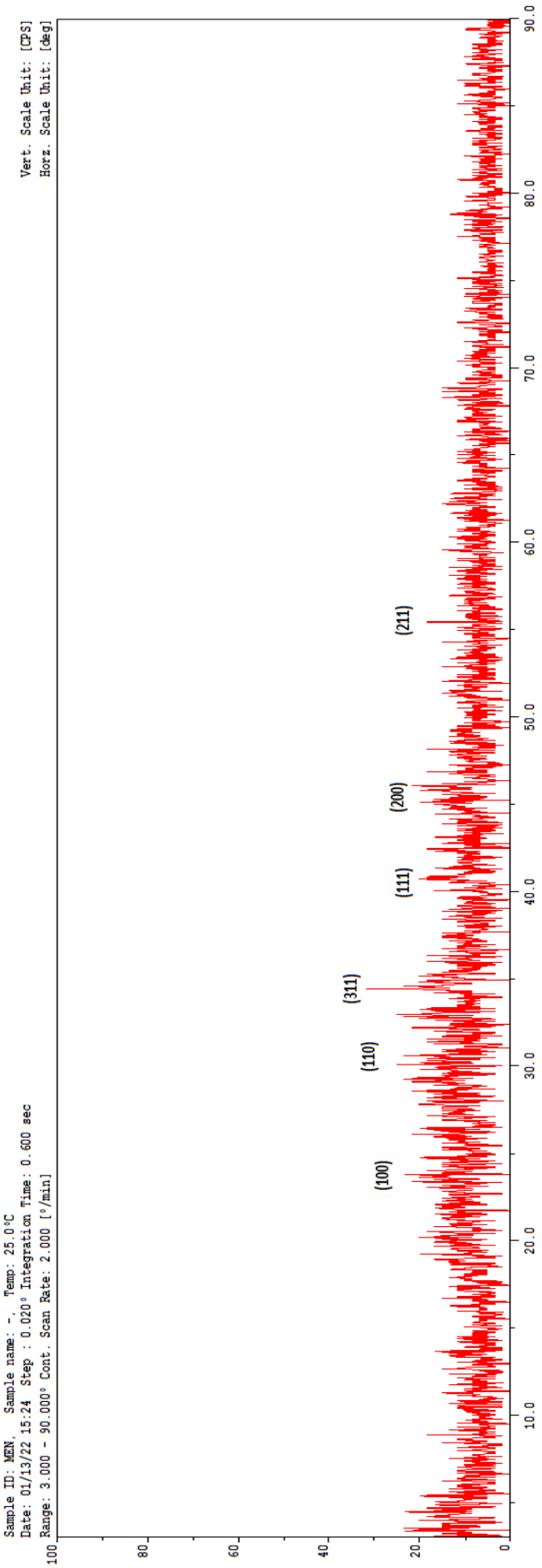

Image 4.17. *XRD analysis of MENs*

4.4. Characterizations of Lipid-Coated Formulations

The lipid-coating process was performed for drug loading to MN and MEN nanoparticles. Gelucire® 44/14 and Gelucire® 50/13 lipids were selected for lipid coat and their effects on MNs and MENs were investigated. Therefore, both placebo formulas formed with solid lipids (G44 and G50), both lipid nanoparticles loaded with MEIS (MS44 and MS50), both lipid-coated MN and MEN nanoparticles (MN44, MN50, MEN44, and MEN50), and lipid-coated nanoparticles containing MEIS (MS44MN, MS50MN, MS44MEN, and MS50MEN) formulations were prepared.

Particle size and size distribution are among the most important features of drug delivery systems. These properties determine the in vivo distribution, biological behavior, toxicity, and targeting ability of drug delivery systems (Gan et al., 2005; Othman et al., 2018).

Particle size is an important factor in the uptake of nanoparticles into the cell. The general opinion is that nanoparticles in the 120-150 nm size range are taken into the cell by clathrin or caveolin-mediated endocytosis, and nanoparticles in the 250 nm to 3 μm size range are taken into the cell by in vitro phagocytosis. In the caveola-mediated pathway, the caveolae size inhibits the uptake of larger nanoparticles. As a result, it may use multiple endocytic pathways to enter the cell, depending on the size of the particle (Foroozandeh & Aziz, 2018).

In a study conducted with Mesoporous Silica Nanoparticles, it was shown that 30, 50, 110, 170 and 280 nm colloidal systems were taken up by the cell at a higher rate (50>30>110>280>170 nm) than the 50 nm one. The cellular uptake of 50 nm particles was determined to be approximately 2.5 times that of 30 nm particles, 4 times that of 110 nm particles, 20 times that of 170 nm particles, and 11 times that of 280 nm particles (Lu et al., 2009).

PDI is a ratio in the range of 0-1 that gives information about the homogeneous distribution of particle size in a dispersion system. The decrease in the ratio towards zero indicates that the dispersion system shows a uniform and homogeneous distribution of the dispersion, which indicates the good quality of the dispersion. Although optimum values for PDI are accepted as ≤0.3, values of ≤ 0.5 are also accepted by most researchers, so it is reported that PDI should be less than ≤ 0.5 for polydisperse systems (Büyükköroğlu et al., 2016).

Particle size and distribution of the prepared formulas are presented in Table 4.3. According to these results, it was observed that the particle sizes of the formulas G44, MS44, and MS50 were below 100 nm and their PDIs were less than 0.3. These results show that the cellular uptake of the formulations will be higher compared to other formulations, and they have a homogeneous dispersion.

Table 4.3. *Particle size, PDI, and zeta potential measurements of formulations prepared within the scope of lipid coating studies.*

	Formulations	**Particle Size (nm) ± SD**	**PDI ± SD**	**Zeta Potential (mV) ± SD**
Gelucire 44/14	G44	33.70 ± 3.23	0.384 ± 0.08	-4.48 ± 0.95
	MS44	83.93 ± 4.22	0.182± 0.06	-3.57 ± 0.58
	MN44	499.4 ± 2.21	0.485 ± 0.08	-16.3 ± 0.65
	MEN44	397.1 ± 3.31	0.462 ± 0.05	-4.75 ± 0.68
	MS44MN	441.4 ± 9.67	0.728 ± 0.10	-15.4 ± 0.78
	MS44MEN	12.75 ± 1.03	0.219 ± 0.06	2.34 ± 0.53
	MN	97,31 ± 2.03	0,316 ± 0.04	-0,23 ± 0.47
	MEN	126,71 ± 4.23	0,261 ± 0.05	-0,43 ± 0.33
Gelucire 50/13	G50	132.8 ± 5.32	0.178 ± 0.12	-9.43 ± 0.63
	MS50	15.81 ± 0.75	0.288 ± 0.04	-7.49 ± 0.67
	MN50	237.5 ± 7.93	0,249 ± 0.05	-9.06 ± 0.46
	MEN50	229.23 ± 4.01	0.257 ± 0.11	-9.23 ± 0.96
	MS50MN	137.66 ± 7.02	0.541 ± 0.91	-7.88 ± 0.58
	MS50MEN	67.55 ± 4.29	0.412 ± 0.83	-11,12 ± 0.72

When the formulations without MEIS1 are considered (MN44 with MEN44 and MN50 with MEN50), it is observed that the particle sizes vary between 229.23 ± 4.01 and 499.4 ± 2.21. The fact that G44 has a smaller particle size than G50 creates the idea that Gelucire 50/13 will have a larger particle size in coated MNs and MENs. However, it was determined that MN and MEN particles coated on Gelucire 44/14 were smaller in size and more homogeneously dispersed. This result was interpreted as the organic solvent used in the coating stage with Gelucire 44/14 influenced the dispersion of lipids and particles, however; these particles might have been trapped in the lipid in larger clusters as aggregates during evaporation. In this case, it was decided that the simple emulsification method used during lipid coating is more suitable in terms of particle size.

Also, for MN, the particle size increased from 97.31 ± 2.03 nm to 499.4 ± 2.21 nm (Gelucire 44/14) and 237.5 ± 7.93 nm (Gelucire 50/13), and for MEN, it increased from 126.71 ± 4.23 nm to 397.1 ±3.31 nm (Gelucire 44/14) and 229.23 ± 4.01 nm (Gelucire 50/13). These increases indicated to coat successfully MNs and MENs with lipids. Among the lipid-coated MN and MEN formulations, only the MS44MN formulation did not show homogeneous distribution because the PID value was above 0.500 (PDI 0.728 ± 0.10).

When evaluating the particle sizes of the MEIS1 loaded lipid-coated MN and MEN formulations (MS44MN, MS44MEN, MS50MN, and MS50MEN) planned as the main formula, it was determined that the MNs were covered with MEIS1-loaded lipid. However, after coating the MENs, the particle size decreased from 126.71 ± 4.23 nm to 12.75 ± 1.03 nm and 67.55 ± 4.29 nm. This shows that the formulations interact with the active agent and form a different structure. This was also confirmed by the results of the UPLC and MEIS1 loading quantity studies. Zeta potentials of all formulations except MS44MEN were determined to be negatively charged. This is expected due to lipid coating, and these results indicate that MNs and MENs are coated with lipids. The value of 2.34 ± 0.53 mV determined in the MS44MEN formulation indicates that MEIS1 forms a different structure with MEN particles, as mentioned above. The active agent used is a newly patented substance and since clear information about the chemical structure of the substance has not been reached yet, it has not been clarified and discussed how MEIS1 interacts with the MEN structure. However, all these results indicate that MENs will not be used as a carrier system for MEIS1 coated with solid lipids Gelucire 44/14 and Gelucire 50/13.

4.5. Analytical Method Development and Validation Study

A new UPLC method has been developed to quantify MEIS. By applying parameters in different variations, the method with the most appropriate peak morphology and selectivity was achieved (ICH, 2005).

4.5.1. Linearity

The calibration curve of the active substance was found by using the field values corresponding to the samples of MEIS prepared in ethanol at concentrations of 5-100 $\mu g.\ mL^{-1}$. The calibration curve and the line equation of the curve are shown in Figure 4.1 below.

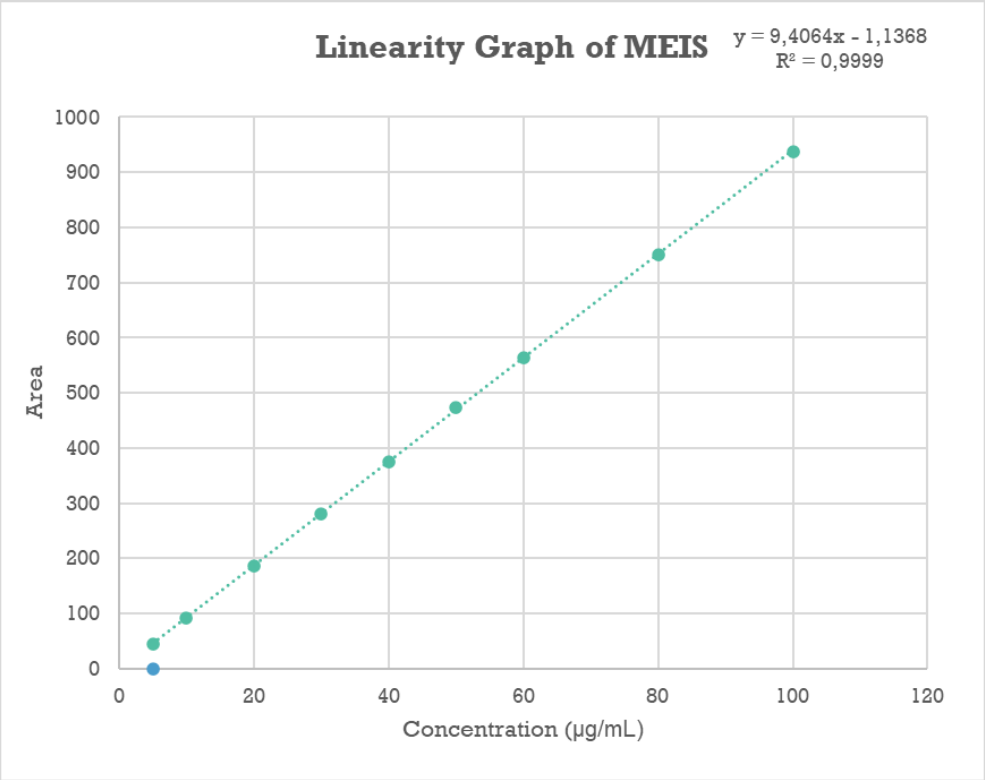

Figure 4.1. *Linearity Graph of MEIS (n=6)*

4.5.2. Precision

Solutions of MEIS at concentrations of 5, 40 and 100 µg. mL^{-1} were prepared by dissolving the active ingredient in ethanol. Three different concentrations were analyzed 3 times on three different days. Concentration calculation was made by replacing the areas obtained because of the analysis in the equation found by linearity study. The precision of the method was evaluated by calculating the coefficients of variation for the concentrations found. The findings of the precision study are shown in Table 4.4 below.

Table 4.4. *Results of Precision Study*

	1st Day	**2nd Day**	**3rd Day**
	4,98279	4,87987	4,9418
5 µg/mL	4,98519	4,94358	4,92811
	4,9939	4,97188	4,93824
Mean	4,987293	4,931776667	4,93605
Standard Deviation	0,005846	0,047126946	0,007103
Coefficient of Variation	**0,117218**	**0,955577455**	**0,143898**
	39,95542	40,06223	40,28888
40 µg/mL	39,87845	40,252	40,6133
	40,58717	40,18305	40,49776
Mean	40,14035	40,16576	40,46665
Standard Deviation	0,388869	0,096059207	0,164433
Coefficient of Variation	**0,968774**	**0,239156952**	**0,406341**

Table 4.4. (Continued) *Results of Precision Study*

	96,94006	96,92328	96,86819
100 µg/mL	98,51829	98,74599	98,47477
	98,61646	98,70716	100,4577
Mean	98,02494	98,12547667	98,60022
Standard Deviation	0,940812	1,041313863	1,79804
Coefficient of Variation	**0,959768**	**1,061206425**	**1,823566**

In the precision studies of the analytical method, the calculated coefficient of variation should be less than 2% (ICH, 2005). When the analysis results in Table 4.3 above are examined, the values obtained for all concentrations are within the accepted limits and prove the precision of the method.

4.5.3. Accuracy

Solutions of MEIS at concentrations of 5, 40 and 100 µg. mL^{-1} were prepared, and each solution was analyzed 3 times. The concentrations of the solutions were calculated by substituting the area values obtained after the analysis in the equation of the active substance. These concentrations were compared with the theoretical concentration and the accuracy of the method was evaluated over the % recovery rate obtained. The accuracy study results are presented in Table 4.5 below.

Table 4.5. *Results of Accuracy Study*

Concentration (µg/mL)	5	40	100
	4,92103	40,33298	98,70863
Obtained Concentration	4,83449	40,28821	98,45481
	4,96152	40,28267	98,33638
	98,4206	100,83245	98,70863
% Recovery	96,6898	100,72053	98,45481
	99,2304	100,70668	98,33638
Mean	98,1136	100,75322	98,49994
Standard Deviation	1,2978247	0,0689666	0,1901843
Standard Error	0,7492998	0,0400852	0,109803

For the analytical method to be considered correct, the acceptance range of the % recovery value is ±2% (ICH, 2005). When the analysis results are evaluated, all % recovery values in this thesis work are in the desired range. Thus, the accuracy of the method has been proven.

4.5.4. Sensitivity

LOD and LOQ values were calculated using 3.1 and 3.2 equations. The results are shown in Table 4.6.

Table 4.6. *Results of Sensitivity Study*

	Cut Point	**Slope (m)**
1	-1,3217	9,0601
2	2,3128	9,0926
3	-3,0497	9,3315
4	-1,9291	9,9744
5	-3,5126	9,7343
6	0,6796	9,2457
Mean	-1,136783333	9,40643333
Standard Deviation	2,243416523	0,36877392
LOD	**0,787043748**	
LOQ	**2,384981048**	

The lowest concentration of MEIS used for analytical method validation is 5 µg/mL. LOD and LOQ values of less than 5 µg/mL are evidence of the sensitivity of the analytical method.

4.5.5. Determining Loading Activity

To determine the amount of MEIS1 inhibitor loaded in the MS44, MS50, MS44MN, MS44MN, MS50MN, and MS50MEN formulations containing the MEIS1 inhibitor, samples were prepared as described in section 3.5. As a result of the analysis made with UPLC, the loading efficiency of MS44 was found to be 96.72 ± 4.23%, while the loading efficiency of MS50 was determined as 97.85 ± 6.21%.

The amount of MEIS1 inhibitor could not be calculated due to different peaks seen at the same place at the same rate in the chromatograms obtained from the MS44MN, MS44MN, MS50MN, and MS50MEN formulations. An example of the chromatogram of the different peaks is presented in figure 4.2. At this stage, it was thought that MN and MEN particles interacted chemically with the MEIS1 inhibitor and transformed into a different molecular structure. This result also supports the low particle size values of these formulations and the differences in zeta potentials.

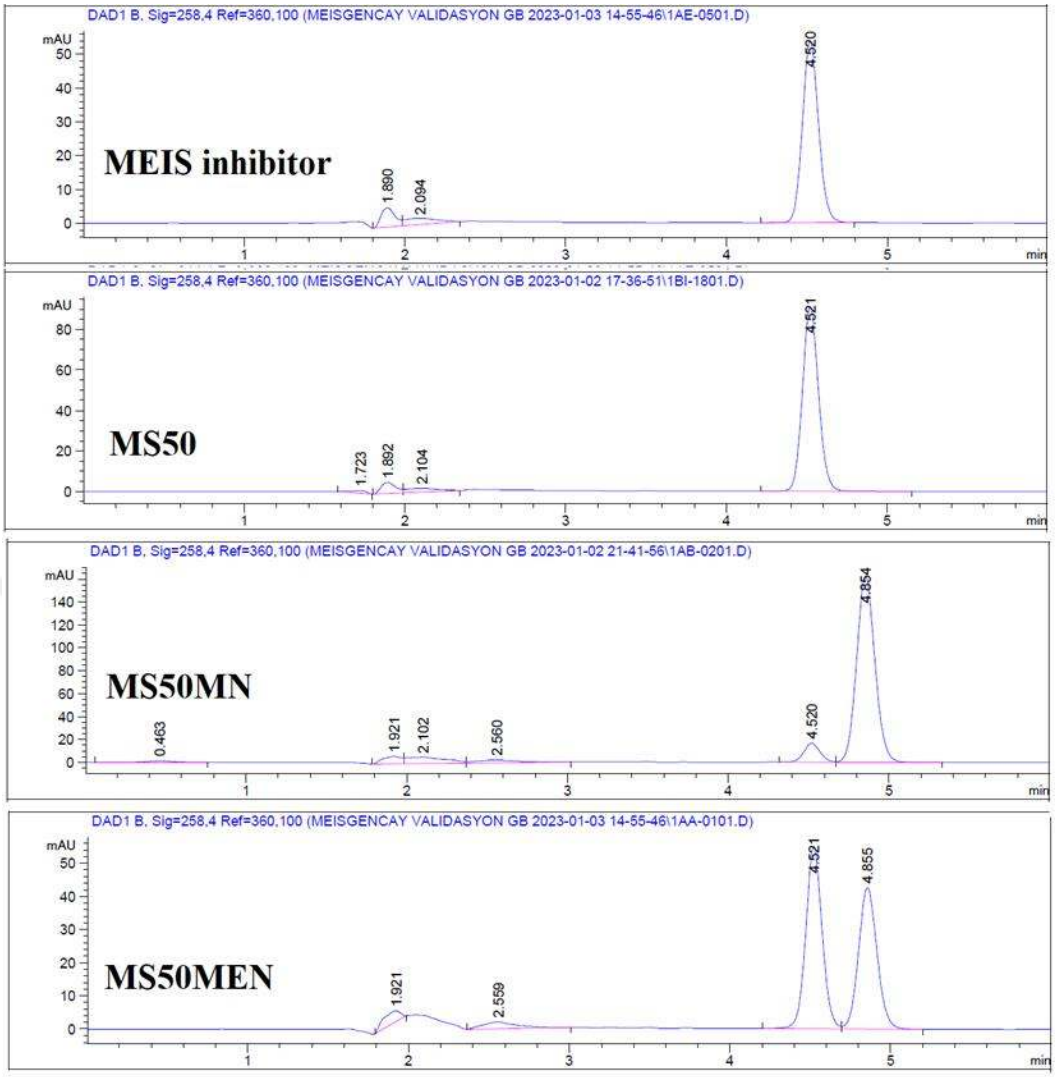

Figure 4.2. *Chromatograms of MEIS inhibitor, MS50, MS50MN, and MS50MEN formulations*

4.6. Cell Culture Studies

After MN and MENs were synthesized, healthy HUVEC and A549, and PANC-1 cancer cell lines were used to determine their toxicity on cells and their effects on cancer cells.

Cell culture studies were planned as mentioned in the Materials and Methods section and the basic procedure was applied (Büyükköroğlu et al., 2016).

First, these viability tests were applied to MNs to determine critical concentrations. As seen from the results in Figure 4.3, 24-hour viability tests of MNs were above 70% for all concentrations. However, after 48 hours of application, one observed that MNs had a cytotoxic effect on HUVEC cell lines in 10 µg and higher concentration applications. One also obtained viability results above 60% for concentrations lower than 5 µg.

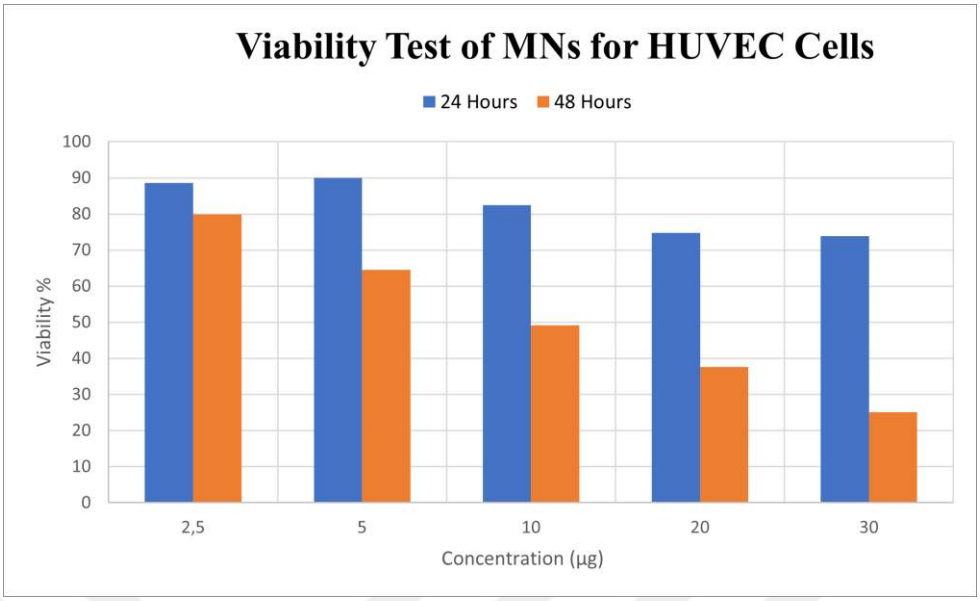

Figure 4.3. *Viability test results of MNs on HUVEC cell line*

After viability tests of MNs, the cytotoxic effects of MENs in HUVEC cell lines were investigated (Figure 4.4). Based on viability tests of MNs, one applied MENs to HUVEC cell lines at a maximum concentration of 12 µg. At the end of the application, one determined that there was no significant change in the viability of HUVEC cells after 24 and 48 hours of MEN exposure. Although the viability of the cells decreased with increasing concentration, it remained above 60% in all conditions. One observed over 80% viability for both time parameters in applications at 4 µg and lower concentrations. Therefore, based on these viability tests, one can conclude that MENs are not cytotoxic to healthy cells.

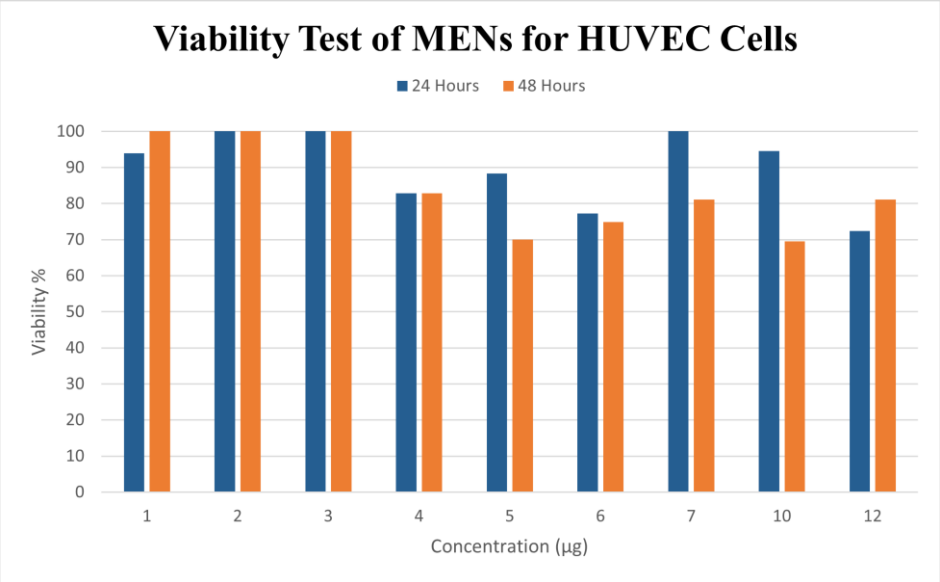

Figure 4.4. *Viability test results of MENs on HUVEC cell line*

One also used PANC-1 and A549 cell lines to examine the effects of MENs on cancer cells. Figure 4.5 shows the toxicity results of MENs applied to the PANC-1 cell line. According to these results, one determined that MENs alone did not cause toxic effects for PANC-1 cell lines. One observed that the concentration amounts of MENs did not change the toxicity. In addition, one has noticed that the application times do not cause toxic effects.

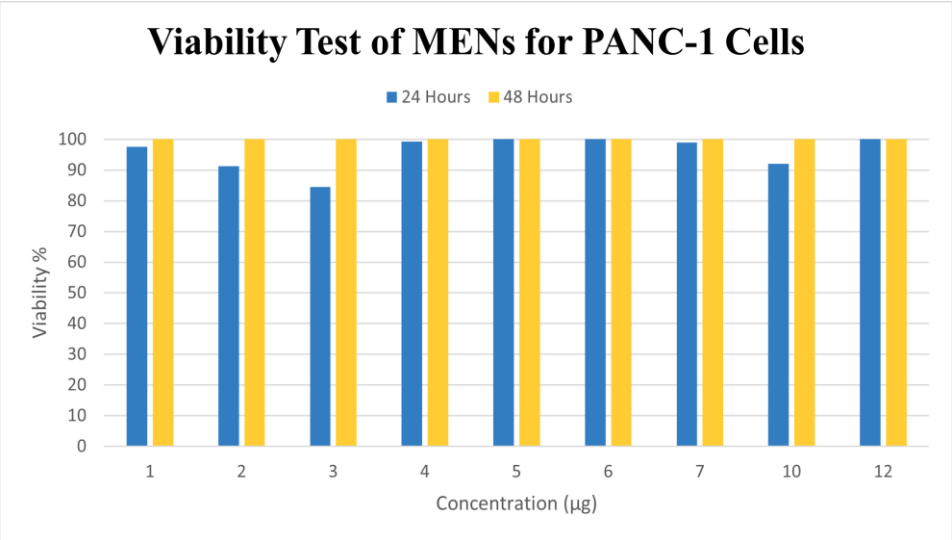

Figure 4.5. *Viability test results of MENs on PANC-1 cell line.*

After examining the effects of MENs on the pancreatic cancer cell line, one observed their impacts on the A549 cell line, as in Figure 4.6. Although different

compared to their effects on the PANC-1 cell line, one observed that they did not have a high cytotoxic impact for A549 cells in general. Although there are some deviations in the results, one noticed over 70% viabilities in the 24-hour application. In the 48-hour application, the average of all concentrations was found to be above 60%. According to these results, one understood that MENs alone would not create a toxic effect if applied to healthy and cancer cells.

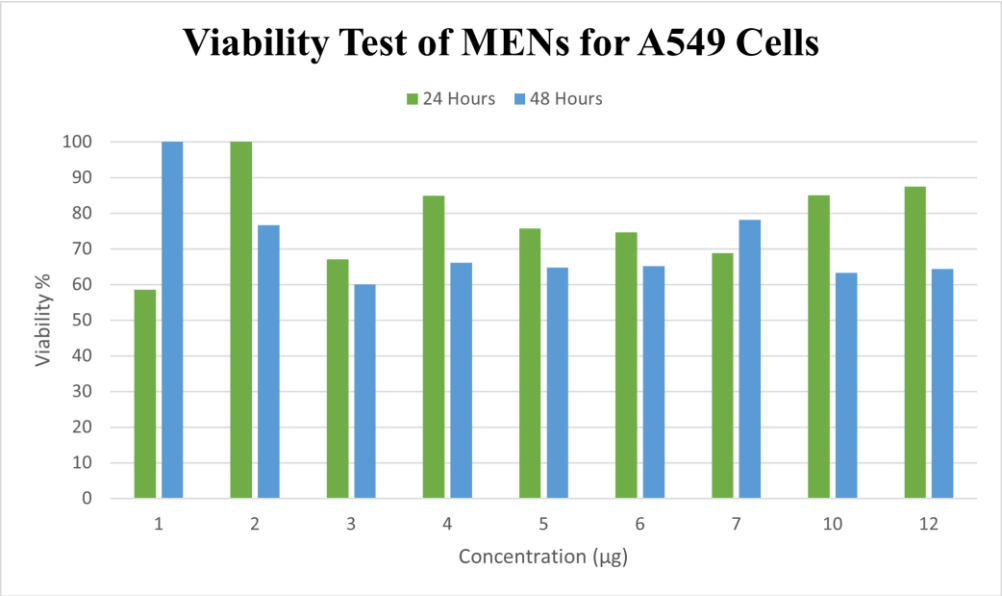

Figure 4.6. *Viability test results of MENs on A549 cell line.*

After these preliminary cell culture studies, it was determined that MN and MEN particles were non-toxic without any magnetic stimulation on a cellular basis, and the toxicity of lipid-coated and MEIS1-loaded lipid-coated forms was investigated on healthy and breast cancer cells. Of the cells used, MCF 10A is an epithelial cell line isolated from the mammary gland of a 36-year-old Caucasian woman with fibrocystic breasts in 1984 and were used as healthy cell and control group. The MCF-7 breast cancer line was derived from the pleural effusion of a 69-year-old Caucasian metastatic breast cancer (adenocarcinoma) by Dr. Soule of the Michigan Cancer Foundation, Detroit, MI in 1970, and has been used more and more in the investigation of breast cancer and metastatic breast cancer. MCF-7 cells are preferred for in vitro breast studies as they retain several ideal mammary epithelial-specific properties, such as the processing of estrogen in the form of estradiol via estrogen receptors (ER) in the cell cytoplasm. It is the first cancer cell sensitive to estrogen hormone (Souto et al., 2004).

The MDA-MB-231 cell line is an epithelial human breast cancer cell line obtained from the pleural effusion of a 51-year-old woman with metastatic breast adenocarcinoma1. This cell lacks ER and progesterone receptor (PR) expression and is defined as a triple-negative breast cancer cell because it lacks human epidermal growth factor receptor (HER2) (Cruz, 2017). Different doses of formulas applied to these cells were left to incubate for 24 and 48 hours.

Obtained results are presented in images 4.7-12. The efficacy of the lipid-coated MN and MEN formulations was compared with other formulations, the blank formulations, and the MEIS1 inhibitor. For MEIS1, 1mg of MEIS1 inhibitor was weighed, dissolved in 25 µL of DMSO and a stock solution was prepared by adding 1 mL of medium. Each dose taken from each formula in µL was applied to the cells after it was made up to 100 µL with the medium.

When the results obtained were evaluated, it was determined in Figure 4.7 those dispersions of MN and MENs in MCF-10A cells in distilled water containing 5% Tween 80 reduced cell viability below 60% for 24 and 48 hours after 1 µL dose. Also, it was observed that MENs at 24 hours and MNs at 48 hours decreased to 7% viability in 2.5 µL. This indicates that Tween 80, the surfactant used in the formulation stage, has toxic properties.

While the toxic dose of MEIS1 inhibitor was determined as 2.5 µL for 24 hours, it was determined as 0.5 µL for 48 hours. The toxicity of the G44 formulation was determined to start at 0.5 µL for 24 hours and 48 hours. This decrease in cell viability was observed at the same rates in the MN44 formulation. This indicates that the formula prepared with Gelucire 44/14, the coated particles, lipid, and Tween 80 have toxic properties.

When MEIS1 loaded formulations were compared, it was observed that the toxicity of MS44MN formulation increased with increasing dose and time. Although toxic properties were observed to increase with increasing doses in the MS44MEN formulation, this situation could not be directly correlated with the presence of the MEIS1 inhibitor. As mentioned before, it was also observed that the complex formed by MEN particles and MEIS1 caused a decrease in the toxic value.

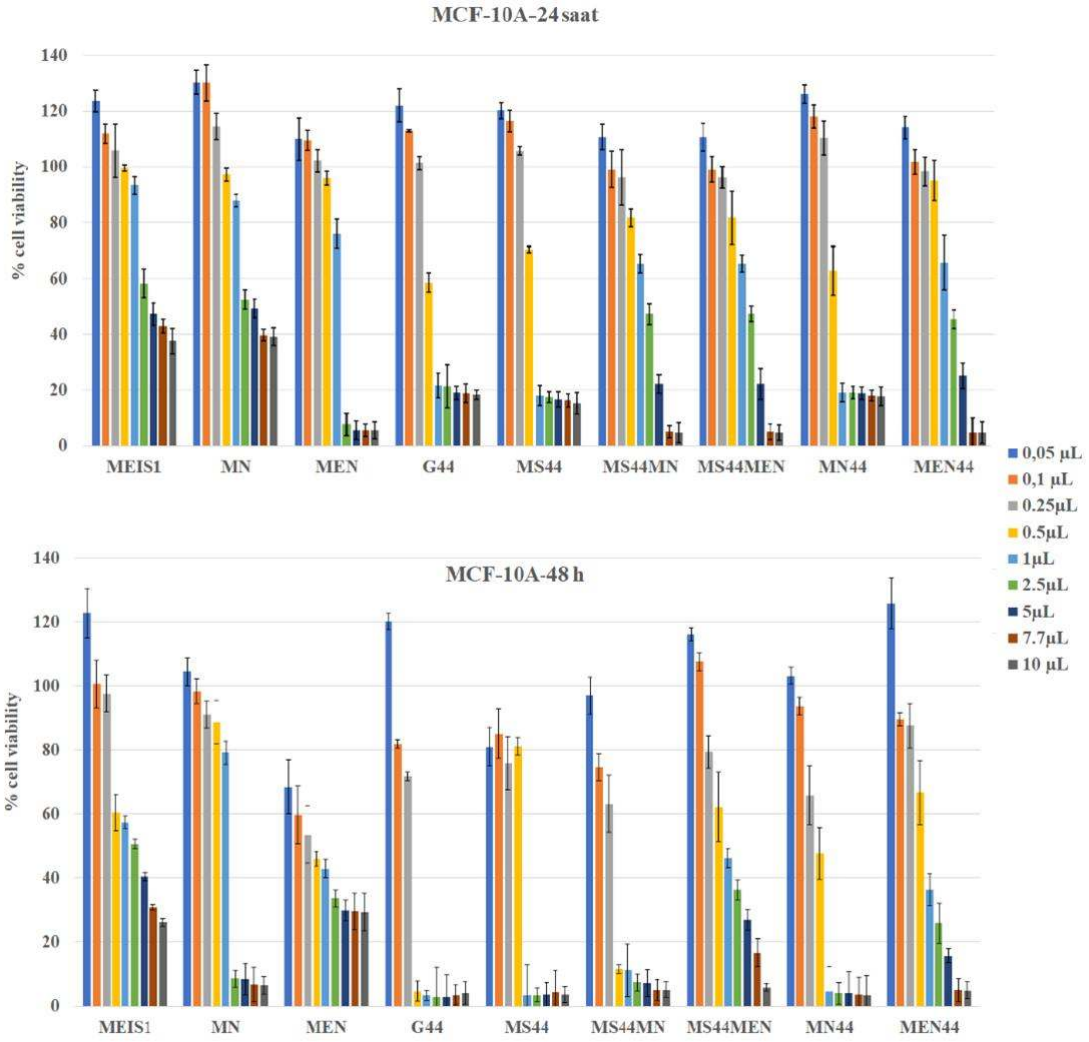

Figure 4.7. *24- and 48-hour MTT test results of formulations prepared with Gelucire44/14 on MCF-10A cells*

In Figure 4.8, the toxicity results on the MCF-7 cancer cell line are shown. Except for the MEIS1 inhibitor, results like those seen in MCF-10A were obtained in other formulations.

The toxic effect of MEIS1 in the first 24 hours is very low. At the highest doses of 7.7 µL and 10 µL, cell viability decreased below 70%. At the end of 48 hours, the dose of cell viability below 70% was observed as 1 µL. This may indicate that the MEIS1 inhibitor is uptake by the cell and MEIS protein expression is downregulated. Considering the MS44 formulation, it was determined that this formulation showed dose-dependent toxic properties at the end of 48 hours.

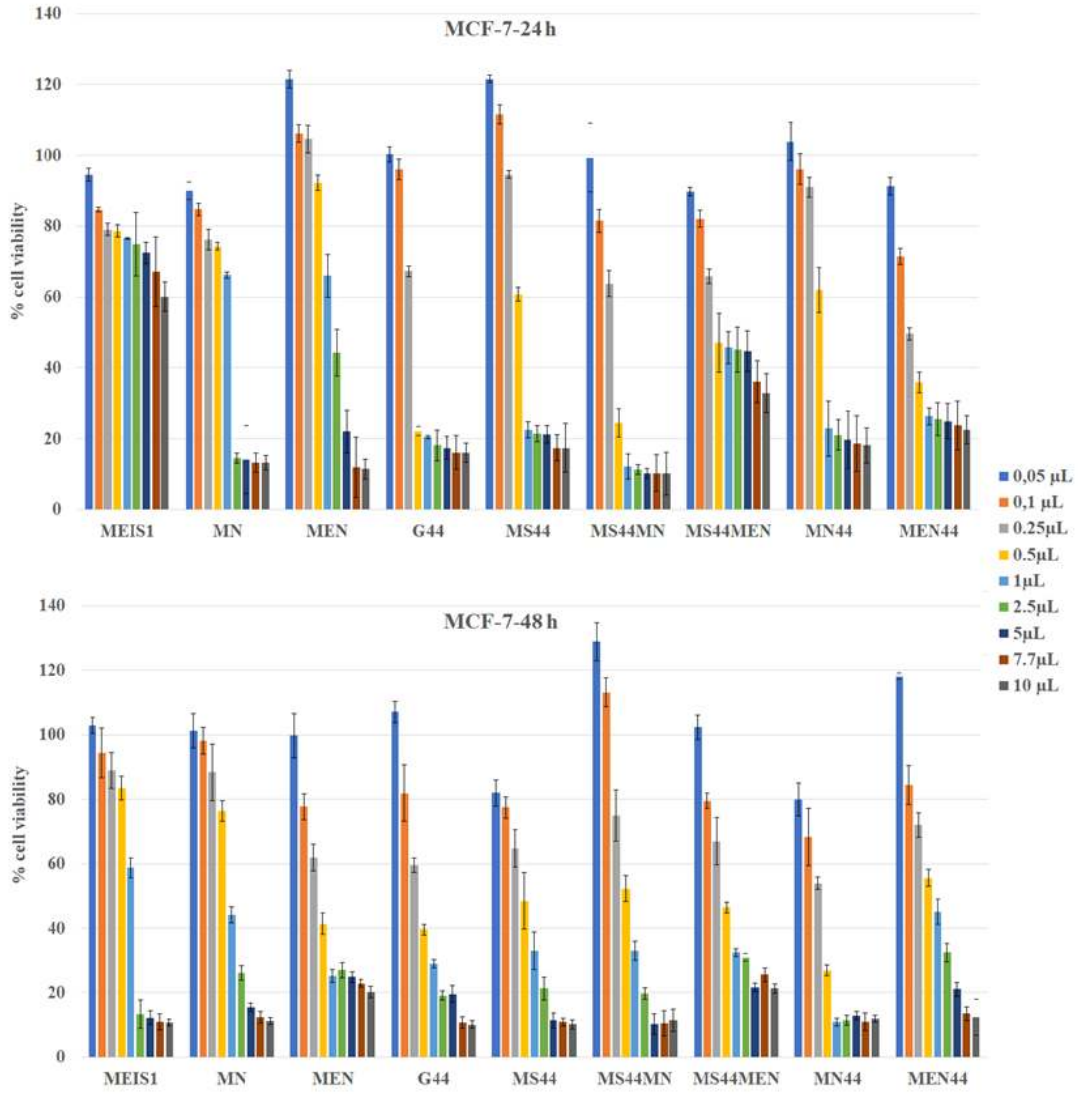

Figure 4.8. *24- and 48-hour MTT test results of formulations prepared with Gelucire44/14 on MCF-7 cells*

In the study investigating the effects of formulations prepared with Gelucire44/14 on MDA-MB-231 cells, it was determined that the MEIS1 inhibitor showed toxic properties at 0.5 µL for 24 hours and 0.1 µL for 48 hours (Figure 4.9). Compared to MCF-10A and MCF-7 cells, it can be said that MDA-MB-231 cells are the cells that can be affected by the lowest dose of MEIS1 inhibitor. However, the response of these cells to increasing doses of other formulations was lower compared to those of other cells. Cellular uptake can be also affected by cell type. The differences in cellular uptake depend on the predominant pathway each cell type uses for its cellular uptake (Adjei et al., 2014). This indicates that the cellular uptake of nanoparticles in MDA-MB-231 cells is lower than in other cells.

These cell culture results led to the use of a different lipid and preparation technique for coating, as it casts doubt on the appropriateness of the lipid and formulation preparation technique used for coating MN and MEN. For this reason, Gelucire 50/13 was used as solid lipid and formulation preparation processes were carried out with a simple emulsification technique. The results of the toxicity studies performed on the same cells as the prepared formulations are presented in Figure 4.10-12.

In these studies, MN and MEN particles were dispersed in d. water without surfactant as much as they were in formulations and applied to the cells. In addition, during the preparation of Gelucire 50/13 formulations, only 4% Tween was added to the outer phase, reducing the rate of 9% in the formulation prepared with Gelucire 44/14.

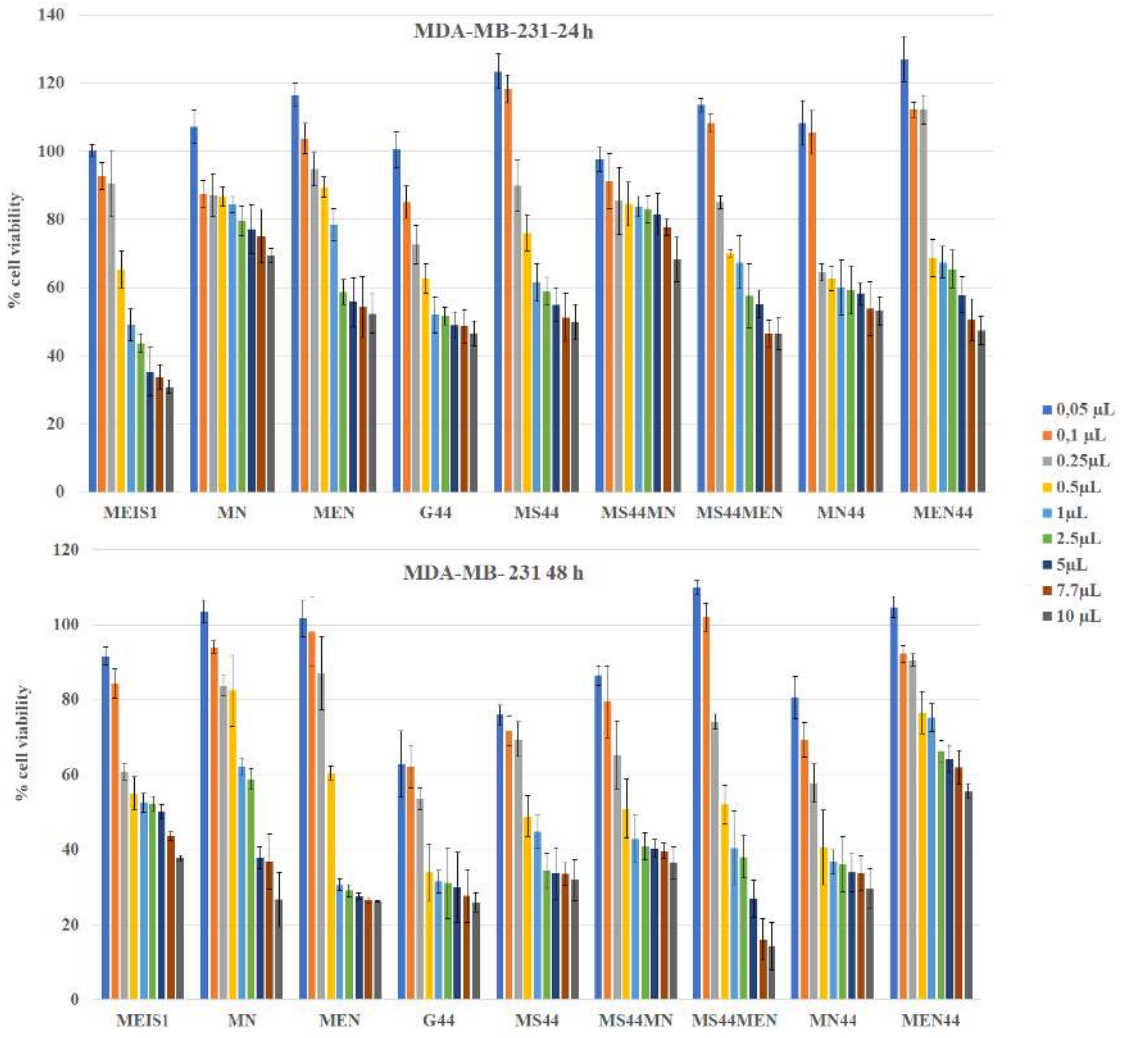

Figure 4.9. *24- and 48-hour MTT test results of formulations prepared with Gelucire44/14 on MDA-MB-231 cells*

It was determined that MN and MEN particles applied to cells without the use of surfactant were not toxic, as in the first cell culture experiments. This shows that there is a decrease in the toxicity of the G50 formulation. It was determined that the toxicity of the G50 formulation started in 1 µL for MCF-10A cells. This value was determined as 0.5 µL for G44 and corresponds to the same toxic dose for G50. As a result, it was determined that the nanoparticles prepared with Gelucire50/13 were less toxic (Figure 4.10).

It was observed that the MEIS1 inhibitor did not show toxic properties at all doses. However, it was determined that the MS50 formula prepared with Gelucire50/13 increased the cellular uptake and showed toxic properties depending on the dose and time. This was also observed for lipid-coated (MN50 and MEN) and lipid-coated (MS50MN and MS50MEN) formulations containing the MEIS1 inhibitor.

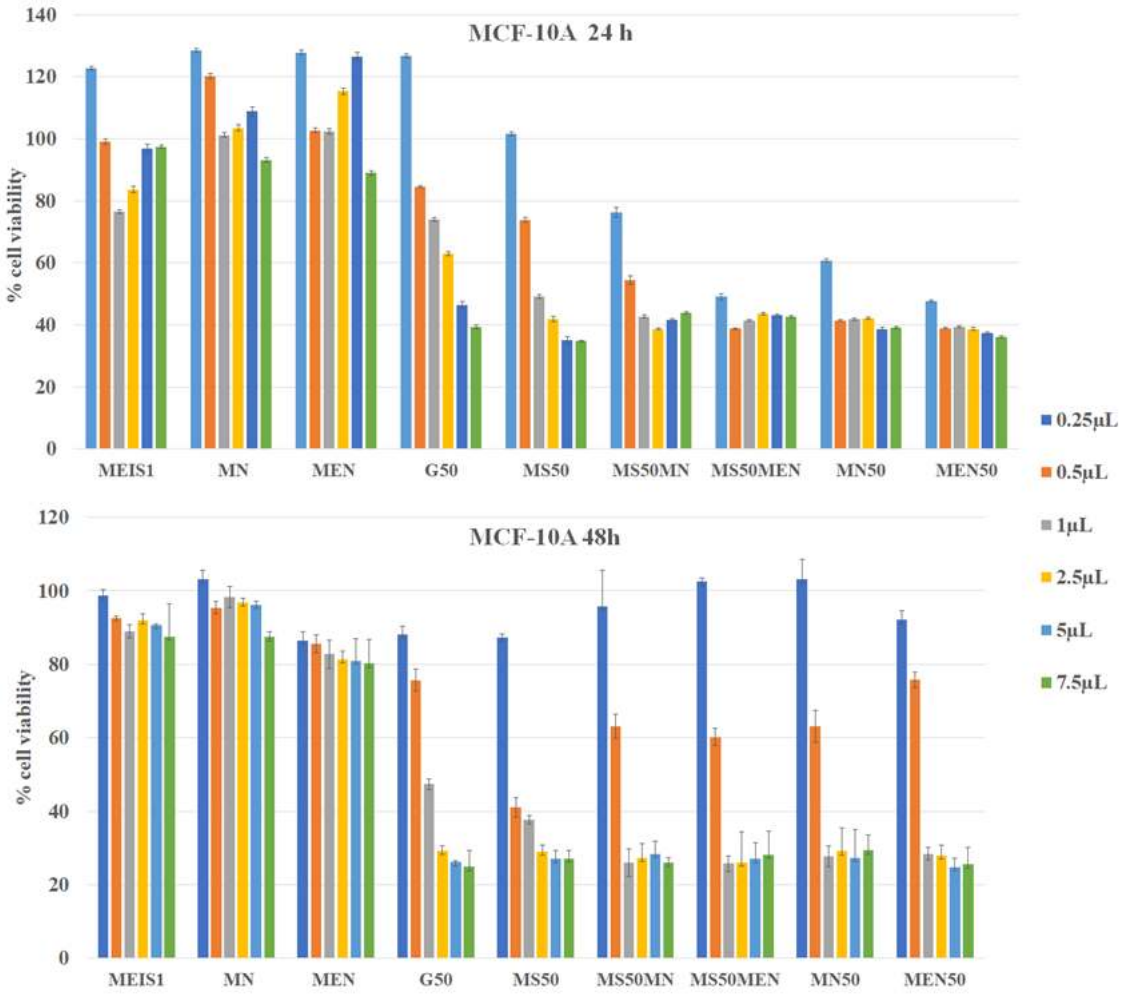

Figure 4.10. *24- and 48-hour MTT test results of formulations prepared with Gelucire50/13 on MCF-10A cells*

The toxic dose of MEIS1 inhibitor in MCF-7 cells was determined as 7.5 µL for 24 and 48 hours (Figure 4.11). This was reduced to 0.5 µL because of its formulation with Gelucire50/13 (MS50). The same effect was observed in formulations of lipid-coating MNs and MENs containing lipid and MEIS1 inhibitors. This indicates that the lipid-coating is effective in cellular uptake. It was determined that the cellular uptake of nanoparticles prepared with Gelucire50/13 was higher. In addition, it has been determined that these nanoparticles with small particle sizes are more easily taken up by the cell. In general, it is known that nanoparticles are taken into the cell by endocytosis. However, it has been stated that cellular uptake is increased compared to other particles, especially since lipidic particles containing solid lipids can be fused in the cell membrane (Nafee et al., 2020). The fact that the particle size of the formulations prepared with Gelucire 50/13 was lower than those prepared with Gelucire 44/14 increased the cellular uptake and thus the effect at lower doses.

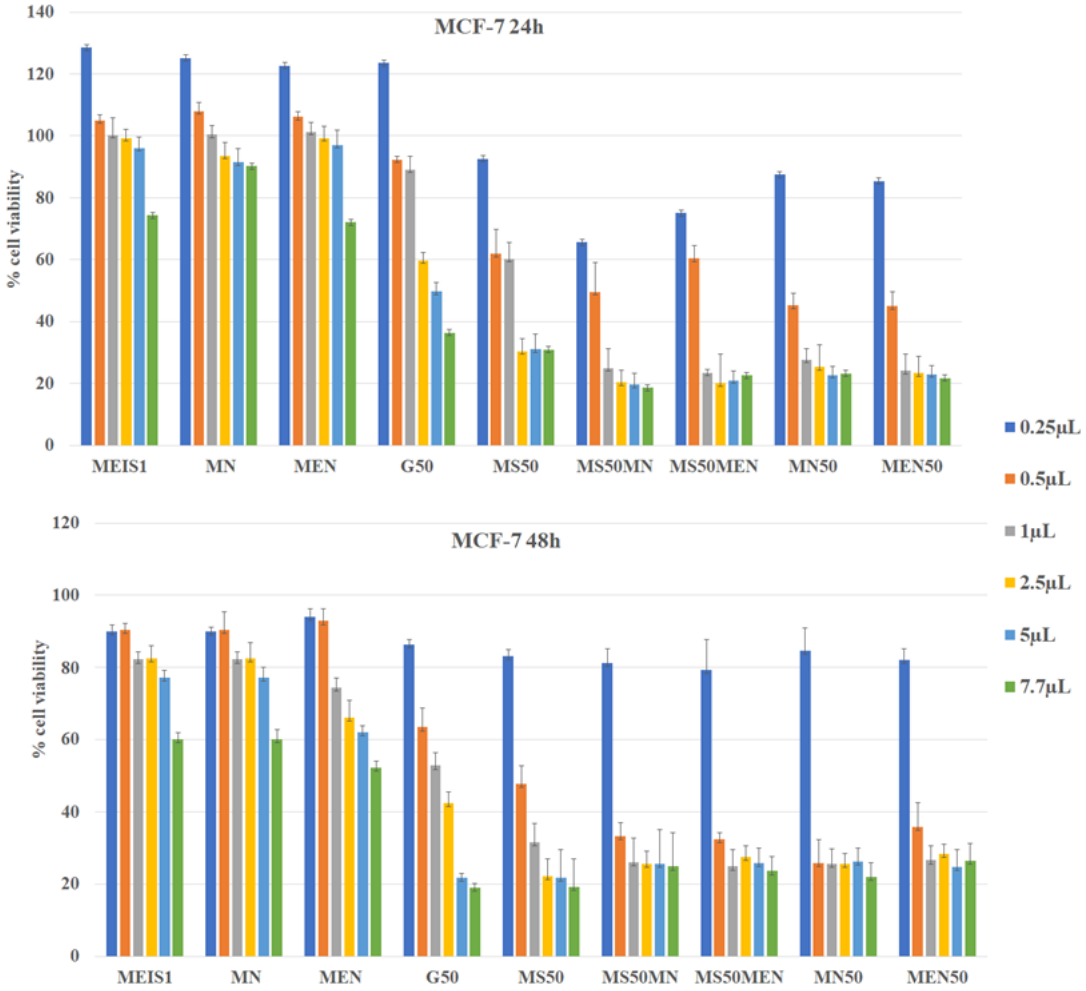

Figure 4.11. *24- and 48-hour MTT test results of formulations prepared with Gelucire50/13 on MCF-7 cells*

Although the toxicity dose of MEIS1 inhibitor, MN, and MEN particles increased by 7.5 µL in the first 24 hours on MDA-MB-231 cells, it was observed that this value was not toxic at 48 hours (Figure 4.12). Interestingly, it was determined that MN50 and MEN50 formulations showed toxic effects even at the lowest dose in the first 24 hours. This indicates that the lipidic property of Gelucire50/13 is effective in cellular uptake. Although it does not show toxic properties at 0.25 and 0.5 µL doses in 48 hours, less viability is observed at other doses than cell viability seen in 24 hours. The reason why magnetic nanoparticles have different cellular uptake mechanisms can be related to a link between cytoskeletal organizations and endocytosis. The relationship between the two systems has been determined to include interactions between different protein complexes, depending on the structure of the particles taken into the cell (Gupta & Gupta, 2005).

As a result, it was determined that MN and MENs applied to cells after being dispersed in water were not toxic to healthy MCF-10A cells at the highest doses, and they started to show toxic properties at the highest dose of 7.5 µL in MCF-7 and MDA-MB-231 cells. Also, coating with Gelucire50/13 was also observed to increase the cellular uptake of MN and MEN particles and the toxic effect of the MEIS1 inhibitor.

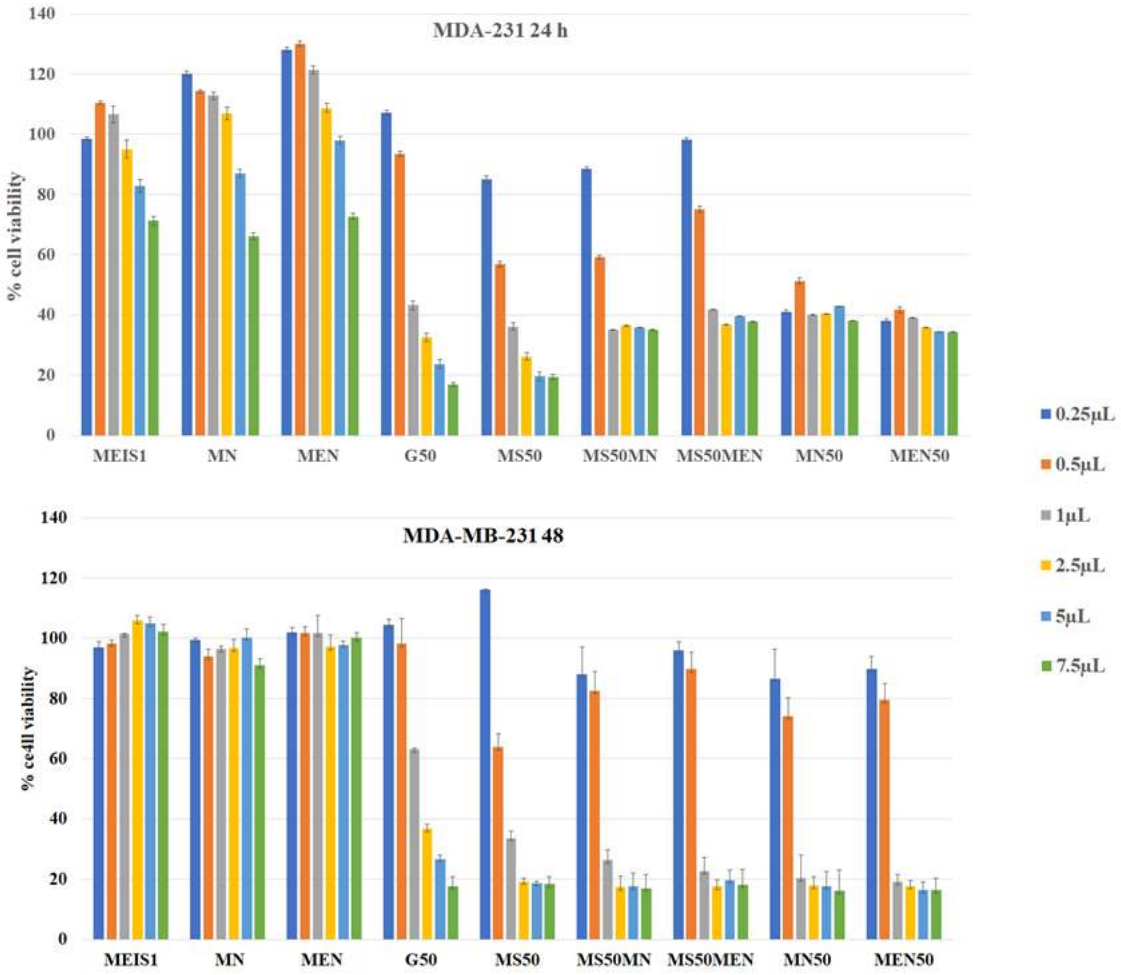

Figure 4.12. *24- and 48-hour MTT test results of formulations prepared with Gelucire50/13 on MDA-MB-231 cells*

4.7. The Data Pool Created to Determine the Limitations of MENs

In this part of the study, one has tried to create a theoretical pool that can express the interaction of MENs, synthesized and did those cytotoxicity tests with cell culture experiments, and different MENs which will be made for different studies in the future with cancer cells. The fact that one has yet to do such a simulation before in the literature has led to the need for this study. For this reason, one carried out the software and simulation of the data pool using the MATLAB 2020B program, which was

licensed by the Eskişehir Technical University Information Processing Department for university staff and students.

In the software made, one has determined the software's process limitations by using the literature studies. One knows that MENs must produce an electrical field of at least 0.1 V/μm to interact easily with cancer cells. However, if they create an electrical field of 1.5 V/μm, they can also interact with healthy cells (Etier et al., 2012; Stewart et al., 2018; Stimphil et al., 2017). For this reason, one has tried to create an ideal theoretical pool for nanoparticles that can produce electric fields in the range of 0.1-1.5 V/μm. This pool aims to determine the particle size and zeta potential of MENs, synthesized in the laboratory environment, and to theoretically predict that nanoparticles produced before determining their cytotoxicity with cell culture experiments can only interact with cancer cells without affecting healthy cells. In this way, synthesized nanoparticles will be easily excluded or included according to the desired physical properties before being tested in cell culture experiments. Not only within the scope of this study but also the scope of future studies, if it comes to working with magneto-electric nanoparticles, one will use this designed and written code easily. The full version of the corresponding MATLAB code is shown in Supplementary Document-1.

The code consists of four primary parts: "Parameters," "Simulation of the generated electrical field," "Selection of suitable electrical fields for cancer cells," and "Selection of appropriate zeta potential, particle radius, and critical distance for cancer cells."

In the "Parameters" section, one calculates and assigns the initial values of each physical parameter to be used in the following sections of the code.

In the "Simulation of the generated electrical field" section, one performs the simulation of the electrical field to be created. At this stage, an electrical potential pool is created, as in Image 4.18, according to each zeta potential, particle radius, and critical distance. This pool contains all electrical field possibilities within the defined constraints, as seen in Image 4.18. One also designs this pool to contain nanoparticles that generate electrical fields that may not interact with cancer cells and with healthy cells. One extracts them and determines the appropriate parameters in the next section of the code.

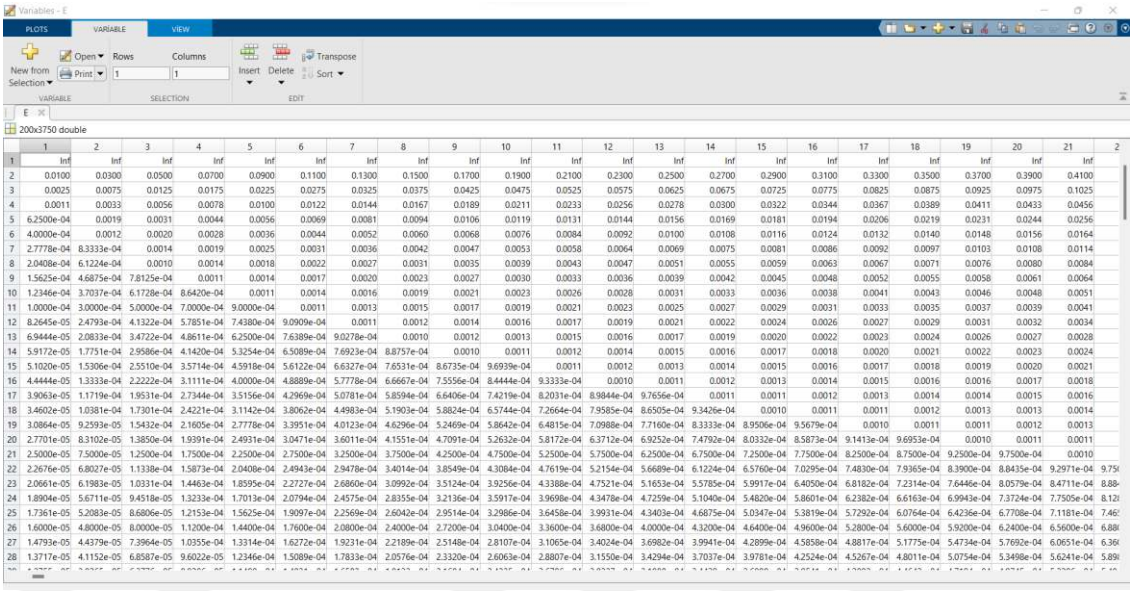

Image 4.18. *The pool containing all the electrical fields that can be produced according to each parameter within the determined limits.*

In the "Selection of suitable electrical fields for cancer cells" section, features such as the zeta potential and particle radius of nanoparticles that can produce the appropriate electrical field by back-computing and by extracting all the possibilities of the electrical field created in the previous section are determined. As shown in Image 4.19, one has extracted the pool containing all the possibilities in Image 4.18. One used two critical limits in the extraction process. One of these two limits is electrical fields large enough to interact with healthy cells. The other is electrical fields that are too low to interact with cancer cells. Values in these two boundaries are removed. Thus, only electrical fields that have the potential to interact with cancer cells remain in the theoretical electrical field pool.

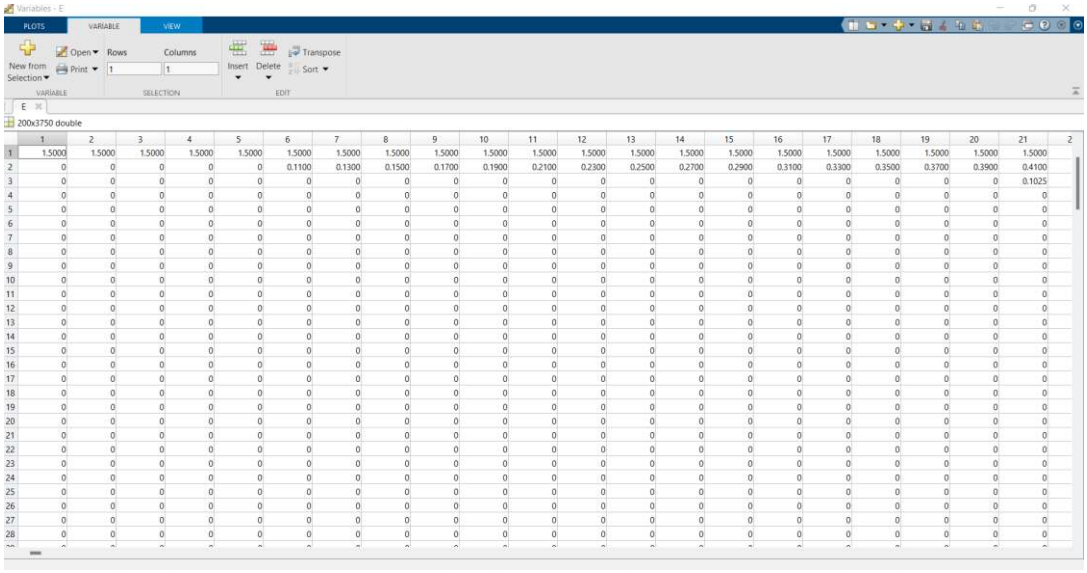

Image 4.19. *Pool of electrical fields in the theoretical window from which nanoparticles producing electrical fields high enough to interact with healthy cells and low enough not to interact with cancer cells are extracted.*

In the last part of the code, one determined the appropriate zeta potential, particle radius, and critical distance for nanoparticles that can only interact with cancer cells by performing a back calculation for the generated electrical field (Image 4.20).

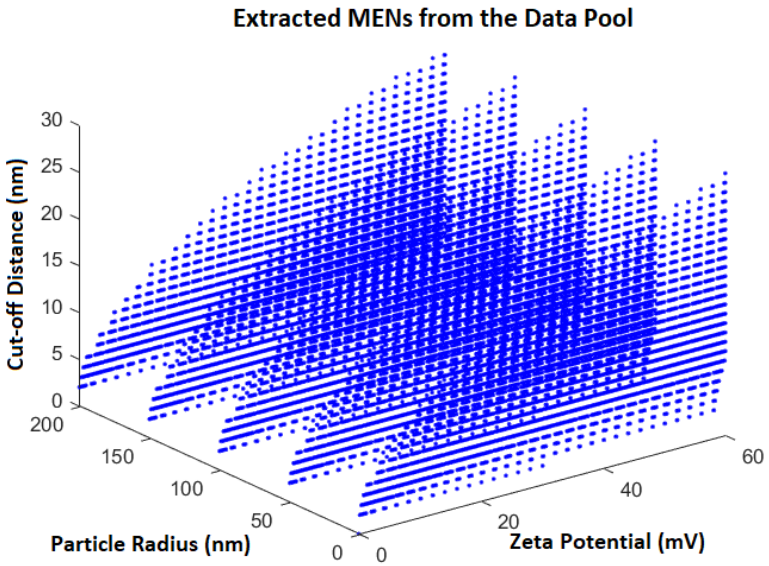

Image 4.20. *Graph showing the zeta potentials, particle radii and critical distance of nanoparticles that can generate the appropriate electric field.*

As a result, with this simulation study, the cellular interaction parameters of MENs were determined theoretically using a simulation that has never been done before in the literature.

5. CONCLUSION

It was determined that MN and MEN particles synthesized within the scope of this study could be highly magnetized and have the desired physical properties. It has been determined that they show these properties when they are dispersed in distilled water and in dispersions formed by coating with lipids such as Gelucire 44/14 and Gelucire 50/13. However, after coating with a MEIS inhibitor-loaded lipid layer, a decrease in the number of oriented particles was observed. This indicated that their magnetic properties change because of their chemical interaction with the MEIS1 inhibitor. Since the clarification of this situation can be a different research topic, it has not been evaluated within the scope of this thesis.

Cell culture studies have shown that lipid-coated MN and MENs increase their uptake into the cell and can have a toxic effect after they are taken into the cell without applying any magnetic field. This shows that it will be possible for an active agent that will not interact chemically with the MN and MEN structure to be loaded onto the lipid layer and directed this active agent to the target region with a magnetic field.

Due to the difficulties experienced in treating bone cancer, one is studying targetable drug delivery systems. In this context, one needs structures that can be applied and targeted externally. In this study, the potential of using the targeted drug delivery system, which was synthesized and formulated for the treatment of metastatic bone cancer, was tested by cell culture studies due to the disruptions experienced caused by the COVID-19 pandemic. These studies showed that a targeted drug delivery system has been designed that can have a synergistic effect when used together with different active substances and different cancer treatment methods in the treatment of different cancers.

In future studies, it is aimed to complete our objectives of "determining the effectiveness of formulations in vitro as a result of magnetic field application" and "in vivo evaluation with animal experiments", which could not be succeeded due to the loss of time caused by the Covid-19 pandemic. Afterward, it is aimed to develop the targeted drug delivery systems prepared in this study, to examine their effectiveness in different cancer types and bone-like structures, and to test their applicability.

REFERENCES

Agostinis, P., Berg, K., Cengel, K. A., Foster, T. H., Girotti, A. W., Gollnick, S. O., Hahn, S. M., Hamblin, M. R., Juzeniene, A., Kessel, D., Korbelik, M., Moan, J., Mroz, P., Nowis, D., Piette, J., Wilson, B. C., & Golab, J. (2011). Photodynamic therapy of cancer: an update. *CA: A Cancer Journal for Clinicians*, *61*(4), 250–281.

Aksoz, M., Turan, R. D., Albayrak, E., & Kocabas, F. (2018). Emerging Roles of Meis1 in Cardiac Regeneration, Stem Cells and Cancer. *Current Drug Targets*, *19*(2).

Angel García Sáenz, J., López Tarruella, S., García Paredes, B., Rodríguez Lajusticia, L., Villalobos, L., Díaz Rubio, E., Ángel García-Sáenz, J. C., Lagos, M., & Osteonecrosis, D.-R. E. (2007). Osteonecrosis of the jaw as an adverse bisphosphonate event: Three cases of bone metastatic prostate cancer patients treated with zoledronic acid. *Medicina Oral, Patología Oral y Cirugía Bucal (Internet)*, *12*(5), 351–356.

Arem, H., & Loftfield, E. (2018). Cancer Epidemiology: A Survey of Modifiable Risk Factors for Prevention and Survivorship. *American Journal of Lifestyle Medicine*, *12*(3), 200.

Ascher, E., Rieder, H., Schmid, H., & Stössel, H. (2004). Some Properties of Ferromagnetoelectric Nickel-Iodine Boracite, Ni3B7O13I. *Journal of Applied Physics*, *37*(3), 1404.

Astrov, D. N. (1960). The magnetoelectric effect in antiferromagnetics. *Sov. Phys. JETP*, *11*(3), 708–709.

Badran, M. (n.d.). Formulation and In Vitro Evaluation of Flufenamic Acid Loaded Deformable Liposomes for Improved Skin Delivery. *Digest Journal of Nanomaterials and Biostructures*, *9*(1), 83–91.

Bandi, P., Minihan, A. K., Siegel, R. L., Islami, F., Nargis, N., Jemal, A., & Fedewa, S. A. (2021). Updated Review of Major Cancer Risk Factors and Screening Test Use in the United States in 2018 and 2019, with a Focus on Smoking Cessation. *Cancer Epidemiology, Biomarkers & Prevention: A Publication of the American Association for Cancer Research, Cosponsored by the American Society of Preventive Oncology*, *30*(7), 1287–1299.

Bañobre-López, M., Teijeiro, A., & Rivas, J. (2013). Magnetic nanoparticle-based hyperthermia for cancer treatment. *Reports of Practical Oncology and Radiotherapy*, *18*(6), 397.

Barenholz, Y. (2012). Doxil®--the first FDA-approved nano-drug: lessons learned. *Journal of Controlled Release: Official Journal of the Controlled Release Society*, *160*(2), 117–134.

Bazak, R., Houri, M., el Achy, S., Kamel, S., & Refaat, T. (2015). Cancer active targeting by nanoparticles: a comprehensive review of literature. *Journal of Cancer Research and Clinical Oncology*, *141*(5), 769–784.

Beik, J., Abed, Z., Ghoreishi, F. S., Hosseini-Nami, S., Mehrzadi, S., Shakeri-Zadeh, A., & Kamrava, S. K. (2016). Nanotechnology in hyperthermia cancer therapy: From fundamental principles to advanced applications. *Journal of Controlled Release: Official Journal of the Controlled Release Society*, *235*, 205–221.

Benov, L. (2015). Photodynamic therapy: current status and future directions. *Medical Principles and Practice: International Journal of the Kuwait University, Health Science Centre*, *24 Suppl 1*(Suppl 1), 14–28.

Bérard, A., & Mohrbach, H. (2006). Spin Hall effect and Berry phase of spinning particles. *Physics Letters A*, *352*(3), 190–195.

Berg, J. M., Romoser, A., Banerjee, N., Zebda, R., & Sayes, C. M. (2009). The relationship between pH and zeta potential of ~ 30 nm metal oxide nanoparticle suspensions relevant to in vitro toxicological evaluations, *Nanotoxicology*, *3*(4), 276–283.

Bertrand, N., Wu, J., Xu, X., Kamaly, N., & Farokhzad, O. C. (2014). Cancer nanotechnology: the impact of passive and active targeting in the era of modern cancer biology. *Advanced Drug Delivery Reviews*, *66*, 2–25.

Biermann, J. S. (2013). Updates in the Treatment of Bone Cancer. *Journal of the National Comprehensive Cancer Network*, *11*(5S), 681–683.

Biermann, J. S., Chow, W., Reed, D. R., Lucas, D., Adkins, D. R., Agulnik, M., Benjamin, R. S., Brigman, B., Budd, G. T., Curry, W. T., Didwania, A., Fabbri, N., Hornicek, F. J., Kuechle, J. B., Lindskog, D., Mayerson, J., McGarry, S. v, Million, L., Morris, C. D., … Scavone, J. L. (2017). NCCN Guidelines Insights: Bone Cancer, Version 2.2017. *Journal of the National Comprehensive Cancer Network*, *15*(2), 155–167.

Bruno, P., Dugaev, V. K., & Taillefumier, M. (2004). Topological Hall effect and Berry phase in magnetic napostructures. *Physical Review Letters*, *93*(9), 096806.

Büyükköroğlu, G., Şenel, B., Başaran, E., Yenilmez, E., & Yazan, Y. (2016). Preparation and in vitro evaluation of vaginal formulations including siRNA and paclitaxel-loaded SLNs for cervical cancer. *European Journal of Pharmaceutics and Biopharmaceutics*, *109*, 174–183.

Cecchini, M. G., Wetterwald, A., van der Pluijm, G., & Thalmann, G. N. (2005). Molecular and Biological Mechanisms of Bone Metastasis. *EAU Update Series*, *3*(4), 214–226.

Chang, S. H., Lin, H. T. V., Wu, G. J., & Tsai, G. J. (2015). pH Effects on solubility, zeta potential, and correlation between antibacterial activity and molecular weight of chitosan. *Carbohydrate Polymers*, *134*, 74–81.

Chen, Y. W., Su, Y. L., Hu, S. H., & Chen, S. Y. (2016). Functionalized graphene nanocomposites for enhancing photothermal therapy in tumor treatment. *Advanced Drug Delivery Reviews*, *105*, 190–204.

Chou, T. C. (2010). Drug combination studies and their synergy quantification using the Chou-Talalay method. *Cancer Research*, *70*(2), 440–446.

Clarke, S. (2013). *Development of hierarchical magnetic nanocomposite materials for biomedical applications*., (Doctoral dissertation, Dublin City University).

Clogston, J. D., & Patri, A. K. (2011). Zeta potential measurement. *Methods in Molecular Biology (Clifton, N.J.)*, *697*, 63–70.

Collins, M. N., Ren, G., Young, K., Pina, S., Reis, R. L., & Oliveira, J. M. (2021). Scaffold Fabrication Technologies and Structure/Function Properties in Bone Tissue Engineering. *Advanced Functional Materials*, *31*(21), 2010609.

Cravo, A. S., & Mrsny, R. J. (2013). A time travel journey through cancer therapies. *Cancer Targeted Drug Delivery: An Elusive Dream*, *9781461478768*, 3–35.

Crist, R. C., Roth, J. J., Waldman, S. A., & Buchberg, A. M. (2011). A conserved tissue-specific homeodomain-less isoform of MEIS1 is downregulated in colorectal cancer. *PloS One*, *6*(8).

Curie, P. (1894). Sur la symétrie dans les phénomènes physiques, symétrie d'un champ électrique et d'un champ magnétique. *J. Phys. Theor. Appl.*, *3*(1), 393–415.

Dai, X., & Tan, C. (2015). Combination of microRNA therapeutics with small-molecule anticancer drugs: mechanism of action and co-delivery nanocarriers. *Advanced Drug Delivery Reviews*, *81*, 184–197.

Danaei, M., Dehghankhold, M., Ataei, S., Hasanzadeh Davarani, F., Javanmard, R., Dokhani, A., Khorasani, S., & Mozafari, M. R. (2018). Impact of Particle Size and Polydispersity Index on the Clinical Applications of Lipidic Nanocarrier Systems. *Pharmaceutics*, *10*(2).

de Smet, M., Langereis, S., den Bosch, S. van, & Grüll, H. (2010). Temperature-sensitive liposomes for doxorubicin delivery under MRI guidance. *Journal of Controlled Release: Official Journal of the Controlled Release Society*, *143*(1), 120–127.

de Smet, M., Langereis, S., van den Bosch, S., Bitter, K., Hijnen, N. M., Heijman, E., & Grüll, H. (2013). SPECT/CT imaging of temperature-sensitive liposomes for MR-image guided drug delivery with high intensity focused ultrasound. *Journal of Controlled Release: Official Journal of the Controlled Release Society*, *169*(1–2), 82–90.

Dellian, M., Witwer, B. P., Salehi, H. A., Yuan, F., & Jain, R. K. (1996). Quantitation and physiological characterization of angiogenic vessels in mice: effect of basic fibroblast growth factor, vascular endothelial growth factor/vascular permeability factor, and host microenvironment. *The American Journal of Pathology*, *149*(1), 59.

DeVita, V. T., & Chu, E. (2008). A history of cancer chemotherapy. *Cancer Research*, *68*(21), 8643–8653.

Du, J. Z., Du, X. J., Mao, C. Q., & Wang, J. (2011). Tailor-Made dual pH-sensitive polymer-doxorubicin nanoparticles for efficient anticancer drug delivery. *Journal of the American Chemical Society*, *133*(44), 17560–17563.

Dzyaloshinskiĭ, I. (1960). On the magneto-electrical effects in antiferromagnets. *Soviet Physics, JETP*.

Ekambaram, P., Abdul, A., Sathali, H., & Priyanka, K. (2012). SOLID LIPID NANOPARTICLES: A REVIEW. *Sci. Revs. Chem. Commun*, *2*(1), 80–102.

Etier, M., Gao, Y., Shvartsman, V. v, Elsukova, A., Landers, J., Wende, H., & Lupascu, D. C. (2012). Cobalt Ferrite/Barium Titanate Core/Shell Nanoparticles. *Ferroelectrics*, *438*(1), 115–122.

Falk, M. H., & Issels, R. D. (2001). Hyperthermia in oncology. *International Journal of Hyperthermia: The Official Journal of European Society for Hyperthermic Oncology, North American Hyperthermia Group*, *17*(1), 1–18.

Ferlay, J., Colombet, M., Soerjomataram, I., Parkin, D. M., Piñeros, M., Znaor, A., & Bray, F. (2021). Cancer statistics for the year 2020: An overview. *International Journal of Cancer*, *149*(4), 778–789.

Florencio-Silva, R., Sasso, G. R. D. S., Sasso-Cerri, E., Simões, M. J., & Cerri, P. S. (2015). Biology of Bone Tissue: Structure, Function, and Factors That Influence Bone Cells. *BioMed Research International*, *2015*.

Frank, S. A. (2004). Genetic predisposition to cancer — insights from population genetics. *Nature Reviews Genetics 2004 5:10*, *5*(10), 764–772.

Geerts, D., Revet, I., Jorritsma, G., Schilderink, N., & Versteeg, R. (2005). MEIS homeobox genes in neuroblastoma. *Cancer Letters*, *228*(1–2), 43–50.

Greenlee, R. T., Murray, T., Bolden, S., & Wingo, P. A. (2000). Cancer statistics, 2000. *CA: A Cancer Journal for Clinicians*, *50*(1), 7–33.

Grünewald, T. G. P., Cidre-Aranaz, F., Surdez, D., Tomazou, E. M., de Álava, E., Kovar, H., Sorensen, P. H., Delattre, O., & Dirksen, U. (2018). Ewing sarcoma. *Nature Reviews. Disease Primers*, *4*(1).

Guduru, R., Liang, P., Runowicz, C., Nair, M., Atluri, V., & Khizroev, S. (2013). Magnetoelectric nanoparticles to enable field-controlled high-specificity drug delivery to eradiate ovarian cancer cells. *Scientific Reports*, *3*, 2953.

Guo, L., Liang, Z., Yang, L., Du, W., Yu, T., Tang, H., Li, C., & Qiu, H. (2021). The role of natural polymers in bone tissue engineering. *Journal of Controlled Release*, *338*, 571–582.

Hashizume, H., Baluk, P., Morikawa, S., McLean, J. W., Thurston, G., Roberge, S., Jain, R. K., & McDonald, D. M. (2000). Openings between defective endothelial cells explain tumor vessel leakiness. *The American Journal of Pathology*, *156*(4), 1363–1380.

Hassan, P. A., Rana, S., & Verma, G. (2015). Making sense of Brownian motion: Colloid characterization by dynamic light scattering. *Langmuir*, *31*(1), 3–12.

Hassanpour, S. H., & Dehghani, M. (2017). Review of cancer from perspective of molecular. *Journal of Cancer Research and Practice*, *4*(4), 127–129.

Henriksen, P. A. (2018). Anthracycline cardiotoxicity: an update on mechanisms, monitoring and prevention. *Heart (British Cardiac Society)*, *104*(12), 971–977.

Hildebrandt, B., Wust, P., Ahlers, O., Dieing, A., Sreenivasa, G., Kerner, T., Felix, R., & Riess, H. (2002). The cellular and molecular basis of hyperthermia. *Critical Reviews in Oncology/Hematology*, *43*(1), 33–56.

Hobbs, S. K., Monsky, W. L., Yuan, F., Roberts, W. G., Griffith, L., Torchilin, V. P., & Jain, R. K. (1998). Regulation of transport pathways in tumor vessels: Role of tumor type and microenvironment. *Proceedings of the National Academy of Sciences of the United States of America*, *95*(8), 4607–4612.

Høgdall, E. V. S., Christensen, L., Kjaer, S. K., Blaakaer, J., Kjærbye-Thygesen, A., Gayther, S., Jacobs, I. J., & Høgdall, C. K. (2007). CA125 expression pattern,

prognosis and correlation with serum CA125 in ovarian tumor patients. From The Danish "MALOVA" Ovarian Cancer Study. *Gynecologic Oncology*, *104*(3), 508–515.

Huh, K. M., Kang, H. C., Lee, Y. J., & Bae, Y. H. (2012). pH-sensitive polymers for drug delivery. *Macromolecular Research 2012 20:3*, *20*(3), 224–233.

Iyer, A. K., Khaled, G., Fang, J., & Maeda, H. (2006). Exploiting the enhanced permeability and retention effect for tumor targeting. *Drug Discovery Today*, *11*(17–18), 812–818.

Jurgons, R., Seliger, C., Hilpert, A., Trahms, L., Odenbach, S., & Alexiou, C. (2006). Drug loaded magnetic nanoparticles for cancer therapy. *Journal of Physics: Condensed Matter*, *18*(38), S2893.

Khan, I., Khan, M., Umar, M. N., & Oh, D. H. (2015). Nanobiotechnology and its applications in drug delivery system: a review. *IET Nanobiotechnology*, *9*(6), 396–400.

Khomskii, D. (2009). Classifying multiferroics: Mechanisms and effects. *Physics*, *2*, 20.

Khomskii, D. I. (2006). Multiferroics: Different ways to combine magnetism and ferroelectricity. *Journal of Magnetism and Magnetic Materials*, *306*(1), 1–8.

Kim, H. I., Lim, H., & Moon, A. (2018). Sex Differences in Cancer: Epidemiology, Genetics and Therapy. *Biomolecules & Therapeutics*, *26*(4), 335–342.

Kim, S., Chun, M., Wang, H., Cho, S., Oh, Y.-T., Kang, S.-H., & Yang, J. (2007). Bone Metastasis from Primary Hepatocellular Carcinoma: Characteristics of Soft Tissue Formation. *Cancer Research and Treatment: Official Journal of Korean Cancer Association*, *39*(3), 104.

Knudson, A. G. (1971). Mutation and Cancer: Statistical Study of Retinoblastoma. *Proceedings of the National Academy of Sciences of the United States of America*, *68*(4), 820.

Kolhatkar, R., Lote, A., & Khambhati, H. (2011). Active tumor targeting of nanomaterials using folic acid, transferrin, and integrin receptors. *Current Drug Discovery Technologies*, *8*(3), 197–206.

Krpetić, Ž., Singh, I., Su, W., Guerrini, L., Faulds, K., Burley, G. A., & Graham, D. (2012). Directed Assembly of DNA-Functionalized Gold Nanoparticles Using Pyrrole–Imidazole Polyamides. *Journal of the American Chemical Society*, *134*(20), 8356–8359.

Kubo, T., Shimose, S., Fujimori, J., Arihiro, K., & Ochi, M. (2013). Diversity of angiogenesis among malignant bone tumors. *Molecular and Clinical Oncology*, *1*(1), 131.

Landau, L. D., Bell, J. S., Kearsley, M. J., Pitaevskii, L. P., Lifshitz, E. M., & Sykes, J. B. (2013). *Electrodynamics of continuous media* (Vol. 8). Elsevier.

Lim, S. B., Banerjee, A., & Önyüksel, H. (2012). Improvement of drug safety by the use of lipid-based nanocarriers. *Journal of Controlled Release: Official Journal of the Controlled Release Society*, *163*(1), 34–45.

Loveday, C., Turnbull, C., Ramsay, E., Hughes, D., Ruark, E., Frankum, J. R., Bowden, G., Kalmyrzaev, B., Warren-Perry, M., Snape, K., Adlard, J. W., Barwell, J.,

Berg, J., Brady, A. F., Brewer, C., Brice, G., Chapman, C., Cook, J., Davidson, R., … Rahman, N. (2011). Germline mutations in RAD51D confer susceptibility to ovarian cancer. *Nature Genetics*, *43*(9), 879–882.

Lowry, G. v, Hill, R. J., Harper, S., Rawle, A. F., Hendren, C. O., Klaessig, F., Nobbmann, U., Sayre, P., & Rumble, J. (2016). Guidance to improve the scientific value of zeta-potential measurements in nanoEHS. *Environmental Science: Nano*, *3*(5), 953–965.

Macedo, F., Ladeira, K., Pinho, F., Saraiva, N., Bonito, N., Pinto, L., & Gonçalves, F. (2017). Bone Metastases: An Overview. *Oncology Reviews*, *11*(1).

Marew, T., & Birhanu, G. (2021). Three-dimensional printed nanostructure biomaterials for bone tissue engineering. *Regenerative Therapy*, *18*, 102–111.

Martincorena, I., & Campbell, P. J. (2015). Somatic mutation in cancer and normal cells. *Science (New York, N.Y.)*, *349*(6255), 1483–1489.

Matsumura, Y., & Maeda, H. (1986). A New Concept for Macromolecular Therapeutics in Cancer Chemotherapy: Mechanism of Tumoritropic Accumulation of Proteins and the Antitumor Agent Smancs1. *Cancer Research*, *46*(12_Part_1), 6387–6392.

Mehenni, H., Resta, N., Park, J. G., Miyaki, M., Guanti, G., & Costanza, M. C. (2006). Cancer risks in LKB1 germline mutation carriers. *Gut*, *55*(7), 984.

Minko, T., Rodriguez-Rodriguez, L., & Pozharov, V. (2013). Nanotechnology approaches for personalized treatment of multidrug resistant cancers. *Advanced Drug Delivery Reviews*, *65*(13–14), 1880–1895.

Mitter, D., Ullmann, R., Muradyan, A., Klein-Hitpaß, L., Kanber, D., Õunap, K., Kaulisch, M., & Lohmann, D. (2011). Genotype–phenotype correlations in patients with retinoblastoma and interstitial 13q deletions. *European Journal of Human Genetics*, *19*(9), 947.

Morachis, J. M., Mahmoud, E. A., & Almutairi, A. (2012). Physical and chemical strategies for therapeutic delivery by using polymeric nanoparticles. *Pharmacological Reviews*, *64*(3), 505–519.

Moskow, J. J., Bullrich, F., Huebner, K., Daar, I. O., & Buchberg, A. M. (1995). Meis1, a PBX1-related homeobox gene involved in myeloid leukemia in BXH-2 mice. *Molecular and Cellular Biology*, *15*(10), 5434–5443.

Mundy, G. R. (2002). Metastasis to bone: causes, consequences and therapeutic opportunities. *Nature Reviews. Cancer*, *2*(8), 584–593.

O'Grady, S. M., & So, Y. L. (2005). Molecular diversity and function of voltage-gated (Kv) potassium channels in epithelial cells. *The International Journal of Biochemistry & Cell Biology*, *37*(8), 1578–1594.

Ojima, I., Lichtenthal, B., Lee, S., Wang, C., & Wang, X. (2016). Taxane anticancer agents: a patent perspective. *Expert Opinion on Therapeutic Patents*, *26*(1), 1–20.

Ottaviani, G., & Jaffe, N. (2009). The epidemiology of osteosarcoma. *Cancer Treatment and Research*, *152*, 3–13.

Paget, S. (1889). The Distribution of Secondary Growths in Cancer of the Breast. *The Lancet*, *133*(3421), 571–573.

Pattni, B. S., & Torchilin, V. P. (2015). Targeted Drug Delivery Systems: Strategies and Challenges. In P. v Devarajan & S. Jain (Eds.), *Targeted Drug Delivery: Concepts and Design* (pp. 3–38). Springer International Publishing.

Persidis, A. (1999). Cancer multidrug resistance. *Nature Biotechnology 1999 17:1*, *17*(1), 94–95.

Pienta, K. J., & Esper, P. S. (1993). Risk factors for prostate cancer. *Annals of Internal Medicine*, *118*(10), 793–803.

Quayle, L., Ottewell, P., & Holen, I. (2015). Bone Metastasis: Molecular Mechanisms Implicated in Tumour Cell Dormancy in Breast and Prostate Cancer. *Current Cancer Drug Targets*, *15*(6), 469–480.

Rajabi, M., Srinivasan, M., & Mousa, S. A. (2016). Nanobiomaterials in drug delivery. *Nanobiomaterials in Drug Delivery: Applications of Nanobiomaterials*, 1–37.

Raymaekers, K., Stegen, S., Gastel, N. van, & Carmeliet, G. (2015). The vasculature: a vessel for bone metastasis. *BoneKEy Reports*, *4*.

Riggi, N., & Stamenkovic, I. (2007). The Biology of Ewing sarcoma. *Cancer Letters*, *254*(1), 1–10.

Rim, C. H., Choi, C., Choi, J., & Seong, J. (2017). Establishment of a Disease-Specific Graded Prognostic Assessment for Hepatocellular Carcinoma Patients with Spinal Metastasis. *Gut and Liver*, *11*(4), 535.

Rodzinski, A., Guduru, R., Liang, P., Hadjikhani, A., Stewart, T., Stimphil, E., Runowicz, C., Cote, R., Altman, N., Datar, R., & Khizroev, S. (2016). Targeted and controlled anticancer drug delivery and release with magnetoelectric nanoparticles. *Scientific Reports 2016 6:1*, *6*(1), 1–14.

Roodman, G. D. (2004). Mechanisms of Bone Metastasis. *New England Journal of Medicine*, *350*(16), 1655–1664.

Sağlık, Y. (2014). Kondrosarkomlar. *TOTBİD Dergisi*, *13*(3), 240–246.

Samuel, J., & Bhandari, R. (1988). General Setting for Berry's Phase. *Physical Review Letters*, *60*(23), 2339.

Schäf, O., Ghobarkar, H., & Knauth, P. (2004). Hydrothermal Synthesis of Nanomaterials. *Nanostructured Materials*, 23–41.

Schmaljohann, D. (2006). Thermo- and pH-responsive polymers in drug delivery. *Advanced Drug Delivery Reviews*, *58*(15), 1655–1670.

Schmid, H. (1994). Multi-ferroic magnetoelectrics. *Ferroelectrics*, *162*(1), 317–338.

Shahzad, K., Mushtaq, S., Rizwan, M., Khalid, W., Atif, M., Din, F. U., Ahmad, N., Abbasi, R., & Ali, Z. (2021). Field-controlled magnetoelectric core-shell CoFe2O4@BaTiO3 nanoparticles as effective drug carriers and drug release in vitro. *Materials Science and Engineering: C*, *119*, 111444.

Shen, J., Yin, Q., Chen, L., Zhang, Z., & Li, Y. (2012). Co-delivery of paclitaxel and survivin shRNA by pluronic P85-PEI/TPGS complex nanoparticles to overcome drug resistance in lung cancer. *Biomaterials*, *33*(33), 8613–8624.

Siegel, R. L., Miller, K. D., Fuchs, H. E., & Jemal, A. (2022). Cancer statistics, 2022. *CA: A Cancer Journal for Clinicians*, *72*(1), 7–33.

Simunovic, F., & Finkenzeller, G. (2021). Vascularization Strategies in Bone Tissue Engineering. *Cells*, *10*(7).

Stein, C. J., & Colditz, G. A. (2004). Modifiable risk factors for cancer. *British Journal of Cancer 2004 90:2*, *90*(2), 299–303.

Stenfelt, S., Blixt, M. K. E., All-Ericsson, C., Hallböök, F., & Boije, H. (2017). Heterogeneity in retinoblastoma: a tale of molecules and models. *Clinical and Translational Medicine*, *6*(1), 42.

Stewart, T. S., Nagesetti, A., Guduru, R., Liang, P., Stimphil, E., Hadjikhani, A., Salgueiro, L., Horstmyer, J., Cai, R., Schally, A., & Khizroev, S. (2018). Magnetoelectric nanoparticles for delivery of antitumor peptides into glioblastoma cells by magnetic fields. *Nanomedicine (London, England)*, *13*(4), 423–438.

Stimphil, E., Nagesetti, A., Guduru, R., Stewart, T., Rodzinski, A., Liang, P., & Khizroev, S. (2017). Physics considerations in targeted anticancer drug delivery by magnetoelectric nanoparticles. *Applied Physics Reviews*, *4*(2), 021101.

Strebhardt, K., & Ullrich, A. (2008). Paul Ehrlich's magic bullet concept: 100 years of progress. *Nature Reviews Cancer 2008 8:6*, *8*(6), 473–480.

Sui, Y., Xin, C., Zhang, X., Wang, Y., Wang, Y., Wang, X., Liu, Z., Li, B., & Liu, X. (2015). Enhancement of multiferroic in BiFeO3 by Co doping. *Journal of Alloys and Compounds*, *645*, 78–84.

Svingen, T., & Tonissen, K. F. (2003). Altered HOX gene expression in human skin and breast cancer cells. *Cancer Biology & Therapy*, *2*(5), 518–523.

Sybil Biermann, J., Adkins, D. R., Agulnik, M., Benjamin, R. S., Brigman, B., Butrynski, J. E., Cheong, D., Chow, W., Curry, W. T., Frassica, D. A., Frassica, F. J., Hande, K. R., Hornicek, F. J., Jones, R. L., Mayerson, J., McGarry, S. v., McGrath, B., Morris, C. D., O'donnell, R. J., … Sundar, H. (2013). Bone Cancer. *Journal of the National Comprehensive Cancer Network*, *11*(6), 688–723.

Tomoeda, M., Yuki, M., Kubo, C., Yoshizawa, H., Kitamura, M., Nagata, S., Nishizawa, Y., & Tomita, Y. (2011). Role of Meis1 in mitochondrial gene transcription of pancreatic cancer cells. *Biochemical and Biophysical Research Communications*, *410*(4), 798–802.

Torchilin, V. P. (2006). Nanoparticulates as drug carriers. *Nanoparticulates as Drug Carriers*, 1–725.

Tumanski, S. (2016). Handbook of magnetic measurements. *Handbook of Magnetic Measurements*, 1–382.

Turan, R. D., Albayrak, E., Uslu, M., Siyah, P., Alyazici, L. Y., Kalkan, B. M., Aslan, G. S., Yucel, D., Aksoz, M., Tuysuz, E. C., Meric, N., Durdagi, S., Gulbas, Z., & Kocabas, F. (2020). Development of Small Molecule MEIS Inhibitors that modulate HSC activity. *Scientific Reports 2020 10:1*, *10*(1), 1–17.

Turgutalp, B., Uslu, M., Helvacioglu, S., Charehsaz, M., Gurdal, E. E., Sippl, W., Kocabas, F., & Yarim, M. (2021). Lead Optimization and Structure-Activity Relationship Studies on Myeloid Ecotropic Viral Integration Site 1 Inhibitor. *Journal of Medicinal Chemistry*, *64*(19), 14448–14464.

Vasir, J. K., & Labhasetwar, V. (2005). Targeted drug delivery in cancer therapy. *Technology in Cancer Research & Treatment*, *4*(4), 363–374.

Vasir, J. K., Reddy, M. K., & Labhasetwar, V. D. (2006). Nanosystems in Drug Targeting: Opportunities and Challenges. *Current Nanoscience*, *1*(1), 47–64.

Wagner, V., Dullaart, A., Bock, A. K., & Zweck, A. (2006). The emerging nanomedicine landscape. *Nature Biotechnology 2006 24:10*, *24*(10), 1211–1217.

Wang, J. (2016). Multiferroic materials: Properties, techniques, and applications. *Multiferroic Materials: Properties, Techniques, and Applications*, 1–392.

Wang, P., Toledo, D., Zhang, E., Telusma, M., McDaniel, D., Liang, P., & Khizroev, S. (2020). Scanning probe microscopy study of cobalt ferrite-barium titanate coreshell magnetoelectric nanoparticles. *Journal of Magnetism and Magnetic Materials*, *516*, 167329.

Wang, Y., Zhang, W., & Yao, Q. (2021). Copper-based biomaterials for bone and cartilage tissue engineering. *Journal of Orthopaedic Translation*, *29*, 60–71.

Ward, M. A., & Georgiou, T. K. (2011). Thermoresponsive Polymers for Biomedical Applications. *Polymers 2011, Vol. 3, Pages 1215-1242*, *3*(3), 1215–1242.

Wardle, J., Robb, K., Vernon, S., & Waller, J. (2015). Screening for prevention and early diagnosis of cancer. *The American Psychologist*, *70*(2), 119–133.

White, M. C., Holman, D. M., Boehm, J. E., Peipins, L. A., Grossman, M., & Jane Henley, S. (2014). Age and cancer risk: a potentially modifiable relationship. *American Journal of Preventive Medicine*, *46*(3 Suppl 1).

Williams, D. B., & Carter, C. B. (2009). Transmission electron microscopy: A textbook for materials science. *Transmission Electron Microscopy: A Textbook for Materials Science*, 1–760.

Winau, F., Westphal, O., & Winau, R. (2004). Paul Ehrlich — in search of the magic bullet. *Microbes and Infection*, *6*(8), 786–789.

Wust, P., Hildebrandt, B., Sreenivasa, G., Rau, B., Gellermann, J., Riess, H., Felix, R., & Schlag, P. (2002). Hyperthermia in combined treatment of cancer. *Lancet Oncology*, *3*(8), 487–497.

Xiao, D., Chang, M. C., & Niu, Q. (2010). Berry phase effects on electronic properties. *Reviews of Modern Physics*, *82*(3), 1959–2007.

Yatvin, M. B., Weinstein, J. N., Dennis, W. H., & Blumenthal, R. (1978). Design of liposomes for enhanced local release of drugs by hyperthermia. *Science (New York, N.Y.)*, *202*(4374), 1290–1293.

Yue, K., Guduru, R., Hong, J., Liang, P., Nair, M., & Khizroev, S. (2012). Magneto-Electric Nano-Particles for Non-Invasive Brain Stimulation. *PloS One*, *7*(9), e44040.

Zvezdin, A. K., Vorob'ev, G. P., Kadomtseva, A. M., Popov, Y. F., Pyatakov, A. P., Bezmaternykh, L. N., Kuvardin, A. v, & Popova, E. A. (2006). Magnetoelectric and magnetoelastic interactions in NdFe3(BO3)4 multiferroics. *JETP Letters 2006 83:11*, *83*(11), 509–514.

http-1: https://www.cancer.org/cancer/bone-cancer/about/key-statistics.html (Accessed: 19.08.2022)

http-2: https://www.cancer.org/cancer/bone-cancer/treating/surgery.html (Accessed: 21.08.2022)

http-3: https://www.cancer.org/cancer/bone-cancer/causes-risks-prevention/risk-factors.html (Accessed: 21.08.2022)

http-4: https://www.urmc.rochester.edu/encyclopedia/content.aspx?contenttypeid=34&contentid=24885-1 (Accessed: 21.08.2022)

http-5: https://ec.europa.eu/health/scientific_committees/emerging/docs/scenihr_o_032.pdf (Accessed: 25.08.2022)

APPENDIX-1 Simulation Algorithm

%%Parameters

k = 8.987551*10^{9}; %Coulomb Constant (Nm^2C^{-2})

V = 1; %Zeta Potential

d = 10^{-9}; %Particle Size/2

Q = (V*d) /k; %Surface Charge, d: Particle Radius, V: Zeta Potential

E_{k0} = 1*10^{5}; % The threshold value of the electrical field for nanoelectroporation in cancer cells should be above 0.1 V/μm.

E_{s0} = 1.5*10^{6}; % Average 1.5 V/μm for healthy cells.

R_c = 0; %Cut-off Distance: The critical effective distance between the nanoparticle and the cancer cell membrane

F = (k*Q^2) /(4*R_c^2); % The force of attraction of cancer cells

%%Simulation of Generated Electric Field

%In this part of the code, a pool of electrical fields that can potentially be generated based on each zeta potential, particle radius, and critical distance is created.

l=1; V_d = zeros (30,1); d_d = zeros (1,125); R_{cd} = zeros (200,1);

for i = 1:30

V_d(i,1) = V*2; % Zeta potential is stored as a different data.

for j = 1:125

Q(i,j) = (V*d) /k; % Particle charge is calculated with each zeta potential and particle radius.

d_d(1,j) = d; % Particle radius is stored as a different data.

for z = 1:200

R_{cd}(z,1) = R_c*10^{-9}; % The critical distance is stored as a different data.

E(z,l) = 0.25*(k*Q(i,j))/R_c^2; % With each parameter, the electrical field that can affect the membrane is calculated.

R_c = R_c + 5*10^{-9}; % The critical distance change is handled in increments of 5 units.

end

R_c = 0;

l = l + 1;

```
                d = d + 2*10^-9; % Particle radius is handled in 2-unit increments.
            end
        d = 10^-9;
        V = V + 1; % The zeta potential is addressed in 1-unit changes.
end
%%Selection of suitable electrical fields for cancer cells
% In this section, data of 1.5 V/μm and above are reset to select the appropriate
electrical fields.
    [k,q] = size (E);
for a = 1:k
    for b = 1:q
      if E(a,b) >= Es0 % Electrical fields of 1.5 V/μm and above are equated to 1.5.
            E(a,b) = Es0;
      elseif E(a,b) == Inf || E(a,b) < Ek0 % Ineffective electric fields are reset..
            E(a,b) = 0;
      end
    end
end
%%Selection of appropriate zeta potential, particle radius and critical distance for
cancer cells
    rd = zeros (200*3750, 2); t = 1;
for a = 1:k
      for b = 1:q
            if E(a,b) > 0 && E(a,b) < Es0 % Only electrical fields that can interact
            with cancer cells are regulated.
                  rd(t,1) = a; % The critical distance is assigned to the rd(t,1)
                  matrix.
                  rd(t,2) = b; % The charge is assigned to the rd(t,2) matrix.
                  t = t + 1;
            end
      end
end
[m, ~] = size(rd); Qij = zeros (2, m); kQ = rd(:,2)*k;
```

for i = 1:m

$Q_{ij}(1, i) = \mathrm{mod}(k_Q(i,1),250) + 1$; % Appropriate zeta potentials are determined from the charges drawn by back-calculating from the appropriate electrical fields.

$Q_{ij}(2, i) = ((k_Q(i,1) - \mathrm{mod}(k_Q(i,1),250))/250) + 1$; % Appropriate particle radii are determined from the charges drawn by back-calculating from appropriate electrical fields.

end

% According to the determined zeta potentials, particle sizes and critical distances, the pool of each possibility is plotted.

$Q_{ijj} = Q_{ij}(1,:)$; $Q_{ji} = Q_{ij}(2,:)$; $R_{dd} = r_d(:,1)'$;

p = plot3 (Q_{ji},Q_{ijj},R_{dd});

p.LineStyle = "none"; p.Color = "blue"; p.Marker = ".";

xlabel('Zeta Potential (mV)')

ylabel('Particle Radius (nm)')

zlabel('Cut-off Distance (nm)')

CURRICULUM VITAE

ORCID ID: 0000-0002-2157-3209

Name Surname : Gençay SEVİM

Foreign Language : English

Place and Year of Birth :

Email :

Education Background:

- 2023, Eskişehir Technical University, Advanced Technologies, Nanotechnology
- 2016, Akdeniz University, Faculty of Medicine, Biophysics
- 2014, Middle East Technical University, Faculty of Arts & Science, Physics

Professional Background:

- 2020, Lecturer, Ufuk University, Vocational School of Health Services

Publications and/or Scientific/Artistic Activities:

Publications:

- Üncü, Y. A., Sevim, G., Özdoğan, H., & Ağar, O. (2022). Monte Carlo simulations of radiation effects on the cell membrane. Kuwait Journal of Science.
- Üncü, Y. A., Sevim, G., & Canpolat, M. (2022). Approaches to preclinical studies with heterogeneous breast phantom using reconstruction and three-dimensional image processing algorithms for diffuse optical imaging. International Journal of Imaging Systems and Technology, 32(1), 343-353.
- Sevim, G., Üncü, Y. A., Mercan, T., & Canpolat, M. (2021). Image reconstruction for diffuse optical tomography using bi-conjugate gradient and transpose-free quasi minimal residual algorithms and comparison of them. International Journal of Imaging Systems and Technology, 31(4), 1894-1905.
- Üncü, Y. A., Sevim, G., Mercan, T., Vural, V., Durmaz, E., & Canpolat, M. (2021). Differentiation of tumoral and non-tumoral breast lesions using back reflection diffuse optical tomography: A pilot clinical study. International Journal of Imaging Systems and Technology, 31(4), 2023-2031.
- Sevim, G., Üncü, Y. A., & Canpolat, M. Application of Reconstruction Algorithms by Simulation Experiments for the Diagnosis of Breast Tumor-Like Tissues Modeled in Diffuse Optical Tomography. Düzce Üniversitesi Bilim ve Teknoloji Dergisi, 9(6), 167-176.

- Üncü Y.A., Sevim G., Canpolat M., "Difüz Optik Tomografi Sisteminde Görüntü İşleme Uygulamalarının Test Edilmesi", Süleyman Demirel Üniversitesi Fen Edebiyat Fakültesi Fen Dergisi, cilt.16, no.1, ss.1-16, 2021
- Sevim G., Üncü Y.A., Canpolat M., "Difüz Optik Tomografi Sistemlerinde Kullanılan Geri Çatım Algoritmaları için İterasyon Sayısını Belirmede Alternatif Bir Yöntem", Süleyman Demirel Üniversitesi Fen-Edebiyat Fakültesi Fen Dergisi, cilt.16, no.1, ss.246-258, 2021.
- Mercan T., Sevim G., Üncü Y.A., Uslu S., Kazanci H.Ö., Canpolat M., "The Comparison of Reconstruction Algorithms for Diffuse Optical Tomography", Süleyman Demirel Üniversitesi Fen Edebiyat Fakültesi Fen Dergisi, ss.285-295, 2019.

Book Chapter:

- Büyükköroğlu, G., Şenel, B., & Sevim, G. (2022). Biotechnology in cosmetics. In Biotechnology in Healthcare (pp. 273-287). Academic Press.

International Conference Presentation and Poster:

- Sevim G., Büyükköroğlu G., "A Mobile Application to Theoretically Calculate the Physical Properties of Magneto-Electric Effect Nanostructures that can Target to Cancer Cells", ASES III. International Health, Engineering and Sciences Conference. (October 14-16, 2022).
- Sevim G., Büyükköroğlu G., "Ph Standardization for The Synthesis of Magnetic Nanostructures Used in Targeted Drug Delivery Systems" 5th International Congress of Multidisciplinary Studies in Medical Sciences (September 23-25, 2022).
- Sevim G., Üncü Y., Canpolat, M., "The Application of Reconstruction Algorithms with Simulation Experiments to Diagnosis Modeled Breast Tumor-like Tissues in Diffuse Optical Tomography." October 2021, International Conference on Artificial Intelligence and Applied Mathematics in Engineering (ICAIAME 2021).
- Sevim G., Mercan T., Uncu Y.A., Canpolat M., "A new reconstruction technique used in Diffuse Optical Tomography System", November 2017, Conference: 2017 21st National Biomedical Engineering Meeting (BIYOMUT).

- Üncü Y.A., Mercan T., Sevim G., Canpolat M., "Interpolation Applications in Diffuse Optical Tomography System", November 2017, Conference: 2017 21st National Biomedical Engineering Meeting (BIYOMUT)
- Mercan T., Sevim G., Kazancı H.Ö., Üncü Y.A., Canpolat M., "Comparison of Images Produced by Diffuse Optical Tomography with Two Different Backscatter Techniques", November 2017, Conference: 2017 21st National BIYOMUT.
- Üncü Y.A., Mercan T., Canpolat M., Sevim G., "A new approach to image processing in diffuse optical tomography and 3-D image", May 2017, Conference: 2017 25th Signal Processing and Communications Applications Conference (SIU).

Professional Union/Association/Organization Memberships:

- Turkish Biophysics Association (TBA)
- Molecular Cancer Research Association (MOKAD)
- European Association for Cancer Research (EACR)
- Evaluation and Accreditation of Health Services Education Programs Association (SAHIDAD)
- European Cooperation in Science & Technology (E-COST)

COST Action CA18103: (INNOGLY) INNOvation with Glycans new frontiers from synthesis to new biological targets.

- WG1: Glycan-based correlations in developmental and cancer biology.
- WG2: Glycan dependent modulation of autophagy, endocytosis, and lysosomal functions: cancer, lysosomal disorders, and neurodegenerative diseases.

COST Action CA18132: Functional Glyconanomaterials for the Development of Diagnostics and Targeted Therapeutic Probes

- WG1: Innovative glyconanomaterials for biomedical prognostic and diagnostic devices; Synthesis and application.
- WG2: Bioactive glycomaterials for personalized, regenerative, and non-invasive therapies.